

1-1-2013

Analytical Modeling, Perturbation Analysis and Experimental Characterization of Guided Surface Acoustic Wave Sensors

Onursal Onen

University of South Florida, onursalonen@mail.usf.edu

Follow this and additional works at: <http://scholarcommons.usf.edu/etd>

 Part of the [Mechanical Engineering Commons](#)

Scholar Commons Citation

Onen, Onursal, "Analytical Modeling, Perturbation Analysis and Experimental Characterization of Guided Surface Acoustic Wave Sensors" (2013). *Graduate Theses and Dissertations*.
<http://scholarcommons.usf.edu/etd/4555>

This Dissertation is brought to you for free and open access by the Graduate School at Scholar Commons. It has been accepted for inclusion in Graduate Theses and Dissertations by an authorized administrator of Scholar Commons. For more information, please contact scholarcommons@usf.edu.

Analytical Modeling, Perturbation Analysis and Experimental Characterization of
Guided Surface Acoustic Wave Sensors

by

Onursal Onen

A dissertation submitted in partial fulfillment
of the requirements for the degree of
Doctor of Philosophy
Department of Mechanical Engineering
College of Engineering
University of South Florida

Major Professor: Rasim Guldiken, Ph.D.
Nathan Crane, Ph.D.
Nathan Gallant, Ph.D.
Patricia Kruk, Ph.D.
Ashok Kumar, Ph.D.
Jing Wang, Ph.D.

Date of Approval:
March 26, 2013

Keywords: SAW, Love wave, immunosensor, oscillatory circuit, surface
functionalization, biomarker, perturbation, Bcl-2

Copyright © 2013, Onursal Onen

DEDICATION

To my family.

ACKNOWLEDGMENTS

Firstly, I have to say I am very happy to have the chance to acknowledge all the great people I am surrounded with that made this dissertation and Ph.D. possible. I tried to include and show my gratitude and thankfulness for all the people in this section, and my apologies for those, whom I forgot to mention.

A dissertation acknowledgement section typically starts with acknowledging the major professor. The reason I want to start with Dr. Rasim Guldiken is definitely not because of this common practice. Sincerely, it is only because he is the person who should be acknowledged first. He is the person who made me come here, and I am very happy to say I am glad I did. Starting from the very first couple e-mails; to kindly hosting me at my very first night in Tampa; and to every single talk, discussion we have; every project, paper or study we worked on; it was a pleasure to work with him and having him as my major professor. Personally, he has always been a very good friend, listener and a supporter, always nice, caring, thoughtful and kind. Academically, he has always been an inspiring, supporting and positively challenging mentor. It is pretty amazing to work together for this long and not to have any issues or problems. I am feeling and will always feel extremely lucky to have him as my supervisor and more as a friend during these years of study.

I would like to acknowledge the members in my committee next: Dr. Nathan Crane, Dr. Nathan Gallant, Dr. Patricia Kruk, Dr. Ashok Kumar, and Dr. Jing Wang. I

not only have the chance of having them in my committee; but also had the chance to work with almost all of them in several projects and publications as well. Again to my luck, they were always helpful, thoughtful, nice, and inspiring. Anytime I was stuck in something, they welcomed me to discuss ideas and to answer my, sometimes irrelevant, questions with patience and care. I have learned a lot from them all. They made everything much easier. I would like to thank them one more time for with all their help, support, and further having me involved in their projects.

The biggest personal support was from my family: my father Yuksel Onen, my mother Ayhan Onen, my grandmother Nermin Senerler, and my brother Alper Onen. I would like to thank them one more time here for all they have done for me to become the person I am right now. And further, for their love, understating, encouragement and support during this study. They were all missed a lot during the time I have been in here, and I am pretty sure they missed me more than I missed them. I want to additionally thank them bearing with me and this feeling, and hardly every complaining about it. As I dedicated this work to them, they deserve more acknowledgement than I can give.

Next comes, all the special people, who provided exceptional friendship and support. I would like to start with my roommate Mark Grichanik and his little puppy Couscous for everything. The life and the experience I had during these years would not be the same without their existence. I would like to thank Mr. Grichanik for his dear friendship, all the great things he had introduced to me and being nice, and kind. In a way that, not even raising our voices once to each other during the years we lived at the same house. And I want to thank Couscous for all her love she has, being a nice puppy and all the fun and entertainment she had provided.

I would like to continue with my thanks to my online support group, who were once in Turkey, now spread all over the world. I would like to thank you all, for being there whenever I needed, for long periods of time; listening me and sharing everything. There are so many of you, but I would like to list the names who were literally always there, not in particular order: Onur Isikli, Erman Ozgur, Isil Ozfidan, Nese Karahasan, Bengi Bezirgan, Tugba Aktan, Koray Tascilar, Semih Ertugrul, Utku Gurtunca, Cankat Hapa, Ali Sinan Basar, Murat Sasmaz, Erdinc Kaya, and Baturalp Ozcan. These people are most possibly have the biggest share to listen all my whining and cool stories; but never complained a bit. Thanks for bearing with me, being not only online but being there, and making me feel like I never left home, on facebook, gtalk, anytime we meet at Turkey or anywhere.

Following online support, I would like to thank my Turkish fellows here in Tampa, for representing what I have been missing home. I would like to acknowledge Emre Demirocak, Aret Karademir, Umut Morkoc, Tugba Pala and Cigdem Akan for dear friendship and support which we all share and need in this once foreign land. Another big acknowledgement should go to my honorary department at USF, Department of Psychology. Meeting you all through my roommate, I would like to thank you all for all your friendship, all the fun and not-so-fun times we have shared. I, again, would like to name some people: Adam Ducey, Jessica Conteras, Glen Forester, Ryan Johnson, Matthew Grossman, Jason Chen. I am very happy to meet you all, and hope to keep in touch for the rest of my life. I would like to continue with my fellow engineering graduate students and scholars. I would like to thank my current and former lab mates Myeong Chan Jo, Tao Wang, Joel Cooper, Jairo Martinez, Klaus Windhager, Dr. Alper

Sisman, Greeshma Manohar, Gokhan Karaman, Rafael Rodriguez; my office mates Vinny Carias, Olukemi Akintewe, Gulnur Efe Sanden, Maritza Muniz and fellow graduate students Jamie Trahan, Asad Ahmad, Jose Carballo, Qi Ni and Mehdi Khodyari for their friendship, and conversations/discussions on all academic and daily issues.

Additionally I would like to thank all the staff of NREC, especially Robert Tufts and Richard Everly, for all their help and trainings they provided; and helping me with any problems I have faced.

I would like to wrap up this long acknowledgement part with sincerely thanking every single person one more time, whether I was able to mention or I not. Not only you all helped for (or even made) this study and experience to be possible, you made me enjoy almost every single moment. Thank you all.

TABLE OF CONTENTS

LIST OF TABLES.....	iii
LIST OF FIGURES	iv
ABSTRACT.....	vii
CHAPTER 1. INTRODUCTION.....	1
CHAPTER 2. SURFACE ACOUSTIC WAVE BIOSENSORS.....	7
2.1. Interdigital Transducers	9
2.2. Surface Acoustic Waves	11
2.2.1. Piezoelectricity.....	11
2.2.2. Materials and Crystal Cuts.....	14
2.2.3. Rayleigh Surface Acoustic Waves.....	15
2.2.4. Shear Horizontal SAWs.....	16
2.2.4.1. Shear Transverse Waves.....	18
2.2.4.2. Love Waves	18
2.3. SAW Biosensors.....	19
2.3.1. Measurement Methods and Sensor Configurations	20
2.3.2. Overview of Existing Literature	29
CHAPTER 3. ANALYTICAL MODELING	32
3.1. Analytical Modeling of Wave Propagation	34
3.1.1. Three Layer Model	34
3.1.2. Generalized Model of a N Layer System.....	39
3.2. Maxwell's Viscoelasticity Model	44
3.3. Numerical Solution of Dispersion Relations	48
3.3.1. Three Layer System	48
3.3.2. Fluid Loaded (Four Layer) System.....	50
3.4. Parametric Study.....	52
3.4.1. Dispersion Solutions of Substrate and Guiding Layer.....	52
3.5. Model Verification.....	61
CHAPTER 4. PERTURBATION ANALYSIS	66
4.1. Perturbation Theory	66
4.2. Perturbation by Guiding Layer	70
4.3. Perturbation by Mass Layer.....	72
4.4. Perturbation by Fluid Loaded Mass Layer.....	86

CHAPTER 5. CASE STUDY: BCL-2 SAW IMMUNOSENSOR	89
Note to Reader	89
5.1. Introduction.....	89
5.2. Sensor Design and Fabrication	94
5.2.1. Sensor Design	94
5.2.2. Fabrication	96
5.2.3. Surface Functionalization	98
5.3. Measurement Setup and Results	101
5.3.1. Oscillatory Circuit Design and Experimental Setup.....	101
5.3.2. Results.....	106
5.4. Perturbation Considerations.....	109
5.5. Discussion and Conclusions	113
CHAPTER 6. CONCLUSION.....	116
6.1. Summary and Contributions	116
6.2. Future Work.....	119
REFERENCES	120
APPENDICES	130
Appendix A. Matlab Codes.....	131
Appendix B. Frequency Responses of the Bare Sensors	136
Appendix C. Copyright Clearance.....	138

LIST OF TABLES

Table 1. A summary of immunosensor applications reported in literature.....	26
Table 2. Material properties for parametric study.	53
Table 3. Effective shear velocity and density values used for data fit.....	62
Table 4. Elevated urinary Bcl-2 in cohorts for healthy controls, benign diseases, and early- and late-stage ovarian cancer.	92
Table 5. Sensor design parameters.....	96
Table 6. Steady state frequency shifts of an acoustic biosensor for Bcl-2.	110

LIST OF FIGURES

Figure 1. Two main types of SAWs.....	9
Figure 2. Methods for SAW energy confinement on surface.....	9
Figure 3. Interdigital transducer illustration.....	11
Figure 4. SAW synchronous frequency and bandwidth.....	13
Figure 5. SAW sensor measurement methods.....	21
Figure 6. SAW sensor configurations.....	24
Figure 7. Overview of a three layer system.....	34
Figure 8. Generalized system with $N=i+1$ layers.....	42
Figure 9. Dispersion curve with substrate: ST-Quartz, guiding layer: Parylene-C, frequency:100 MHz, $\omega\tau = 10^6$,x-axis: z.....	54
Figure 10. Dispersion curve with substrate: ST-Quartz, guiding layer: Parylene-C, frequency:10, 100 and 1000 MHz, $\omega\tau = 10^6$,x-axis: guiding layer thickness.....	55
Figure 11. Dispersion curve with substrate: ST-Quartz, guiding layer: Parylene-C, frequency: 100 MHz, $\omega\tau = 10$ and 10^6 ,x-axis: dimensionless guiding layer thickness.....	56
Figure 12. Dispersion curve for substrate: ST-Quartz, 41°LiNbO_3 and 36°LiTaO_3 , guiding layer: Parylene-C, frequency: 100 MHz, $\omega\tau=10^6$,x-axis: dimensionless guiding layer thickness.....	57
Figure 13. Dispersion curve for substrate: ST-Quartz, guiding layer: SiO_2 , chromium, gold, SU-8 and Parylene-C, frequency: 100 MHz, $\omega\tau=10^6$, x-axis: guiding layer thickness.....	59
Figure 14. Dispersion curve for substrate: 36°LiTaO_3 , guiding layer: SiO_2 , chromium, gold, SU-8 and Parylene-C, frequency: 100 MHz, $\omega\tau=10^6$,x-axis: guiding layer thickness.....	60

Figure 15. Data points and curve fit for substrate: quartz, $\lambda:80 \mu\text{m}$, guiding layer: S1813 ($V_{g,eff}=3200 \text{ m/s}$, $\rho_{g,eff}=1200 \text{ kg/m}^3$)	63
Figure 16. Data points and curve fit for substrate: LiNbO ₃ , $\lambda:80 \mu\text{m}$, guiding layer: S1813 ($V_{g,eff}=3200 \text{ m/s}$, $\rho_{g,eff}=2200 \text{ kg/m}^3$)	63
Figure 17. Data points and curve fit for substrate: quartz, $\lambda: 300 \mu\text{m}$, guiding layer: AZP4620 ($V_{g,eff}=1600 \text{ m/s}$, $\rho_{g,eff}=3200 \text{ kg/m}^3$)	64
Figure 18. Data points and curve fit for substrate: LiNbO ₃ , $\lambda: 300 \mu\text{m}$, guiding layer: AZP4620 ($V_{g,eff}=1600 \text{ m/s}$, $\rho_{g,eff}=5000 \text{ kg/m}^3$)	64
Figure 19. Single layer perturbation model	68
Figure 20. Sensitivity with substrate: quartz; guiding layer: chrome; $f=100 \text{ MHz}$; $\omega\tau=10^6$ with perturbing mass layers: Parylene-C, gold, SiO ₂ and chromium.	77
Figure 21. Sensitivity with substrate: LiTaO ₃ ; guiding layer: chrome; $f=100 \text{ MHz}$; $\omega\tau =10^6$ with perturbing mass layers: Parylene-C, gold, SiO ₂ , and chromium.	78
Figure 22. Sensitivity with substrate: quartz; guiding layer: gold; $f=100 \text{ MHz}$; $\omega\tau =10^6$ with perturbing mass layers: Parylene-C, gold, SiO ₂ and chromium.	79
Figure 23. Sensitivity with substrate: LiTaO ₃ ; guiding layer: gold; $f=100 \text{ MHz}$; $\omega\tau =10^6$ with perturbing mass layers: Parylene-C, gold, SiO ₂ and chromium.	80
Figure 24. Sensitivity with substrate: quartz; guiding layer: Parylene-C; $f=100 \text{ MHz}$; $\omega\tau =10^6$ with perturbing mass layers: Parylene-C, gold, SiO ₂ and chromium.	81
Figure 25. Sensitivity with substrate: LiTaO ₃ guiding layer: Parylene-C; $f=100 \text{ MHz}$; $\omega\tau =10^6$ with perturbing mass layers: Parylene-C, gold, SiO ₂ and chromium.	82
Figure 26. Sensitivity with substrate: quartz guiding layer: Parylene-C; $f=100 \text{ MHz}$; $\omega\tau =10$ and 10^6 with perturbing mass layers: Parylene-C, and protein layer.	84
Figure 27. Disperison curves with modified density and shear velocity, after experimental verification.	85

Figure 28. Sensitivity curves with modified density and shear velocity, after experimental verification.	86
Figure 29. Illustration of sensor.	94
Figure 30. Overview of sensor fabrication.	97
Figure 31. Fabricated ST-cut Quartz sensor	98
Figure 32. Illustration of surface functionalization.....	100
Figure 33. Block schematic for oscillator circuit.....	102
Figure 34. Frequency response of sensor.....	104
Figure 35. Loop gain and loop phase measurements for filter design.....	105
Figure 36. Loop gain and loop phase measurements with filter.....	106
Figure 37. Measured frequency shift (Hz) for various concentrations of Bcl-2 in DPBS.....	107
Figure 38. Average frequency shift measured, corresponding to different Bcl-2 concentrations and best line fit.....	108
Figure 39. The frequency shifts corresponding to various concentrations of Bcl-2 in PBS, PBS only or BSA controls, and a mixture of Bcl-2 and BSA were measured with a acoustic biosensor.....	110
Figure B1. Insertion loss of ST-cut quartz sensor without surface functionalization.	136
Figure B2. Phase of ST-cut quartz sensor without surface functionalization.....	136
Figure B3. Insertion loss of lithium niobate sensor without surface functionalization.	137
Figure B4. Phase of lithium niobate sensor without surface functionalization.	137

ABSTRACT

In this dissertation, guided surface acoustic wave sensors were investigated theoretically and experimentally in detail for immunosensing applications. Shear horizontal polarized guided surface acoustic wave propagation for mass loading sensing applications was modeled using analytical modeling and characterized by perturbation analysis. The model verification was performed experimentally and a surface acoustic wave immunosensor case study was presented. The results of the immunosensing were also investigated using the perturbation analysis.

Guided surface acoustic wave propagation problem was investigated in detail for gravimetric (or mass loading) guided wave sensors, more specifically for immunosensors. The analytical model was developed for multilayer systems taking viscoelasticity into account. The closed form algebraic solutions were obtained by applying appropriate boundary conditions. A numerical approach was used to solve dispersion equation. Detailed parametric investigation of dispersion curves was conducted using typical substrate materials and guiding layers. Substrate types of ST-cut quartz, 41° YX lithium Niobate and 36° YX lithium tantalate with guiding layers of silicon dioxide, metals (chromium and gold), and polymers (Parylene-C and SU-8) were investigated. The effects of frequency and degree of viscoelasticity were also studied. The results showed that frequency only has effect on thickness with same shaped dispersion curves. Dispersion curves were found to be unaffected by the degree of viscoelasticity. It was

also observed that when there was a large shear velocity difference between substrate and guiding layer, a transition region with a gradual decrease in phase velocity was obtained. However, when shear velocities were close, a smooth transition was observed. Furthermore, it was observed that, large density differences between substrate and guiding layer resulted in sharp and with nearly constant slope transition. Smooth transition was observed for the cases of minimal density differences. Experimental verification of the model was done using multi-layer photoresists. It was shown that with modifications, the model was able to represent the cases studied.

Perturbation equations were developed with first order approximations by relating the slope of the dispersion curves with sensitivity. The equations were used to investigate the sensitivity for material selection (substrate, guiding layer, and mass perturbing layer) and degree of viscoelasticity. The investigations showed that the sensitivity was increased by using guiding layers with lower shear velocities and densities. Among the guiding layers investigated, Parylene C showed the highest sensitivity followed by gold and chrome. The perturbation investigations were also extended to viscoelasticity and to protein layers for immunosensing applications. It was observed that, viscous behavior resulted in slightly higher sensitivity; and sensitivity to protein layers was very close to sensitivity for polymers. The optimum case is found to be ST-cut quartz with Parylene-C guiding layer for protein layer sensing.

Finally, an immunosensing case study was presented for selective capture of protein B-cell lymphoma 2 (Bcl-2), which is elevated in many cancer types including ovarian cancer. The immunosensor was designed, fabricated, and experimentally characterized. An application-specific surface functionalization scheme with monoclonal

antibodies, ODMS, Protein A/G and Pluronic F127 was developed and applied. Characterization was done using the oscillation frequency shift of with sensor used as the feedback element of an oscillator circuit. Detection of Bcl-2 with target sensitivity of 0.5 ng/ml from buffer solutions was presented. A linear relation between frequency shift and Bcl-2 concentration was observed. The selectivity was shown with experiments by introducing another protein, in addition to Bcl-2, to the buffer. It was seen that similar detection performance of Bcl-2 was obtained even with presence of control protein in very high concentrations. The results were also analyzed with perturbation equations.

CHAPTER 1. INTRODUCTION

Acoustics is a highly interdisciplinary field with a wide variety of applications. Many different types of mechanical waves such as sound, stress, and pressure waves with wide range of frequency components are investigated under acoustics for potential applications ranging from structural vibrations to ultrasound. In the last few decades, several new applications of acoustic waves in the ultrasound range have emerged and are extensively investigated in fields such as medical imaging, nondestructive testing (NDT) and consumer electronics. The advancements in microfabrication techniques have led to reliable and low cost mass manufacturing of acoustic devices that enable deployment in several configurations. Acoustic devices operating in the ultrasound range are typically used as filters, resonators, sensors, and actuators in the aforementioned applications. One of the largest markets for acoustics at ultrasound frequencies is anticipated to be the telecommunications industry [1]. Especially surface acoustic wave (SAW) devices employed as filters or resonators are used in nearly all wireless devices such as tablets, cell phones; and also in base stations and RF front ends [1]. The advantages offered by SAW devices include their compact size and integrated circuit (IC) compatibility leading to their extensive use in communications. Ultrasound waves have also been used in medical imaging for decades, which provides non-invasive monitoring and diagnosis during pregnancy or for vascular imaging and monitoring. They are also employed in nondestructive evaluation (NDE) and testing (NDT) applications to monitor the health of

structures and to detect flaws and imperfections in components, welds, and materials. More recently, surface acoustic waves have also been employed in sensing applications, because of their high sensitivity to mechanical and electrical perturbations on the surface [2]. Acoustic sensors are used to measure physical, chemical and biological quantities using different modes of acoustic modes in a wide range of designs and sensor types [2].

Piezoelectricity has been the main transduction method for almost all ultrasound applications. Piezoelectricity is the reciprocal coupling between mechanical and electrical domains, which exists in some certain types of anisotropic materials [3]. In piezoelectric materials, electrical charges (potential difference) impose mechanical stress (strain) and reciprocally, stress induces charge. This reciprocity enables generation and sensing of acoustical waves using similar methods and devices. Piezoelectric transduction can be employed in several applications with suitable design and material selection.

The most typical sensor types and related acoustic modes used are: surface acoustic wave (SAW) sensors which uses surface acoustic waves, thickness shear-mode (TSM) sensor which uses resonant thickness shear modes, shear horizontal acoustic plate mode (SH-APM) sensors which uses bulk shear horizontal waves, and flexural plate-wave (FPW) sensors which employs Lamb waves [2]. Among these, the main focus of this study is the guided surface acoustic waves. Surface acoustic waves show good sensitivity to surface perturbations, with their energy concentrated at or very close to the surface [2]. Surface acoustic wave transduction is mainly performed by interdigital transducers (IDTs) patterned on piezoelectric substrates. An IDT is formed by two comb-shaped electrodes with periodical fingers [2]. By applying a voltage difference to comb pair, mechanical strain is generated on the substrate regions in contact with the electrodes

as a result of the piezoelectricity effect. As a result, a surface acoustic wave is formed on the surface due to the periodic structure of the IDTs. Several sensor applications have employed surface acoustic waves with capability to operate as vapor, humidity, temperature, mass sensors as well as biosensors [4].

Biosensing applications aim to detect biological target analytes ranging from biomarkers to fungi, bacteria, and viruses and to DNA. A biosensor is a device which can detect a target biological analyte. Acoustic biosensors offer the capability of low-cost, portable, rapid, sensitive, selective, and point-of care detection as a viable alternative to other methods [5].

SAW biosensors typically utilize shear horizontal polarized waves enabling sensing under liquid loading, which is essential for biosensing. SH SAWs propagate on the surface of materials with particle displacement and propagation in the plane of the surface [6]. Ideally, in SH SAWs, there is no normal to the surface motion on propagation plane. Normal-to-surface particle motions results in coupling of SAW waves to compressional waves under liquid loading, which renders sensor insensitive to target analyte [6]. Nevertheless, SH waves couple to shear vertical and longitudinal waves, because of the anisotropic nature of the substrate materials. This phenomenon leads to poor sensitivity with energy leaking to other modes. There are several methods to reduce energy leakage and to increase the sensitivity of the SH SAW sensors by confining energy to the surface. Two main approaches are use of surface transverse waves (STWs, which use metal gratings) and Love waves [6]. Love waves are obtained with guiding layer on SH SAW propagating surfaces. The thin guiding layers acting as a shielding/protection layer ensures energy confinement. Love wave devices have gathered

a lot of interest in the last few decades, after they were presented by Du and Harding [7]. Nonetheless, there is still lack of understanding on optimization and operation of the devices, to author's knowledge.

Biosensors are used in a broad range of applications: clinical diagnosis, biomedicine, food production and analysis, microbiology, pharmaceutical and drug analysis, pollution control and monitoring, for military and security applications [1]. Biosensors that utilize antibody–antigen interactions are called immunosensors. They are based on the same principles as conventional immunoassays, such as enzyme linked immunosorbent assay (ELISA). Acoustic immunosensors utilize antibody-antigen interactions for biosensing. They are typically utilized as delay line devices or resonators, along with several different types of electrical peripheries. Insertion loss, phase shift, oscillation frequency, quality factor and impedance data can be used to quantify sensing in acoustic immunosensors [2]. In addition to guiding layers used on SH SAW propagating surface for enhanced sensitivity (Love waves), SAW immunosensors usually employ additional layers or films. The layers are required to activate the surface for interaction with organic domain, to properly orient and immobilize antibodies, and to prevent non-specific binding [8]. These requirements further complicate the design, material selection, and operation, while ensuring sufficient sensitivity. The sensor operation also necessitates selection, implementation and optimization of electrical periphery in accordance with immunosensing.

SAW immunosensors requires incorporation of knowledge on several different fields, as described before. Understanding on the physics of acoustic wave propagation in anisotropic media is essential for the mechanism. Material selection for substrate,

fabrication, guiding layers, electrical interconnects are important to ensure high yield and reliable device throughput and operation. Proper activation of surface, and selection and application of bio-layers for selective and sensitive immunosensing requires extensive investigations on chemistry and biology. The sensor operation also necessitates selection, implementation and optimization of electrical periphery in accordance with immunosensing and all the materials involved. Considering all these aspects, optimization in the system level along with in each specific task is essential and usually involves several trade-offs and decision making. In this dissertation, the efforts on all these aspects of biosensors have been presented for a better understanding of SAW immunosensor design and operation.

The contents of this dissertation consist of both theoretical and experimental work of guided shear horizontal acoustic wave biosensors. In Chapter 2, a detailed description for surface acoustic waves is presented, following this introduction chapter. Surface acoustic waves and their types, piezoelectricity, interdigital transducers, an extensive literature survey on SAW immunosensors, and overview of the literature is presented.

The physics of the guided wave propagation problem is then investigated in Chapter 3. The problem is formed, starting from equation of wave motion in the substrate and in the guiding layers considering viscoelasticity. The system is formed, and solved by trial solutions, a frequently employed method in acoustics. Several systems in growing complexity are investigated and formulized step by step with inclusion of additional layers, which is typical in SAW immunosensors. In addition to presented closed-form solutions of three and four layer models, a generic method is also presented to form and solve the problem with infinite number of layers. A method for numerical solution of the

wave propagation problem is shown. A parametric study is also done and presented, in order to investigate the effect of different substrate materials and guiding layers. Experiments for dispersion were also done to illustrate the validity of the theory presented in this chapter.

Following Chapter 3, perturbation theory, which is used to obtain approximate solutions to complex problems, is introduced in Chapter 4. First order perturbation equations for the wave propagation problem are derived for investigating guided wave sensor performance and sensitivity. The parametric study given in Chapter 4 is extended to perturbation analysis to investigate sensitivity considerations in detail. Sensitivity of acoustic waves to several substrate types, guiding layers and mass perturbing layers is illustrated by sensitivity figures.

Chapter 5 contains a case study of SAW immunosensing, which was aimed for detection of anti-apoptotic protein Bcl-2. The manuscript and figures chapter is author's published work [5, 8], which includes detailed information on ovarian cancer; design, fabrication and operation of the sensing system; surface functionalization and experimental results. The results obtained, are also investigated using perturbation equations in this chapter.

Finally, general conclusions about SAW immunosensors and suggested work for the future are presented in Chapter 6. Unless otherwise stated, the design, fabrication, packaging of all the SAW devices used were done, all the codes in the appendix were written and all resulting dispersion and sensitivity graphs were obtained; all experiments were performed and all measurements were taken by the author.

CHAPTER 2. SURFACE ACOUSTIC WAVE BIOSENSORS

Surface acoustic waves are guided-waves that travel on the surface of a material with their energy concentrated at the surface [2]. There are several ways to excite and utilize surface acoustic waves. Piezoelectricity is the most typically employed mechanism for exciting SAWs. Piezoelectric behavior is defined as the coupling of mechanical domain (strain) and electrical domain (polarization) in certain type of anisotropic materials [9]. The piezoelectric behavior is both direct (strain causes charge or polarization) and indirect (polarization causes strain). Piezoelectricity can be used in several ways for SAWs: by metal inter digital transducers (IDTs) on piezoelectric substrates, piezoelectric IDTs or by bulk transducer-wedge pairs (by conversion of bulk waves to SAWs via Snell's law). Several types of SAWs exist depending on the material, cut type and boundary condition [1]. Polarization (longitudinal or shear) is one of the major properties of SAWs and other acoustic waves. In longitudinal waves (compressional wave, p-wave), the particle motion (or polarization) and the direction of wave propagation are parallel. A shear wave (transverse wave, s-wave) has particle motion perpendicular to the wave propagating direction. Shear waves can be shear horizontal (SH, in-plane polarization parallel to the substrate surface) or shear vertical (SV, transverse polarization normal to the surface). Shear and longitudinal modes can be highly coupled due to the anisotropic nature of the propagation medium. Such modes are called quasi-shear or quasi-longitudinal depending on the dominant mode. The quasi-

modes are excited when there is low crystal symmetry in the propagating direction [2]. SAWs with less coupling to other modes can be either pure with almost negligible coupling or pseudo-SAW (or leaky SAW), in which energy is not totally confined on the mode of interest, but leaks in other directions and modes.

Shear horizontal (SH) polarized SAWs are the most frequently used SAW types for biosensor, especially for liquid-loaded biosensing applications. In SH-SAWs, the particle displacement is in the plane of the surface (unlike normal-to-surface displacement of Rayleigh waves). SH-SAWs are minimally attenuated or damped by liquid loading. On the other hand, in Rayleigh waves, the particle displacement is directly coupled with the liquid on top as compressional waves and highly attenuated by mass loading and viscosity of the liquid itself. An illustration of the particle displacements of SH and Rayleigh SAWs is given in Figure 1. Rayleigh waves are virtually insensitive to mass loading changes in liquid sensing applications compared with SH SAWs, because of the coupling [6]. However, almost all SH wave propagation on various substrates involves leaky waves, with energy coupling to longitudinal and shear vertical wave components when excited. For this reason, the propagation nature of SH waves have been investigated for least possible coupling with other modes and special cuts of wafer types are selected and used for applications. There are several factors that determine these optimal cuts such as, high electromechanical coupling (energy conversion efficiency), temperature stability, and attenuation [10].

In addition to advantages of SH SAW devices, their performance can be enhanced by using methods to further concentrate wave energy on the surface. This can be achieved either by using guiding layers, named as Love wave devices (Figure 2-a); or by

periodic gratings placed normal to propagation direction, named as surface transverse wave devices (STWs, Figure 2-b). Both methods help enhancement of sensor performance by further confining the energy on the propagation surface, increasing sensitivity.

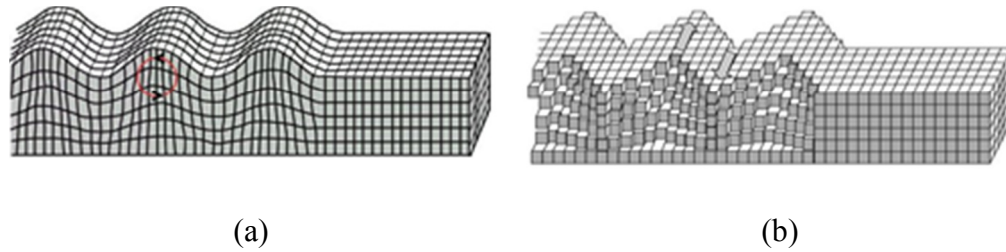


Figure 1. Two main types of SAWs. a) Rayleigh SAW, b) SH SAW.

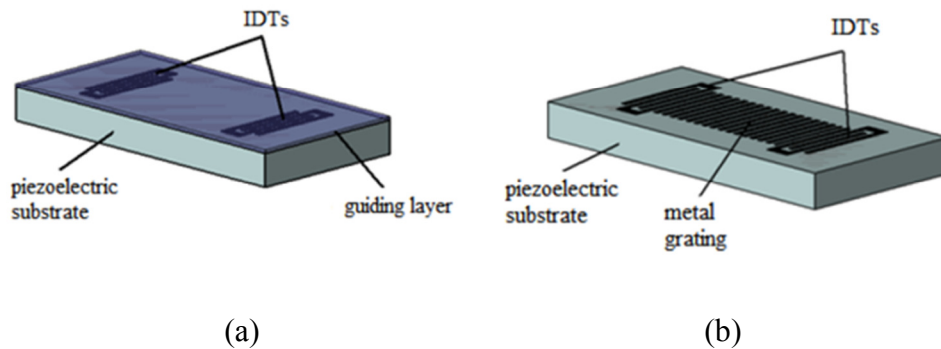


Figure 2. Methods for SAW energy confinement on surface. a) Love wave SAW device, b) surface transverse wave (STW) SAW device [6].

2.1. Interdigital Transducers

Interdigital transducers (IDTs) were reported first in 1965 by White and Voltmer as a way to utilize SAWs on a piezoelectric substrates [11]. Since then, IDTs were used as the most typical way for SAW transduction. An IDT is formed by two comb-like metal electrodes whose fingers are located in a periodic pattern, formed on top of a

piezoelectric substrate as seen in Figure 3-a. One of the combs is grounded and the other one is connected to a radio frequency (RF) supply. When an alternating RF potential difference is applied to the pair, the resulting electric field generates strain on the substrate as a result of the piezoelectricity effect. The periodic structure of the IDTs gives rise to a surface acoustic wave because of the periodic strain field. The propagation properties of the surface acoustic wave depend on substrate material, cut, and direction. The configuration illustrated in Figure 3-b is the most basic type of IDTs, named as bidirectional IDT [10].

The propagating surface acoustic waves also generate an electric field or charge, when encountering an IDT, similarly with the inverse piezoelectric effect.

IDTs can be designed to utilize SAWs with several different properties resulting in different operation characteristics and frequency responses. The two most important design parameters are center (or synchronous) frequency and bandwidth, illustrated in Figure 4. The synchronous (or operation) frequency of a SAW device constructed by IDTs depends on the periodicity of the IDT comb (corresponding to the wavelength λ of the SAW) and the SAW velocity (V_o). The synchronous frequency (f_o), then can be calculated using the formula $f_o = V_o / \lambda$. The bandwidth is defined as the range of the frequencies within 3dB of the amplitude of synchronous frequency. The bandwidth of an IDT depends on material selection, the number, and the shape of the fingers. Narrower bandwidths can be obtained by increasing the number of finger pairs [2] and wider band response can be obtained with decreasing number. Optimization studies should be conducted based on the desired operation characteristics. High number of finger pairs theoretically narrows the bandwidth, but up to a limit. It has been observed

that when finger number exceeds 100 [6], the losses associated with mass loading and the scattering from the electrodes increase, decreasing the sensor performance. Similarly, lower number of finger pairs can cause reduced performance. Frequency response of IDTs are further tunable with a method called apodization, and details can be found in reference [12].

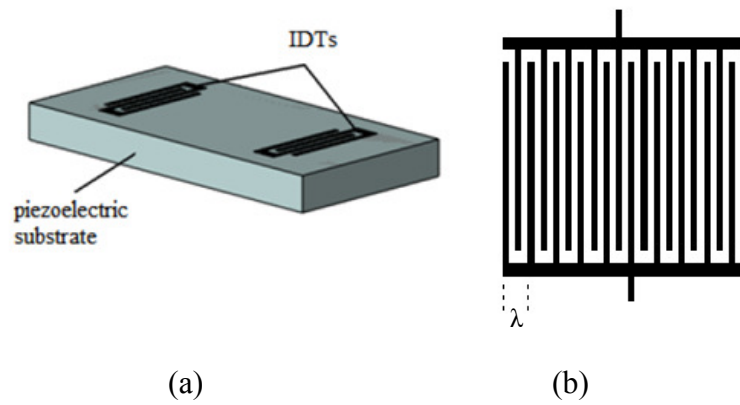


Figure 3. Interdigital transducer illustration. a) Typical IDT placement on a piezoelectric substrate [6], b) bidirectional single electrode IDT

2.2. Surface Acoustic Waves

2.2.1. Piezoelectricity

Piezoelectricity is defined as the linear coupling mechanism between elastic (or mechanical) and electrical domains [9]. It exists in anisotropic materials; with most commercially available ones having trigonal and hexagonal crystal structures. The effect is two-way (or reciprocal): when an electric field is applied on a piezoelectric material, it generates mechanical strain, which is called as the direct piezoelectric effect. The

opposite also holds, when a stress (or strain) applied to a piezoelectric material, it generates an electrical field (or charge). Piezoelectricity is caused by the unbalanced dipole moments in non-symmetrical anisotropic crystal structure [3]. For example, in a trigonal crystal structure, there is no polarization in equilibrium state. Dipole moments are balanced by each other. When an external tensile or compressive stress is applied on the trigonal crystal, the orientation of the structure does not allow auto-balancing of dipole moments [10]. A net positive or negative polarization occurs, causing charge generation in the material, which is referred as the piezoelectricity. Reciprocally applied charge or dipole moments cause elastic stress (or strain).

The governing equations of piezoelectricity are the coupled equations in mechanical and electrical domain [9]:

$$D_i = \epsilon_{ij}^T E_j + d_{ijk} T_{jk} \quad (1)$$

$$S_{ij} = \underline{d}_{ijk} E_k + s_{ijkl}^E T_{kl} \quad (2)$$

where matrices D is electrical displacement, E is electrical field, ϵ is dielectric constant, d_{ijk} and \underline{d}_{ijk} are piezoelectric strain constants, T is stress, S is strain, and s is stiffness. The subscripts i, j, k , and l define related tensors. Depending on the crystallographic structure, all these matrices have different symmetry lines, which can be found in detail at reference [3]. Transformation matrices of these parameters and equations are also available in the reference, which is beyond the scope of this dissertation and will not be described in detail.

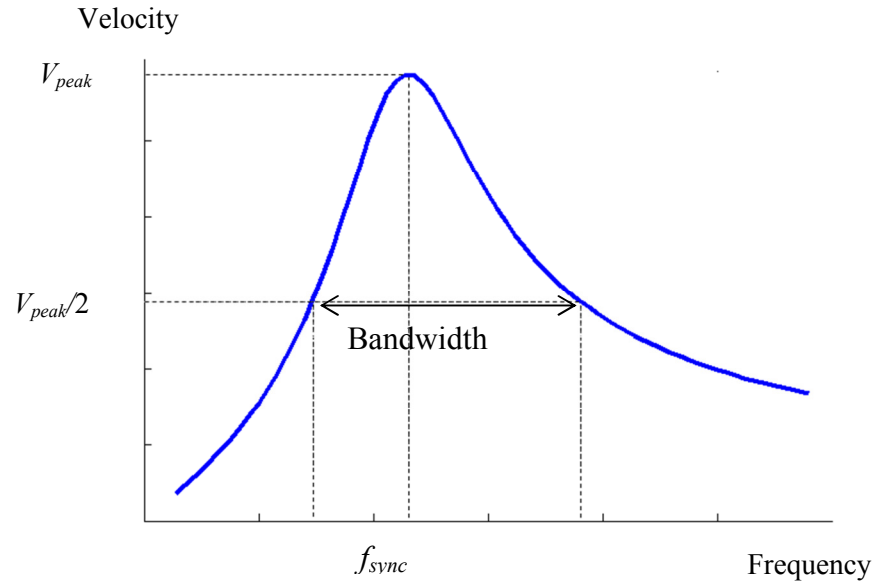


Figure 4. SAW synchronous frequency and bandwidth

In materials with weak piezoelectricity, the wave motion can be uncoupled with electrical domain, i.e. effect of piezoelectricity can be neglected in wave propagation [9]. Anisotropic nature of the piezoelectric materials with different characteristics enable propagation of various modes of acoustic waves such as; bulk acoustic waves, Rayleigh waves, shear horizontal and shear vertical surface acoustic waves, Lamb waves and surface skimming bulk waves; with different designs. The propagating wave type is determined by material type, cut, rotation angle of the cut, propagation direction, and substrate thickness. Wave types and related parameters will be discussed in detail at the next sections.

2.2.2. Materials and Crystal Cuts

As discussed in previous section, piezoelectric material type and cut are the major parameters that determine wave type and propagation characteristics. Extensive information and knowledge is present in the literature on piezoelectric materials and cuts in references such as [3, 9, 10, 12]. Material properties, elastic constants and dielectric properties of typical piezoelectric materials and cuts can be found in these references.

In acoustic wave literature, cuts are designated with respect to the normal of the material face. The surface of a X-cut material has its surface normal oriented parallel to the x-axis of the material crystallographic direction [9]. Similarly, the Y- and Z- cuts have their surface normal in Y- and Z-directions. Another important parameter is the rotation of the crystal cut. It represents the rotation of the crystal in degrees, around that axis. The crystal properties of a piezoelectric substrate are often designated as: 'degrees of rotation', 'cut type', 'wave propagation direction' and 'substrate material'. For example: "36° YX LiTaO₃" is the 36 degrees rotated (with respect to the crystallographic X-axis), Y-cut, X polarized lithium tantalate substrate. In the existing literature the word 'propagating' is often confusing because of its different use by different authors. As in [9], an "x-propagating wave" corresponds to propagation plane, but at some other sources, it is related with propagation direction of the wave. In this manuscript, "X-cut, Y- propagating wave" is used as wave motion in the plane, with its surface normal in x-direction and the wave is polarized in y-direction.

The selection of cut and direction is determined by several parameters depending on the application. Electromechanical coupling coefficient, temperature stability,

propagation characteristics, attenuation, and phase velocity of the propagating wave are the major parameters in material and cut selection.

Electromechanical coupling coefficient (k^2), is a measure of efficiency of energy conversion between electrical and mechanical domains. High k^2 is preferable for wideband devices and when use of multiple propagation modes are desired, and low k^2 is preferable for narrowband applications [2]. Thermally stable cuts are often preferred in sensing applications, to eliminate the need for temperature compensation. Type of anisotropy of the cut and the thickness of the material enables propagation of various modes such as acoustic plate modes, flexural plate modes, Rayleigh surface waves, thickness shear mode, and shear horizontal waves [2]. The degree of leakiness of propagating waves is also determined by the cut and direction. Attenuation is especially important for devices performance, when low insertion loss is obligatory, such as RF filters. Phase velocity is also affected by the cut and direction of same material. Usually higher phase velocities are desirable enabling higher frequency devices with same dimensions. However, higher frequency means higher wave attenuation [2]. Most of the time, it is not possible to have optimal values for all the parameters, so design trade-offs should be made to pick the most suitable material and cut for specific application.

2.2.3. Rayleigh Surface Acoustic Waves

Surface acoustic wave theory was first presented by Lord Rayleigh in 1896 [13]. The surface acoustic waves presented were elastic waves in the material surface with penetration depth being only a couple of wavelengths. The particle motion associated

with the wave was a circular motion at the surface in the plane formed by the propagation direction and normal to the surface, as presented in Figure 1-a.

Rayleigh SAWs can be excited with IDTs on some specific cuts of piezoelectric materials easily. Popular materials and cuts are ST-Cut Quartz ($V_p = 3200$ m/s) and 128° YX Lithium Niobate ($V_p = 4000$ m/s) with x-axis propagation for both [2]. Electromechanical coupling coefficients of Rayleigh SAWs are smaller compared with SH SAWs, but they usually show high energy concentration in the propagating mode. They propagate on the free surface without significant leak. High energy concentration on the surfaces enables use of them as strain [14], and temperature sensors[15] ensuring free surface boundary condition is satisfied. There are also reported mass loading sensor applications of Rayleigh SAWs from gas phase as in reference [16]. However, when immersed in liquids (i.e. the free surface boundary condition is disturbed), the particle motion couples with the surrounding fluid medium. SAWs leak energy into compressional waves in liquids. This coupling renders Rayleigh SAWs almost insensitive to liquid loading. This condition necessitates use of shear horizontal SAWs for immersion or liquid-loaded sensors.

2.2.4. Shear Horizontal SAWs

Several decades after Rayleigh SAWs were discovered and implemented, shear horizontal (SH) SAWs were presented in late 60s by Bleustein [17] and Gulyaev [18] separately. Similar to Rayleigh SAWs, SH SAWs propagate on the surface of materials but with particle displacement being on the plane of surface as presented in Figure 1-b.

The particle motion parallel to surface plane enables immersion operation, because SH waves do not significantly couple to compressional waves in liquids, unlike Rayleigh waves. They usually constitute higher electromechanical coefficients and phase velocities than Rayleigh waves. However, their propagation nature is leakier: even in the special cuts with least significant attenuation, i.e. the SH waves couple to shear vertical and longitudinal modes. When enhanced sensitivity is essential, this leaky nature is usually problematic, and requires special treatment to further confine energy in the surface. The two main approaches used are: surface transverse waves (STWs) and Love waves, which will be discussed next.

Surface skimming bulk waves (SSBW) are also shear horizontal polarized waves very similar to SH waves, and given a different name, because the leak angle is usually higher than SH SAWs. The name is used often in literature; however there is no widely accepted criterion whether a wave should be named as SH wave or SSBW.

SAW biosensing applications became realizable after discovery and use of SH SAWs, because of their immersion capability. The nature of biological analytes usually requires sensing in liquid, mostly in aqueous environment. The typical materials and cuts for SH SAWs and SSBWs are, ST-Cut quartz, 41° YX LiNbO₃, (lithium niobate) 64° YX LiNbO₃, 36° YX LiTaO₃ (lithium tantalate), potassium niobate (KNbO₃) and langasite (pure SH waves) [6]. Material and SAW properties of these cuts of materials can be found in detail at references [10, 19].

2.2.4.1. Shear Transverse Waves

Surface transverse wave devices were developed on materials that can support a SH SAW or SSBW. Metal gratings, usually fabricated during IDT fabrication, placed parallel to IDT fingers causes energy trapping effect by slowing the wave, enhancing its surface mass sensitivity [6] (Figure 2-b).

The SSBWs was firstly presented by in 1977 [20, 21], but high insertion loss from radiation into the bulk of the substrate was also reported. The first successful STW device was presented by Bagwell and Bray in 1987 [22]. However, no clear optimal design parameters have been presented with true understanding of STWs, despite numerous studies presented up-to-date [6, 23].

2.2.4.2. Love Waves

Love wave devices, similar to STWs, were developed for confining acoustic energy to surface. Love waves or Love wave devices are fabricated by introducing a thin guiding layer, usually thin films or polymers, on top of a SH SAW or SSBW propagating surface (Figure 2-a). First Love wave device was presented by Du and Harding [7] and they were shown to have increased sensitivity. The thin guiding layers, of which bulk shear velocity should be less than the substrate [7], acts similar to gratings of STW for confining the wave on the surface. The guiding layer can either cover the entire sensor surface area including IDTs and delay line; or IDTs only [24]. Several studies presented that Love waves increase sensitivity of the mass loading sensors (less with only-IDT

coverage) [24]. The guiding layers can be comprised of polymers such as photoresist [25], Parylene C [26], Zinc oxide [27, 28] or chemical vapor deposited SiO₂ [29]. The guiding layer is not only helpful for energy confinement, but further protects IDTs from harsh chemicals and other surface treatments that are involved especially in biosensing. The degree of wave confinement determines the sensitivity, however it has been presented that this effect is valid up to some guiding layer thickness [30]. The effective thickness range depends on the operating frequency, substrate type and design. It was shown that below this optimum range, energy confinement is not significant; and above this range high attenuation is observed, resulting in high insertion loss [30]. Similar to STWs, the physics of Love waves investigated extensively [31, 32], however models still fail to show optimum solutions and to explain high attenuation for thick guiding layers.

2.3. SAW Biosensors

The first application of SAW devices as mass-sensors was in 1979 by Wohltjen and Dessy for gas detection [33-35]. Later, in the 80s, early attempts to transfer the simple method of SAW gas sensing to a biosensor were less successful [36-38]. The reason was that these devices utilizing Rayleigh waves were unable to operate efficiently in contact with liquids. As discussed in previous sections, to avoid the high attenuation caused by the liquids, the acoustic waves must be of shear horizontal polarization. The first successful approaches of using liquid-loaded SAW devices were not achieved until 1987 [39, 40]; with shear horizontal polarized waves. Another approach used for facing this problem was the use of APM devices (SH-APM and FPW), which have been

reported to work efficiently in liquid media [6]. However, their operation frequencies are limited and they are very fragile due to the thin membrane utilized in the design. Thus, in the last decades, SAW devices have gained extensive attention for biosensing applications. Up-to-date, there are numerous SH SAW based biosensors reported for detecting proteins, DNA, viruses, bacteria and cells [36]. Along with several different substrate and guiding materials, several detection mechanisms have been presented, which are summarized in Table 1 for immunosensing.

2.3.1. Measurement Methods and Sensor Configurations

SAW sensors are most typically used in three different electronic configurations: oscillator, vector voltmeter and network analyzer; as illustrated in Figure 5 a-c [6, 41]. Oscillator or the oscillatory circuit is the most popular and the least expensive method utilizing the sensor as the feedback element of an amplifier (Figure 5-a). In this configuration, the sensor is used as a filter that determines the oscillation frequency through the circuit. The sensing is monitored by the oscillation frequency change, which is caused by the change in wave propagation characteristics, specifically wave speed and phase. A digital frequency counter or an oscilloscope is used for measurements. It is regarded as the simplest method with its inexpensiveness and ease of operation, but the only measurable output parameter is the frequency [6]. Signal amplitude and phase information are sometimes required for sensing purposes, but they cannot be extracted using this method. If the sensor response contains several strong peaks, use of filters in the circuit is essential to ensure the oscillation at the desired mode. Simplicity of the

system and possibility of miniaturizing the amplifier and frequency counter to an integrated system makes it one of the most promising methods for remote settings, even with the aforementioned problems.

Vector voltmeter method utilizes a signal generator and a vector voltmeter in addition to the sensor Figure 5-b [6, 41]. In this method, one IDT is fed with a signal at the synchronous frequency of the sensor, usually in bursts by the signal generator, accompanied with an amplifier. The output is obtained from the other IDT by connecting it to a vector voltmeter, by which the phase and signal amplitude is monitored. A data acquisition system or an oscilloscope might be substituted for the voltmeter, by which the frequency change can also be monitored. One drawback of this method is it usually requires further data processing, which makes real time monitoring challenging. The sensitivity is also limited by the resolution of the voltmeter.

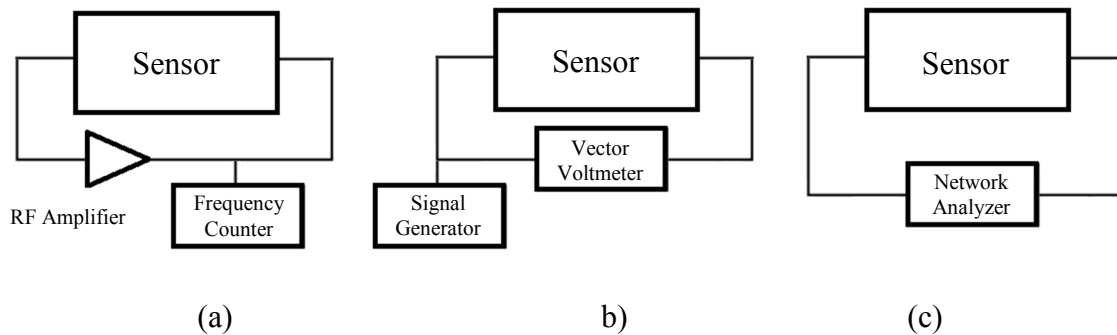


Figure 5. SAW sensor measurement methods. a) oscillatory circuit, b) vector voltmeter, c) network analyzer.

Network analyzer is the third method, which uses the same principle as the voltmeter with an integrated plug-and-play device called vector network analyzers as illustrated in Figure 5-c [41]. A network analyzer is more expensive (compared with

other alternatives) equipment that is capable of measuring one port or two port impedance, insertion loss, phase, and several other measurements real time. It enables complicated measurements of capacitance, resistance and inductance with a programmable interface. The drawback of network analyzers is that they are bulky, expensive and fragile. On the other hand, they enable numerous measurements for the same system without significant extra effort. They are more frequently used in development stages of the sensing systems.

SAW sensors can also be utilized in different configurations in the device level, depending on the application. Delay path configuration consists of two IDTs separated by a distance (or delay line), much larger than the SAW wavelength as illustrated previously in Figure 3-a. The actual sensing takes place on the delay path with the perturbations acting on the propagating wave. Delay line devices suffer from high insertion losses due to attenuation, since the acoustic waves have to travel long distances on the sensor surface. They enable sample placement far from IDTs. On the other hand, usually a sealed chamber is required on the delay path, which causes further attenuation, drift, extra noise, and instability [6].

Resonator configuration also contains IDTs, with less number of IDT pairs compared with delay path configuration. Resonator uses grating or reflectors placed on either sides of the IDTs, as seen in Figure 6-a. The wave reflections from the reflectors constructively form a signal with more significant or pronounced peaks at the design frequency (compared with delay path) [2]. Resonators offer sharper resonances, low insertion loss, and more linear phase response. The resonator can be designed as either two-port (can be used similar to delay path configuration) or one-port [6]. The

perturbations should usually act upon the whole sensor surface including IDTs and the reflectors. This necessitates use of protective and shielding layers on top of the surface. These layers can be also used for further confining SAW energy to the surface, as Love wave devices.

There are several approaches to eliminate the effect of temperature with most typically used method being dual-channel sensor configuration. This method involves use of two sensors simultaneously, with one used as the actual sensor, and the other one is used as a reference [2]. For example, in a typical dual channel SAW immunosensor, the two sensors are prepared exactly the same except one of the sensors, which does not contain any antibodies for the target analyte. Two sensors are run with exact same periphery and same solution/liquid under same environmental conditions, or in a custom differential amplifier design. Reference sensor is perturbed by all the perturbations as the actual sensor, but not by target analyte. The drift of the reference sensor is then subtracted from the actual sensor response, and thus other effects are eliminated. In the case of differential amplifier, only the difference can be monitored. Crosstalk between sensors is problematic and there has been discussions on usefulness of the method [6]. It should be noted that biosensors are more complex compared with other sensors, thus are not easy to operate under exactly the same conditions. Another possible approach is using a single sensor firstly for the reference and then for the actual test, and eliminating other effects again by subtraction of two results.

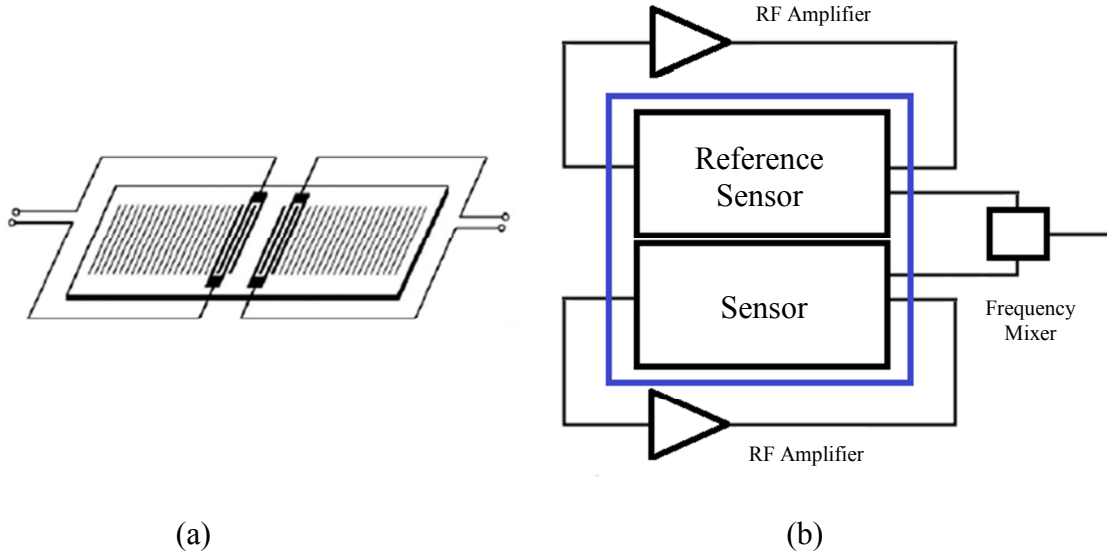


Figure 6. SAW sensor configurations. (a) a two-port resonator [6], (b) dual line configuration.

Antigen and pathogen identification and quantification assays used to mainly rely on plating, culture methods, biochemical testing, microscopy [6]. Over the last decades, several new methods including immunological methods, polymerase chain reaction (PCR) and biosensors have been developed, which provide better specificity and more rapid testing compared to traditional techniques [6, 42]. Immunological detection with antibodies (or immunosensors) is the most widely used technique as a standard for detection of biomarkers, cells, spores, viruses, DNA hybridization, gene mutations and toxins alike [36, 43]. The availability and ease of generation of antibodies, together with the emergence of several transduction mechanisms, has made immunosensing sensitive, specific, reproducible and reliable [6].

SAW immunosensors utilize selective detection of target analytes using antibody-antigen interactions. Either antigens or antibodies can be immobilized on the acoustic device for sensing purposes. The immobilization procedure of these molecules should

ensure specificity, sensitivity, and reproducibility. Covalent binding is usually utilized in sensing layer formation of SAW immunosensors with retention of biological activity of biomolecules after immobilization [6]. Self-assembled monolayers (SAMs) are frequently employed, enabling formation of monomolecular layers of biological molecules. These monolayers can be formed on a variety of substrates and materials with proper surface activation and on top of each other by covalent binding.

Piezoelectric devices with different wave modes, substrates, cuts and methods as discussed in previous sections have widely been employed for immunosensors. SAW immunosensors usually utilize SH SAWs either bare or in STWs or Love waves to quantify target analytes in liquid solutions (mostly aqueous). Antibodies derived from mouse, goat or rabbit are frequently used for specific sensing of target biological analytes. Surface activation to achieve bio-molecule immobilization can be utilized by several methods. Gold surfaces allow the use of functionalized thiols and SiO₂ surfaces enable use of various silanes [6]. Immobilization and specificity is ensured after surface activation using, protein A, G and A/G avidin-biotin interactions using biotinylated antibodies, photo-activated dextrans, lipids, hydrogel layers, and fullrenes [36]. All these methods form monolayers of active or passive groups for the subsequent coupling of biomolecules onto the transducer surface. As mentioned before immobilization methods should usually be optimized specific to application.

Proper orientation of antibodies in immunosensors is also essential for most effective target capture. The antibodies should be immobilized on the sensor surface from their constant regions, with active regions free to capture target analyte. Protein A, Protein G and Protein A/G can be utilized after surface activation to ensure proper

antibody orientation as presented in several studies [5, 8, 44-48]. Non-specific binding on uncovered areas of sensor surface should also be avoided by use of other surface treatments such as polymers [5] and hydrogels [36].

To date, there are numerous reported immunosensor applications, utilizing several designs with different methods, SAW types, configurations, materials and surface treatments. SAW Immunosensing applications that were reported up to date are summarized in Table 1, under several headings; however details of each work will not be discussed one by one. One can refer to excellent review papers for detailed information on specific works, such as [6, 36, 41]. In the ‘target analyte’ column the target species to be captured and sensed by the sensor is given; the “coatings” column includes the guiding layers and applied surface treatments; the ‘immobilized’ column contains the information on what species immobilized on sensor surface to capture the target analyte and the ‘device type’ column show SAW device type and used substrate material. As seen from the table, several different designs have been used with a wide variety of different materials, methods, chemicals, for several applications.

Table 1. A summary of immunosensor applications reported in literature.

Detection of Proteins via Direct Immobilization				
Target Analyte	Coatings	Immobilized	Device Type	Reference
IgG	-	Anti-IgG	STW, Quartz	Baer et al. 1992 [49]
Glucose Oxidase	-	Anti-glucose Oxidase	SH, LiTaO3	Rapp et al. 1993[50]
Glucose Oxidase	Polyimide (cyano transfer/TRIMID)			Wessa et al. 1999[51]
Anti IgG & Protein A	PMMA + Gold	IgG	Love ,Quartz	Gizeli 1992 [52]

Table 1. (Continued)

IgG	PMMA & Novalac PR + gold	Protein A	Love, Quartz	Rasmusson & Gizeli 2001 [53]
	PR + gold		Love, LiTaO3 and Quartz	Saha et al. [54], Gizeli et al. 2003[55]
	gold		Quartz, STW	Leidl et al. 1997 [56]
	-		SH, LiTaO3	Hoummady 1997[57]
Anti IgG	SiO2	IgG	Love, Quartz	Harding et al. 1997 [58]
	PMMA, Cyanethylcellulose	IgG	Love, LiTaO3	Josse et al. 2001 [59]
Thrombin	SiO2 + gold	Thrombin DNA aptemers	Love, Quartz	Schlenso 2004 [60]
Blood coagulation cascade	SiO2 + gold	Thrombin DNA aptemers	Love, Quartz	Gronewold 2005 [61]
Thrombin	SiO2 + gold	Anti-thrombin	Love, Quartz	Perpeet 2006[62]
Detection of Proteins via immobilization by Protein A & G, Dextran, Streptavidin-Biotin				
IgG, Anti-human Serum Albumin (anti-HSA)	Gold + Protein A	Anti-IgG, HSA	SH, LiTaO3	Welsch 1996 [45]
IgG	Protein A	anti-IgG	SH, LiTaO3	Freudenberg et al. 1999 [47], 2001 [46]
IgG	Gold + Alkanethiol +Protein A	Anti-IgG	SH, LiTaO3	Kwon and Roh, 2004 [48]
Bcl-2	ODMS+Protein A/G	Anti-Bcl-2	SH, Quartz	Onen et al. 2012 [5]
Urease	Polyimide or Parylene C+ copolymer (carboxymethylated dextran and BSA)	Anti-Urease	SH, LiTaO3	Wessa et al. 1998 [63]
IgG		Anti-IgG	SH, LiTaO3	Barie et al. 1999 [64]
Ostrogen receptor/ Anti-Urease	Optodextran	Estradiol/ Urease	SH, LiTaO3	Lange et al. 2003 [65]
Anti-folic Acid	Parylene C - Aminodextran	Folic Acid	SH, LiTaO3	Lange et al. 2007 [26]
Breast cancer biomarker, Mammoglobin (hMAM)	Streptavidin-biotin	Anti -HMAM	Love, CMOS ZnO	Tigli 2010 [66]
HER-2-neu (breast cancer biomarker)				

Table 1. (Continued)

Detection of DNA (hybridization) and Cells				
15-mer Oligonucleotide (responsible for Hunter syndrome)	Gold + Protein A	Anti-IgG	SH, LiTaO3	Welsch 1996 [45]
P53 gene fragment (exchange or deletions for cancer related mutations)	SiO ₂ +gold+dextran+probe oligonucleotides	Probe oligonucleotides	Love, Quartz	Gronewold, 2006 [68]
Cancer cells by CD-4 proteins	SiO ₂ , Gold, 11-mercaptoundecanoic acid, carboxyl activation	Anti-CD-4	Love, Quartz, Nanopatterning	Broker et al. 2012 [69]
JEG-3				
Lymphoblastic leukemia and MOLT-17 (choriocarcinoma)				
Class I Major Histocompatibility Complex molecule HLA-A2 on the surface of whole cells	Gold + Protein G	Anti HLA-A2	Love, Quartz	Saitakis et al., 2010 [70]
Receptor-specific ligand binding (octapamine hydroxide)	-	Sf-9 Insect cells	SH - LiTaO3	Racz et al. 2011 [71]
Detection of Bacteria & Virus				
Anti-M13 bacteriophage	SiO ₂	M13 Bacteriophage	Love, Quartz	Tamarin et al. 2003 [72]
Anti-E-coli and Anti-Legionella	SiO ₂	E-coli and Legionella	Love, Quartz	Howe and Harding 2000 [73]
E-coli and Legionella Analyte + Antibodies	SiO ₂	Anti-species Antibody	Love, Quartz	Moll et al. 2007 [74]
B8 Bacillus Thuringiensis (Anthraxis stimulant)	Polyimide or Polystyrene, Protein G	Anti-B8	Love, LiTaO3	Branch and Brozik 2004 [75]
E-coli	Gold, PEG	Anti-E-Coli	Langasite	Berkenpas, 2006 [76]
Coxsackie virus B4 and Sin Nombre virus (SNV)	NeutrAvidin	Unlabeled antibodies (for SNV) or with biotinylated	Love, LiTaO3	Bisoffii et al. 2008 [77]
	Biotin Binding Protein (for B4)	Antibodies (B4)		

2.3.2. Overview of Existing Literature

The pioneering SAW immunosensing studies, starting from Baer et al. focused on proof of concept mainly using IgG antibodies and anti-IgG either as target analyte or immobilized biomolecule. Successful applications have led to extensive research in the field to detect proteins, biomarkers, bacteria, virus, and DNA mutations.

- The operation frequency of the immunosensors varies from the low-MHz range up to GHz range. In theory, higher frequency leads to higher sensitivity, but there are several other parameters and trade-offs should be made for device design. First of all, higher frequency devices are costly by means of fabrication and of required electrical periphery. Fabrication of high frequency SAW immunosensors require high quality thin films, and rather expensive e-beam lithography. Also, high frequency network analyzers, power amplifiers, filters, couplers, and vector voltmeters are more expensive than their lower frequency counterparts. Another problem is that wave attenuation and related insertion loss increases with increasing frequency. It is not very problematic, when the sensing surface is in the order of couple wavelengths, however, if the sensing surface is relatively long, high insertion losses can be an issue. This not only increases amplification requirement but also causes further need for temperature compensation in temperature-unstable cuts.

- Dual line configurations in theory shows a good alternative to avoid all unwanted effects, however, it is not easy to obtain and operate two identical sensors operating exactly under same conditions. Especially, when selectivity and sensitivity in biosensors is required, the assembly includes several layers, in addition to several fabrication steps,

which makes obtaining two identical sensors problematic. Other controlled experiment techniques should be developed to enable testing on the same sensor with complete reversibility and reproducibility.

- In several recent studies, there's a clear movement towards using smaller and smaller devices for lower sample size requirement and more rapid detection, usually with integrated microfluidics. The results were successful in reaching goals; however, integration with microfluidics and handling of small sample sizes is not very easy and is costly. This trend is clearly helpful, when multiple tests should be run with very small sample sizes, such as bodily fluids or tests for biomarkers from cells extracted from cancerous tissues. Although, smaller sample sizes enables very robust detection, cost and integration problems makes small size favorable only when access to sample is very limited. The aim in the designs should focus on most feasible solution for size, cost, response time and complexity. The research should focus on designing simpler and lower cost, point of care systems, especially for detection of pathogens and viruses for global healthcare. Handling of samples and reagents should also be considered while designing systems for these purposes.

- No antibody immobilization technique has been proven to be optimal, up-to-date. Although, some studies claim the method they're using as being the most effective method, there's not a published work that compares and evaluates the methods objectively.

- SAW Immunosensors offer several advantages outlined in the previous sections, however selectivity still remains a main issue. In order for SAW Immunosensors to be a viable alternative to other well developed techniques such as SPR and immunoessays,

selectivity problem should be addressed. Selective detection of target analytes from complex solutions requires further research and new methods.

CHAPTER 3. ANALYTICAL MODELING

Acoustic propagation problem in multi-thin-layer systems is essential for understanding of gravimetric (or mass loading) sensors. The solution necessitates simultaneous solution of wave equation in each layer, with continuity of stress and displacement boundary conditions. As discussed in previous chapter, Guided or Love waves are obtained when thin mass layers are formed on top of SH SAW propagating substrates. The layers deposited, spun or grown on top have wave-guiding effect, by confining energy to surface, and increasing the sensor sensitivity.

The wave propagation and related sensitivity can be investigated in two steps. The layer guiding effect of multi-layer thin films should firstly be treated by wave equation with boundary conditions, in the form of dispersion curves. Detailed investigation of sensing mechanism with numerous parameters involved using exact analytical solutions is usually complex, and sometimes even not possible. However, sensing mechanism can be investigated by perturbation methods, which was first presented by Auld for acoustic wave propagation [9]. The method involves first or higher order approximations to exact analytical solution, which results in rather less complicated explicit or simple implicit equations.

The actual wave propagation problem on a piezoelectric substrate involves anisotropy (in substrate and possibly in guiding layer), piezoelectricity, and three dimensional wave vectors (leaky waves). Exact modeling of all these is possible,

however is very complicated and not very feasible for engineering purposes. For this reason, several reasonable simplifications and assumptions were made.

The substrate and the guiding layer were assumed as ideal elastic and isotropic materials with shear velocities equal to actual materials in the specified SH SAW direction. The substrate was assumed as non-piezoelectric; when materials with low piezoelectricity (like quartz) were considered or when there were no significant electrical field perturbations present. No significant electrical perturbation assumption is valid, when there is no short on the propagation path between IDTs physically. The leaky nature of SH or SSBW waves was also neglected, since Love waves are effective in energy confinement to the surface. The effect of the assumptions was neutralized, at the very end of section by comparisons with experimental results.

Shear horizontal polarized wave propagation was investigated step by step by dispersion solution and perturbation analysis. The sensing and wave guiding layers were modeled as elastic mass (for metal and dielectric films) and as viscoelastic layers using Maxwell's model for fluids, polymers and layers of proteins [78, 79].

A detailed parametric study on dispersion, sensitivity and perturbation analysis was done for each case and results were compared. The case and model has been investigated in several papers in literature [79-83], however, no similar detailed analysis and parametric studied have been presented elsewhere, to authors knowledge.

3.1. Analytical Modeling of Wave Propagation

3.1.1. Three Layer Model

The simplest model for the Love wave propagation involves shear horizontally polarized acoustic waves in a system of the substrate, guiding layer and the mass layer, with layer thicknesses t_s , t_g and t_m respectively. The mass layer was the layer, in which the sensing takes place with increasing mass and thickness during operation. Using the assumptions and simplifications mentioned above, the problem were treated as a two dimensional system with polarization x_2 direction and propagation in x_3 direction as presented in Figure 7.

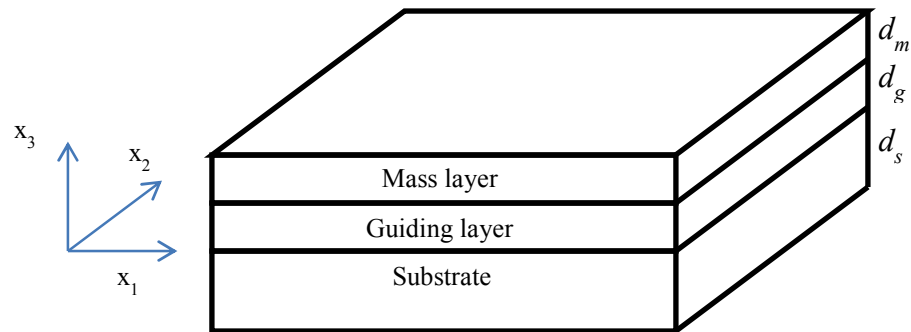


Figure 7. Overview of a three layer system

Considering wave propagation in an isotropic and non-piezoelectric medium, in which u_j is the particle displacement; ρ is the density; λ and μ are the Lamé constants and S_{ij} is the strain tensor; the equation of motion can be written as:

$$\frac{\rho \partial^2 u_j}{\partial t^2} = (\mu + \lambda) \frac{\partial S_{ij}}{\partial x_j} + \mu \nabla^2 u_j \quad (3)$$

where S_{ij} is the strain tensor:

$$S_{ij} = \frac{1}{2} \left(\frac{\partial u_i}{\partial x_j} + \frac{\partial u_j}{\partial x_i} \right) \quad (4)$$

The coordinate axes are placed such as x_1 - x_2 plane coincident with the upper surface of the substrate and x_3 as normal to this plane with $x_3 = 0$ defining the upper substrate surface, as presented in Figure 7. The solution of the multilayer wave propagation equation is done by trial solutions for displacements with propagation along the x_1 axis and displacement in x_2 axis, for SH waves. The trial solutions for substrate (s), guiding layer (g) and mass layer (m) can be constructed, satisfying these conditions:

$$u_s = (0, 1, 0) \left[A_s e^{-T_s x_3} + B_s e^{T_s x_3} \right] e^{j(\omega t - k_1 x_1)} \quad (5)$$

$$u_g = (0, 1, 0) \left[A_g e^{-jT_g x_3} + B_g e^{jT_g x_3} \right] e^{j(\omega t - k_1 x_1)} \quad (6)$$

$$u_m = (0, 1, 0) \left[A_m e^{-jT_m x_3} + B_m e^{jT_m x_3} \right] e^{j(\omega t - k_1 x_1)} \quad (7)$$

where and $k_l = \omega/v$ gives the phase speed v of the solution, $A_{s,g,m}$ and $B_{s,g,m}$ are constants that determine wave propagation characteristics and $T_{s,g,m}$ are wave vectors. Because of

initial assumption of propagation only along x_1 direction strain tensor S_{ij} can be takes as zero. Substituting trial solutions Equation (5) -(7) into Equation (3) for each layer, the wave vectors can be obtained as:

$$T_s^2 = \omega^2 \left(\frac{1}{v^2} - \frac{1}{v_s^2} \right) \quad (8)$$

$$T_g^2 = \omega^2 \left(\frac{1}{v_g^2} - \frac{1}{v^2} \right) \quad (9)$$

$$T_m^2 = \omega^2 \left(\frac{1}{v_m^2} - \frac{1}{v^2} \right) \quad (10)$$

where v_s , v_g and v_m are shear velocities of substrate, guiding layer and mass layer respectively. The resulting wave vector T_s is different from the others, because the trial solution was chosen in a way to ensure non-imaginary T_s value. This condition arises from Love wave theory, in which shear acoustic velocities of any guiding layers should be less than of the substrate. Shear velocities of isotropic, elastic materials can be calculated using shear modulus and density values with the formula $v_{s,g,m} = (\mu_{s,g,m} / \rho_{s,g,m})^{1/2}$. A love wave solution is obtained when $t_s \rightarrow \infty$. In such case, wave vector T_s is real, leading to real v_s and particle displacement decaying with depth (i.e. surface waves).

The solution to dispersion problem is obtained by applying displacement and stress boundary conditions. The displacement boundary conditions are continuity of particle displacement at interfaces and the stress boundary conditions are continuity of

stress at the interfaces and stress-free top and bottom surfaces. The displacement boundary conditions and corresponding equations are:

$$u_s(x_3 = 0) = u_g(x_3 = 0); A_s + B_s = A_g + B_g \quad (11)$$

$$u_g(x_3 = d_g) = u_m(x_3 = d_g); A_g e^{-jT_g d_g} + B_g e^{jT_g d_g} = A_m e^{-jT_m d_g} + B_m e^{jT_m d_g} \quad (12)$$

The stress boundary condition, requires calculation of stress and in this problem, we will impose the τ_{i3} component of the stress tensor, which is given by:

$$\tau_{i3} = \delta_{i2} \mu \left(\frac{\partial u_2}{\partial x_3} \right) \quad (13)$$

Using this formula for stress, the other four boundary conditions including two continuity and two free stress conditions are as follows:

$$\tau_s(-d_s) = 0; A_s e^{T_s d_s} - B_s e^{-T_s d_s} = 0 \quad (14)$$

$$\tau_m(d_m + d_g) = 0; A_m e^{-jT_m(d_m + d_g)} - B_m e^{jT_m(d_m + d_g)} = 0 \quad (15)$$

$$\tau_s(0) = \tau_g(0); \quad (16)$$

$$\mu_s T_s A_s - \mu_s T_s B_s = j \mu_g T_g A_g - j \mu_g T_g B_g$$

$$\tau_g(d_g) = \tau_m(d_g);$$

(17)

$$j \mu_g T_g A_g e^{-j T_g d_g} - j \mu_g T_g B_g e^{j T_g d_g} = j \mu_m T_m A_m e^{-j T_m d_g} - j \mu_m T_m B_m e^{j T_m d_g}$$

The dispersion problem defined by these set of six equations with six unknowns, can be solved simultaneously using a matrix approach by defining constants ξ_{sg} and ξ_{mg} :

$$\xi_{sg} = \frac{\mu_s T_s}{\mu_g T_g} \quad (18)$$

$$\xi_{mg} = \frac{\mu_m T_m}{\mu_g T_g} \quad (19)$$

The system of equation can then be written in matrix form as:

$$\begin{pmatrix} 1 & 1 & -1 & -1 & 0 & 0 \\ 0 & 0 & e^{-j T_g d_g} & e^{j T_g d_g} & -e^{-j T_m d_g} & -e^{j T_m d_g} \\ e^{T_s d_s} & -e^{-T_s d_s} & 0 & 0 & 0 & 0 \\ 0 & 0 & 0 & 0 & e^{-j T_m (d_m + d_g)} & -e^{j T_m (d_m + d_g)} \\ 1 & -1 & -j \xi_{sg} & j \xi_{sg} & 0 & 0 \\ 0 & 0 & e^{-j T_g d_g} & -e^{j T_g d_g} & -\xi_{mg} e^{-j T_m d_g} & \xi_{mg} e^{j T_m d_g} \end{pmatrix} \begin{bmatrix} A_s \\ B_s \\ A_g \\ B_g \\ A_m \\ B_m \end{bmatrix} = \begin{bmatrix} 0 \\ 0 \\ 0 \\ 0 \\ 0 \\ 0 \end{bmatrix} \quad (20)$$

In order to have a non-trivial solution, the determinant of the first matrix should be equal to zero. The values of v satisfying this equality are the phase velocities of the system for any given set of parameters. The dispersion equation after extensive algebraic manipulation has presented in the reference [79], and also verified by the author as

$$\tan(T_g d_g) = \xi_{sg} \tanh(T_s d_s) - \xi_{mg} \tan(T_m d_m) \left[1 + \xi_{sg} \tan(T_g d_g) \tanh(T_s d_s) \right] \quad (21)$$

Note that, the dispersion equation (21), represents the three layer system with substrate s , guiding layer g and perturbing mass layer m . Solution to system with substrate and guiding layer, without the mass layer, can be obtained by setting mass layer thickness d_m to zero.

3.1.2. Generalized Model of a N Layer System

The system represented by matrix equation (20) with two additional layers on top of the substrate, can be expanded to a system of infinite number of layers on top of a substrate. This multilayer system approach would essentially helpful for modeling sensors, which requires numerous different intermediate layers to achieve sensing. For expanding the model to multilayer system, let us firstly consider another (third) viscoelastic layer with subscript f . Similar to previous derivation, assume a trial solution u_f with the wave vector T_f and thickness d_f :

$$u_f = (0, 1, 0) \left[A_f e^{-jT_f x_3} + B_f e^{jT_f x_3} \right] e^{j(\omega t - k_1 x_1)} \quad (22)$$

$$T_f^2 = \omega^2 \left(\frac{1}{v_f^2} - \frac{1}{v} \right) \quad (23)$$

The additional boundary conditions, similar to equations (11) to (17); are continuity of displacement at $x_3=d_m+d_g$, and the stress free surface of the top layer at $x_3=d_m+d_g+d_f$. The additional boundary conditions corresponding to these are:

$$u_m(d_g + d_m) = u_f(d_g + d_m) \quad (24)$$

$$A_m e^{-jT_m(d_g+d_m)} + B_m e^{jT_m(d_g+d_m)} = A_f e^{-jT_f(d_g+d_m)} + B_f e^{jT_f(d_g+d_m)}$$

$$\tau_f(d_m + d_g + d_f) = 0 ; A_f e^{-jT_f(d_m+d_g+d_f)} - B_f e^{jT_f(d_m+d_g+d_f)} = 0 \quad (25)$$

Also, with the addition of the new layer, the stress free surface condition in equation (15), changes to continuity of stress at $x_3=d_m+d_g$ as:

$$\tau_m(d_m + d_g) = \tau_f(d_m + d_g) ; \quad (26)$$

$$A_m e^{-jT_m(d_m+d_g)} - B_m e^{jT_m(d_m+d_g)} = \xi_{fm} A_f e^{-jT_f(d_m+d_g)} - \xi_{fm} B_f e^{jT_f(d_m+d_g)}$$

where ξ_{fm} is defined as

$$\xi_{fm} = \frac{\mu_f T_f}{\mu_m T_m} \quad (27)$$

In order to obtain a generic system, assume the multilayer structure illustrated in Figure 8. Instead of deriving the equation from the beginning, the order of the equations can be rearranged by interchanging rows. Also, the new equations resulting from the additional layers should also be placed in order. The six equations representing boundary conditions for three layer system is reordered as: 1) $u_s(0)=u_g(0)$; 2) $\tau_s(-d_s)=0$; 3) $\tau_s(0) = \tau_g(0)$; 4) $\tau_g(d_g) = \tau_m(d_g)$ 5) $u_g(d_g)=u_m(d_g)$ 6) $\tau_m(d_g+d_m)=0$. The stress free top surface boundary condition is placed at the bottom every time, in order to avoid confusion by changing the condition to stress continuity after addition of extra layer. Placing the two new equations at the bottom with displacement continuity first and free surface at the bottom, we can obtain the dispersion system for 4 layer system as in equation (28).

Consider a general system, in which the layer subscripts starts with 1 for the layer at the top of the substrate and up to i layers, that are placed on top of each other. In this case, the coefficient matrix is a $(2i+2)$ by $(2i+2)$ matrix, which was a 6x6 matrix for the three layer case given in equation (20). Following the pattern and the formula for the matrix; one can find that, each additional layer adds two extra rows and columns to the coefficient matrix. The elements in the new rows are all zero except for six elements.

A system composed of the substrate and i number of additional layers, with formulas of the added elements is given in equation (29). Note that the two non-zero elements added at the last row of previous layer ($a_{2i,2i+1}$ and $a_{2i,2i+2}$) represents continuity of stress between the layers; the row before the last row with non-zero elements $a_{2i+1,2i-1}$,

$a_{2i+1,2i}$, $a_{2i,2i+1}$ and $a_{2i,2i+2}$ is the displacement continuity, and last row with non-zero elements $a_{2i+2,2i+1}$ and $a_{2i+2,2i+2}$ is the top free surface. Another advantage of this representation is that, it already lists down the dispersion equation of the simpler systems. The first 4x4 matrix represents the two layer system, and 6x6 matrix represents the three layer system.

In this study, closed form equations up to 4 layers are presented. Beyond that, the approach should involve implicit solution of the coefficient matrix, which requires extensive computing and advanced numerical solution approaches.

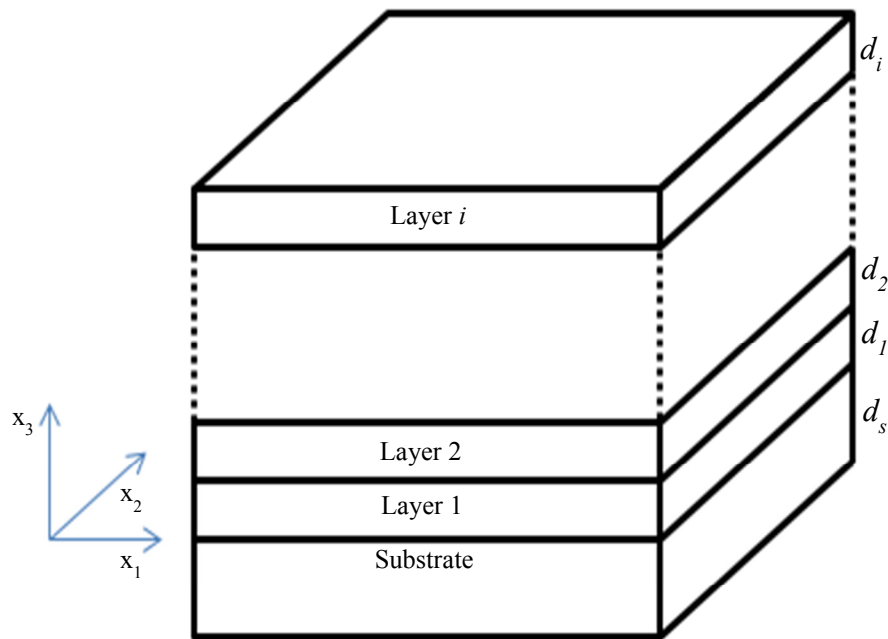


Figure 8. Generalized system with $N=i+1$ layers.

$$\begin{pmatrix}
1 & 1 & -1 & -1 & 0 & 0 & 0 & 0 \\
e^{T_s d_s} & -e^{-T_s d_s} & 0 & 0 & 0 & 0 & 0 & 0 \\
1 & -1 & -j\xi_{sg} & j\xi_{sg} & 0 & 0 & 0 & 0 \\
0 & 0 & e^{-jT_g d_g} & -e^{jT_g d_g} & -\xi_{mg} e^{-jT_m d_g} & \xi_{mg} e^{jT_m d_g} & 0 & 0 \\
0 & 0 & e^{-jT_g d_g} & e^{jT_g d_g} & -e^{-jT_m d_g} & -e^{jT_m d_g} & 0 & 0 \\
0 & 0 & 0 & 0 & e^{-jT_m (d_m + d_g)} & -e^{jT_m (d_m + d_g)} & -\xi_{fm} e^{-jT_f (d_m + d_g)} & \xi_{fm} e^{jT_f (d_m + d_g)} \\
0 & 0 & 0 & 0 & e^{-jT_m (d_m + d_g)} & e^{jT_m (d_m + d_g)} & -e^{-jT_f (d_m + d_g)} & -e^{jT_f (d_m + d_g)} \\
0 & 0 & 0 & 0 & 0 & 0 & e^{-jT_f (d_m + d_g + d_f)} & e^{-jT_f (d_m + d_g + d_f)}
\end{pmatrix}
\begin{pmatrix}
A_s \\
B_s \\
A_g \\
B_g \\
A_m \\
B_m \\
A_f \\
B_f
\end{pmatrix}
=
\begin{pmatrix}
0 \\
0 \\
0 \\
0 \\
0 \\
0 \\
0 \\
0
\end{pmatrix}
\quad (28)$$

$$\begin{pmatrix}
1 & 1 & -1 & -1 & 0 & 0 & 0 & 0 & . & . & 0 & 0 \\
e^{T_i d_i} & -e^{-T_i d_i} & 0 & 0 & 0 & 0 & 0 & 0 & . & . & 0 & 0 \\
1 & -1 & -j\xi_{s1} & j\xi_{s1} & 0 & 0 & 0 & 0 & . & . & 0 & 0 \\
0 & 0 & e^{-jT_1 d_1} & -e^{jT_1 d_1} & -\xi_{21} e^{-jT_2 d_1} & \xi_{21} e^{jT_2 d_1} & 0 & 0 & . & . & 0 & 0 \\
0 & 0 & e^{-jT_1 d_1} & e^{jT_1 d_1} & -e^{-jT_2 d_1} & -e^{jT_2 d_1} & 0 & 0 & . & . & 0 & 0 \\
0 & 0 & 0 & 0 & e^{-jT_2 (d_2 + d_1)} & -e^{jT_2 (d_2 + d_1)} & -\xi_{32} e^{-jT_3 (d_2 + d_1)} & \xi_{32} e^{jT_3 (d_2 + d_1)} & . & . & 0 & 0 \\
0 & 0 & 0 & 0 & e^{-jT_2 (d_2 + d_1)} & e^{jT_2 (d_2 + d_1)} & -e^{-jT_3 (d_2 + d_1)} & -e^{jT_3 (d_2 + d_1)} & . & . & 0 & 0 \\
0 & 0 & 0 & 0 & 0 & 0 & e^{-jT_3 (d_3 + d_2 + d_1)} & -e^{jT_3 (d_3 + d_2 + d_1)} & . & . & 0 & 0 \\
. & . & . & . & . & . & . & . & . & . & 0 & 0 \\
. & . & . & . & . & . & . & . & . & . & \xi_{i,i-1} e^{-jT_i \sum_0^{i-1} d_i} & \xi_{i,i-1} e^{jT_i \sum_0^{i-1} d_i} \\
0 & 0 & 0 & 0 & 0 & 0 & 0 & 0 & e^{-jT_{i-1} \sum_0^{i-1} d_i} & e^{jT_{i-1} \sum_0^{i-1} d_i} & -e^{-jT_i \sum_0^{i-1} d_i} & -e^{jT_i \sum_0^{i-1} d_i} \\
0 & 0 & 0 & 0 & 0 & 0 & 0 & 0 & 0 & 0 & e^{-jT_i \sum_0^1 d_i} & -e^{jT_i \sum_0^1 d_i}
\end{pmatrix}
\begin{pmatrix}
A_s \\
B_s \\
A_1 \\
B_1 \\
A_2 \\
B_2 \\
A_3 \\
B_3 \\
. \\
. \\
A_i \\
B_i
\end{pmatrix}
=
\begin{pmatrix}
0 \\
0 \\
0 \\
0 \\
0 \\
0 \\
0 \\
0 \\
0 \\
0 \\
0 \\
0
\end{pmatrix}
\quad (29)$$

3.2. Maxwell's Viscoelasticity Model

As discussed previously, biosensors usually work under liquid loading, mostly with aqueous solutions. Furthermore, intermediate layers employed for biosensing, such as polymer coatings (SU-8, Parylene, PMMA) and organic layers of proteins, antibodies, which act like rubbery polymers [78]. As the name implies, viscoelasticity represents the transitional behavior between viscous (fluids) and elastic (solids) materials. Assuming a viscous and incompressible fluid and negligible pressure gradient, Navier-Stokes equation can be reduced to:

$$\frac{\partial v_{ve}}{\partial t} = \frac{\eta_{ve}}{\rho_{ve}} \nabla^2 v_{ve} \quad (30)$$

in which, v_{ve} is the fluid velocity and η_{ve} is the dynamic viscosity of the fluid. Similar to procedure applied in previous section, assume a trial solution with a complex time dependence such as $v_{ve} = v_{ve} e^{j\omega t}$, Equation (30) can be rewritten, with particle displacement u_{ve} as

$$\rho_{ve} \frac{\partial^2 u_{ve}}{\partial t^2} = j\omega \eta_{ve} \nabla^2 u_{ve} \quad (31)$$

The equation, rewritten with particle displacement is very similar to equation (3) without the strain tensor; and shear modulus μ replaced by the Newtonian fluid viscosity factor $j\omega\eta_f$. A similar replacement can also be done in the stress formula, given by

Equation (13). In Maxwell's model of viscoelasticity, real valued shear modulus μ is replaced by the complex shear modulus G with limits of μ for ideal elastic solid and $j\omega\eta_f$ for ideal elastic fluid such as:

$$G_{ve} = \frac{j\omega\eta_{ve}}{1 + j\omega\tau} \quad (32)$$

The relaxation time τ is defined such as $\tau = \eta_{ve} / \mu$; so that G_{ve} is able to represent the limiting conditions. When $\omega\tau$ approaches infinity (solid limit) and 0 (Newtonian fluid). This approach and replacing real-valued elastic shear modulus with the complex viscoelastic G_{ve} , enables us to incorporate viscoelasticity into the problem. Another important feature of the viscoelastic or any other thin films is that, whether the film can be treated as acoustically thin or thick. Acoustically thin films enable several assumptions, which are useful in simplifying solutions and perturbation equations, which will be described in detail. This differentiation can be made in viscoelastic films, by defining and investigating the viscous penetration depth. The penetration depth δ can be defined as $\delta = \sqrt{(2\eta_{ve} / \omega\rho_{ve})}$ [79]. For investigating its effect, assume the mass layer discussed in previous section is viscoelastic with T_m . Remember that, the wave vector for this layer is:

$$T_m^2 = \omega^2 \left(\frac{1}{v_m^2} - \frac{1}{v^2} \right) \quad (33)$$

with complex shear velocity v_m calculated as:

$$v_m^2 = \frac{G_m}{\rho_m} = \frac{j\omega\eta_m}{\rho_m(1+j\omega\tau)} \quad (34)$$

Substituting v_m into wave vector T_m and replacing η_m / ρ_m with $\delta^2\omega/2$, from the definition of penetration depth:

$$T_m^2 = \left(-\frac{2j(1+j\omega\tau)}{\delta^2} - \frac{\omega^2}{v^2} \right) \quad (35)$$

Equation (35) can be rewritten, using the wave number $k=\omega/v=2\pi/\lambda$ and reorganizing:

$$T_m^2 = \frac{1}{\delta^2} \left(-2j(1+j\omega\tau) - \left(2\pi \frac{\delta}{\lambda} \right)^2 \right) \quad (36)$$

In an acoustically thin film, one would expect that the wavelength is much bigger than the penetration depth, i.e. $\delta/\lambda \rightarrow 0$; the wave vector reduced to

$$T_m = \frac{1}{\delta} \sqrt{-2j(1+j\omega\tau)} \quad (37)$$

which is independent of wave speed v . Considering limits of the relaxation time $\omega\tau$: for the Newtonian fluid, wave vector is purely imaginary meaning damped oscillations and for elastic solid, is purely real with undamped wave propagation.

Another important parameter that can be obtained from the analysis is the insertion loss. Insertion loss is defined as the magnitude of the signal that should be supplied to system to overcome attenuation. Hence, the imaginary part of the velocity in propagation (x_l direction) is related with attenuation, and insertion loss can be calculated with imaginary part of the wave number. The decay, or attenuation, in displacement, per an arbitrary length L in the direction x_l for the system is the $\exp(Imk_l L)$, the insertion loss in decibels per unit length can be calculated as [79]:

$$IL = 20(\log_{10} e)Im \left[\frac{\omega}{v} \right] \frac{dB}{m} \quad (38)$$

It should be noted that, the insertion values calculated from this equation, only represents losses related with system; with the assumption of lossless substrate. However, almost all typical piezoelectric materials are leaky, which means there's inevitable natural attenuation related arising from the substrate.

3.3. Numerical Solution of Dispersion Relations

3.3.1. Three Layer System

The perturbation analysis and resulting equations presented in the next chapter, relies on the dispersion solutions for the wave propagation. In the perturbation equation, perturbation caused by the mass perturbing layer will be investigated, using the dispersion curves for the system composed of substrate and the guiding layer. For this reason, the numerical solution of dispersion will be obtained for these two layers. The investigations on actual sensitivity, depending on the target quantity, will be presented at next chapter. The numerical solution of dispersion curve for substrate and guiding system involves numerical solution of equation (20) by setting d_m as 0, resulting in:

$$\tan(T_g d_g) = \xi_{sg} \tanh(T_s d_s) \quad (39)$$

The equation is implicit, which means, the roots of the equation, corresponding to phase velocities should be solved numerically. The equation can be handled numerically without significant modification, for ease of numerical solution, some additional manipulations were done. Considering the guiding layer is viscoelastic and substrate is elastic solid, equation (39) can be rearranged in the form:

$$\tan x + \left(\frac{\mu_s}{G_g} \right) \left(\frac{\beta}{x} \right) \sqrt{1 - \left(\frac{x}{\beta} \right)^2} \tan \left(\frac{\beta d_s}{d_g} \sqrt{1 - \left(\frac{x}{\beta} \right)^2} \right) = 0 \quad (40)$$

where $x = T_g d_g$, $G_g = j \rho_g v_g^{\infty 2} \omega \tau / (1 + j \omega \tau)$, $v_g = v_g^{\infty} [j \omega \tau / (1 + j \omega \tau)]^{1/2}$, v_g^{∞} is the solid limit of the shear velocity, $z = f d / v_g$, $\beta = \omega d_g (1 / v_g^2 - 1 / v_s^2)^{1/2} = 2 \pi v_g^{\infty} z (1 / v_g^2 - 1 / v_s^2)$ and using the identity $\tan(\cdot) = -j \tanh(\cdot)$.

A Matlab routine is developed, in order to solve the implicit equation in range of $0 < z < 1$, which is given in Appendix A. All the material properties and outputs are defined in one main m-file, and the problem is defined in a subroutine that is called from the main m-file. The solution of the implicit equation is performed by a freeware subroutine named “LMFnlsq”, which is available through Matlab file exchange central [84]. Use of the subroutine was required because the built-in solvers in Matlab are unable to solve complex implicit equations. LMFnlsq was primarily developed for curve fitting using minimization of a sum of squares method by Levenberg-Maquardt algorithm. The code was later adapted by the coder to solve the roots of implicit complex equation, and author adapted the subroutine to solve equation (40). The solution requires inputting initial values to subroutine. At first, the real valued shear velocity of the substrate was used as the initial value for the first run; and solution obtained from this first run was fed to next calculation as the initial value. The method worked for the majority of the range, but for the values of z smaller than 0.2, solutions of x corresponding to velocities higher than shear velocity of the substrate was obtained. This is not physically possible for SAWs so to overcome the problem in this range, another subroutine was developed to

form an initial value matrix, later to be fed into subroutine. The method and code is similar to perturbation solutions, which forms a matrix with real valued initial guesses. The solution to guided wave dispersion parameter x is obtained with the codes for non-dimensional thickness z in steps of 0.002. The x values, then are converted back to phase velocity using the formula for each z as:

$$v = \frac{v_g}{\sqrt{1 - \left(\frac{xv_g}{2\pi z v_g^\infty} \right)^2}} \quad (41)$$

The result obtained is the first Love wave mode and the solutions to higher modes can be obtained with modifications to subroutine, which is discussed in detail at the reference [79].

3.3.2. Fluid Loaded (Four Layer) System

Similarly, the numerical solution of the fluid loaded dispersion curve is also required for fluid loaded perturbation relations presented in the next chapter. Again note that, the dispersion equation is represented by the 8x8 matrix on the upper left corner of matrix in equation (29) or equation (28) itself. Similarly, the mass perturbing layer is neutralized by setting the d_m to 0 and the system containing the substrate, guiding layer and fluid is solved. After algebraic manipulation, the dispersion equation for the system can be obtained, with terms related with mass layer placed at one side of the equation as given in [79] and verified by the author as:

$$\left[\tan(T_g d_g) - \xi_{sg} \tanh(T_s d_s) \right] + \xi_{fg} \tan(T_f d_f) \left[1 + \xi_{sg} \tan(T_g d_g) \tanh(T_s d_s) \right] = \tan(T_m d_m) \left\{ \begin{array}{l} \tan(T_f d_f) \xi_{fm} \left[\tan(T_g d_g) - \xi_{sg} \tanh(T_s d_s) \right] - \\ \xi_{mg} \left[1 + \xi_{sg} \tan(T_g d_g) \tanh(T_s d_s) \right] \end{array} \right\} \quad (42)$$

where any ξ_{ij} value is defined as (except when substrate s is involved with $G \rightarrow \mu$):

$$\xi_{ij} = \frac{G_i T_i}{G_j T_j} \quad (43)$$

Note that the dispersion equation is the left side equation being equal to zero, when $d_m=0$. The equation (42), with left side being equal to zero, is needed to be numerically solved, in order to obtain the dispersion curves. This equation, which requires defining an extra term, in addition to x and β defined for the previous case is more complex than the previous one. Defining $\gamma = \omega d_g (1/v_f^2 - 1/v_g^2)^{1/2}$, with left side of equation (42) being equal to zero, dispersion equation can be rewritten using the defined parameters; formed by the author as:

$$\tan x - \left(\frac{\mu_s}{G_g} \right) \sqrt{\left[\left(\frac{\beta}{x} \right)^2 - 1 \right]} \tanh \left(\frac{d_s}{d_g} \sqrt{\beta^2 - x^2} \right) + \left(\frac{G_f}{\mu_g} \right) \sqrt{\left[\left(\frac{\gamma}{x} \right)^2 + 1 \right]} \tan \left(\frac{d_f}{d_g} \sqrt{\gamma^2 + x^2} \right) \cdot \left[1 + \left(\frac{\mu_s G_f}{G_g \mu_g} \right) \sqrt{\left[\left(\frac{\beta}{x} \right)^2 - 1 \right]} \left[\left(\frac{\gamma}{x} \right)^2 + 1 \right] \right] \tan x \tanh \left(\frac{d_s}{d_g} \sqrt{\beta^2 - x^2} \right) \tan \left(\frac{d_f}{d_g} \sqrt{\gamma^2 + x^2} \right) \right] = 0 \quad (44)$$

The solution for x can be handled similarly for each z , and phase velocity corresponding to z values can be calculated using equation (44).

3.4. Parametric Study

In this section, a parametric study on dispersion analysis of typical substrates and guiding layers and liquid types using the numerical solution method is presented. The effects of material selection, operating frequency, degree of viscoelasticity are investigated as a function of guiding layer thickness. Dispersion curves represent the real part of the phase velocities. The imaginary parts of the phase velocities are related with attenuation and insertion loss, which will not be considered in this study.

3.4.1. Dispersion Solutions of Substrate and Guiding Layer

The parametric study for the dispersion of substrate and guiding layer is aimed to investigate the effect of material selection, operating frequency, degree of viscoelasticity. The dispersion relation can easily be obtained using equation (39) and using the numerical procedure outlined in 3.3.1. As mentioned in previous sections, the dispersion curves will also be used to determine sensitivity by using perturbation relations.

Selection of materials was based on the literature survey given in Table 1. The substrate materials chosen for study are the most typical SH supporting substrates: ST-cut quartz (ST-Quartz), 41° YX lithium Niobate (41°LiNbO_3) and 36° YX lithium tantalate (36°LiTaO_3). Similarly a wide range of guiding layers investigating including silicon

dioxide (SiO₂), metals (chromium-Cr and Gold-Au), and polymers (Parylene-C and SU-8). The material properties required for the study are the shear velocity and density for each material. The properties used for substrate and guiding layer materials are listed in Table 2. Densities (ρ) of all the materials are found in literature, however not all the shear velocities are available. For the ones those missing shear velocities, the values are calculated using the shear modulus and density. Shear modulus (G) can be calculated using Young's modulus (E) and Poisson's ratio (ν) as: $G=E/[2(1+ \nu)]$. The shear velocities are then calculated using the formula $v_s=(G/\rho)^{1/2}$.

Table 2. Material properties for parametric study.

	E (GPa)	ν	G (GPa)	ρ (kg/m ³)	V_s (m/s)
Substrate					
ST-Quartz	-	-	-	2650 [85]	4990 [85]
41°LiNbO ₃	-	-	-	4650 [12]	4795 [2]
36°LiTaO ₃	-	-	-	7460 [85]	4211 [85]
Guiding Layer					
SiO ₂	70 [86]	0.17 [86]	30	2160 [86]	3359
Chromium	279 [4]	0.21 [4]	110	7194 [4]	3936
Gold	78 [4]	0.44 [4]	27	19320 [4]	1192
SU-8	4 [87]	0.22 [87]	1.2	1190 [87]	1012
Parylene-C	4 [88]	0.4 [89]	1.4	1289 [88]	1052
Protein Film			10^{-3} - 10^{-4} [78]	1000 [78]	32

- Non-dimensional general dispersion relation: the first graph showing the numerical results of the dispersion relation is illustrated in Figure 9. In this figure, the data shown is for ST-Quartz substrate with Parylene-C guiding layer and relaxation time $\omega\tau$ is taken as 10^6 (solid limit). The y-axis is the phase velocity and the x-axis is the nondimensional guiding layer (Parylene-C) thickness z , defined previously as $z=d_g f/v_g^\infty$, where d_g is the thickness, f is the frequency and v_g^∞ is the shear velocity in guiding layer. As depicted easily from the figure, the phase velocity remains almost constant (very close to shear velocity of quartz ≈ 5000 m/s) almost up to a z of 0.2. After this point there is a gradual fall is observed with phase velocity approaching shear velocity of guiding layer as expected. Note that for an operating frequency of 100 MHz, the thickness corresponding to $z=1$ for Parylene-C is $10.5 \mu\text{m}$.

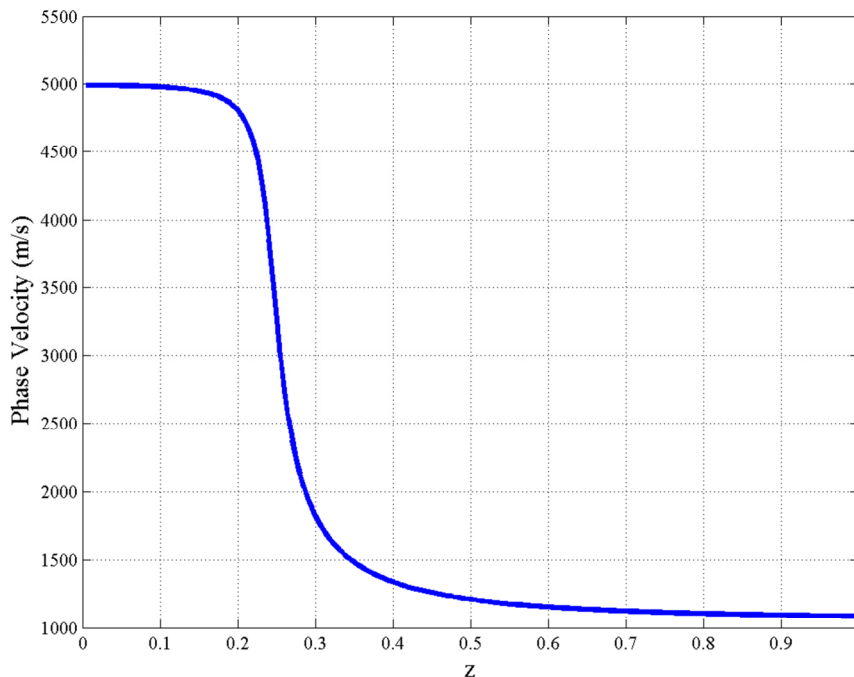


Figure 9. Dispersion curve with substrate: ST-Quartz, guiding layer: Parylene-C, frequency:100 MHz, $\omega\tau = 10^6$ x-axis: z .

- Operation frequency: In this figure the effect of frequency on dispersion curve is presented. The data shown is for ST-Quartz substrate with Parylene-C guiding layer and relaxation time $\omega\tau$ is taken as 10^6 (solid limit). The y-axis is the phase velocity and the x-axis is guiding layer (Parylene-C) thickness. As seen from the figure, the dispersion curves for frequencies 10, 100 and 1000 MHz show similar characteristics. The phase velocity remains constant up to a thickness, corresponding to z values 0.2, which is expected from the previous figure. The x-axis is presented in logarithmic scale for better understanding.

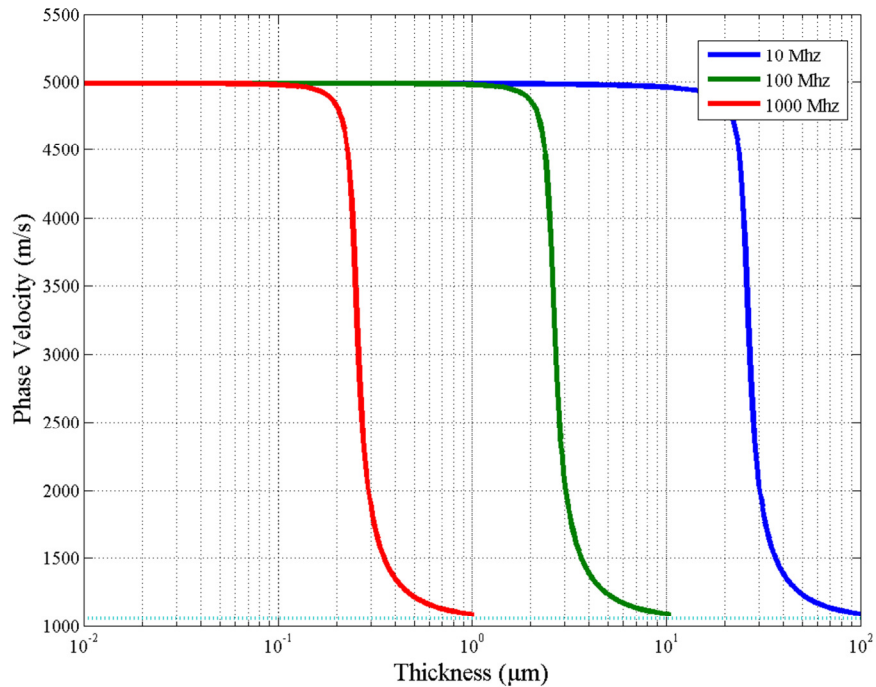


Figure 10. Dispersion curve with substrate: ST-Quartz, guiding layer: Parylene-C, frequency:10, 100 and 1000 MHz, $\omega\tau = 10^6$ x-axis: guiding layer thickness.

- Relaxation time: In Figure 11, the effect of relaxation time $\omega\tau$, or viscoelasticity of the guiding layer; on dispersion curve is presented. The data shown is for ST-Quartz substrate with Parylene-C guiding layer, frequency is 100 MHz and relaxation time $\omega\tau$ is

taken as 10 (liquid) and 10^6 (solid). The y-axis is the phase velocity and the x-axis is guiding layer (Parylene-C) thickness. As seen from the figure, the dispersion curves for two relaxation times are almost exactly the same, except for minor difference in the transition region, corresponding to a range of 0.2 to 0.3 z. The relaxation times for 10 MHz and 1000 MHz was also investigated and similar characteristics were observed. Thus, the results for different frequencies are not illustrated in separate figures.

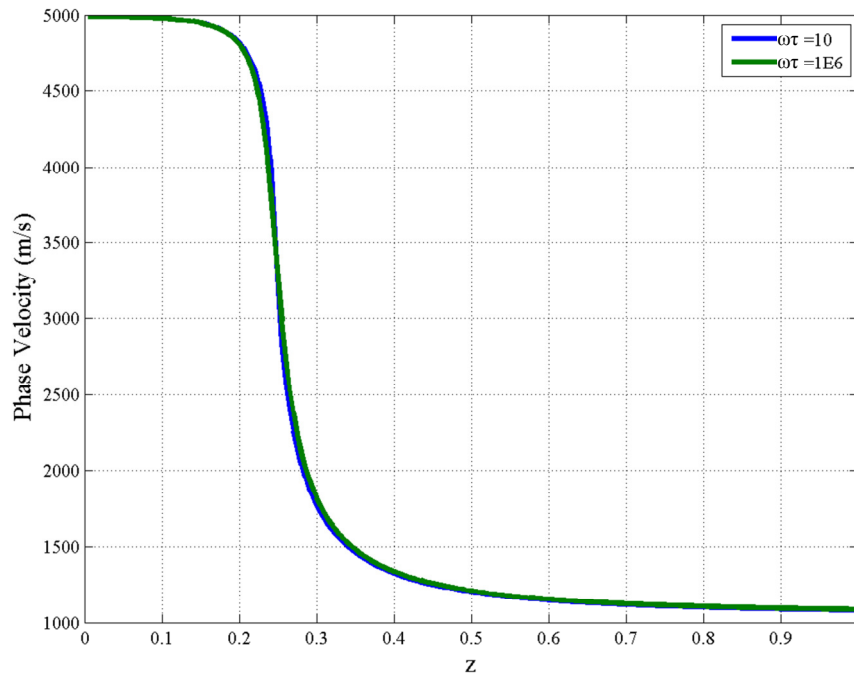


Figure 11. Dispersion curve with substrate: ST-Quartz, guiding layer: Parylene-C, frequency: 100 MHz, $\omega\tau = 10$ and 10^6 , x-axis: dimensionless guiding layer thickness.

- Substrate material: Figure 12 shows the dispersion of three different substrate materials of interest, with same guiding layer. The presented data is for ST-Quartz, 41°LiNbO_3 and 36°LiTaO_3 substrates with Parylene-C guiding layer, with a frequency of 100 MHz, and relaxation time is taken as 10^6 . The x-axis is normalized guiding layer (Parylene-C) thickness. As seen from the figure, the only parts of the dispersion curve

affected are the regions up to $0.25z$. The dispersion curves start with values very close to shear velocities of substrate materials up to $0.25z$ and gradually decreases similarly to the shear velocity in guiding layer. Note that, the graphs were drawn using same z . The IDT periodicity required for same frequency operation on these substrates are different (shear velocities are different). For operation at same frequency, the gradual decrease in phase velocity happens in same region.

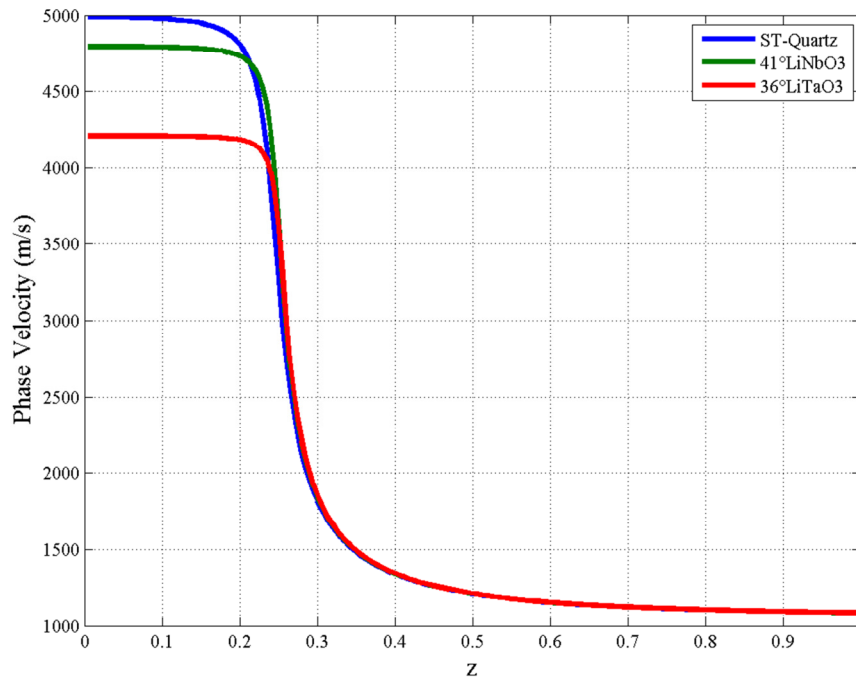


Figure 12. Dispersion curve for substrate: ST-Quartz, 41°LiNbO_3 and 36°LiTaO_3 , guiding layer: Parylene-C, frequency: 100 MHz, $\omega\tau=10^6$, x-axis: dimensionless guiding layer thickness.

- Guiding layer material: Final figure (Figure 13) illustrates the dispersion of five different guiding layer materials of interest, listed in Table 2. The dispersion curves for guiding layers with substrate materials ST-Quartz and 36°LiTaO_3 are illustrated below. Dispersion with 41°LiNbO_3 is not depicted, because 41°LiNbO_3 has intermediate values

of density and shear velocity compared with other two alternatives. ST-Quartz and 36°LiTaO_3 represent the limiting conditions. The guiding layers of SiO_2 , chromium. Gold, SU-8 and Parylene-C, with two substrate materials at a frequency of 100 MHz, and relaxation time of 10^6 are given in Figures (15)(16. The x-axes are the actual guiding layer thickness, unlike normalized thickness z is used in previous figures. The use of z avoided, because each guiding layer has different shear velocities.

The data series in Figure 13 is slightly different from the values presented in previous figures. First of all, for gold, phase velocities with SU-8 and Parylene-C layers, which have lower shear velocities, are calculates up to $5z$; in able to be comply with SiO_2 and chromium layers. The center of gradual decrease, still correspond to $0.25z$ for SU-8 and Parylene-C layers. However, gold differs from the two polymers; with almost no constant phase velocity region in lower z values (or thickness) and almost constant slope in the transition region. This is related with extremely high density of gold compared with polymers (almost 15 times). The dispersion of SiO_2 and chromium is different from the others. They both have higher individual shear velocities and moderate densities (higher than polymers, lower than gold). They both have a lower slope and smoother transition, again with the phase velocity approaching shear velocity of guiding layer with increasing thickness. In next figure, same guiding layers with lithium tantalate are presented.

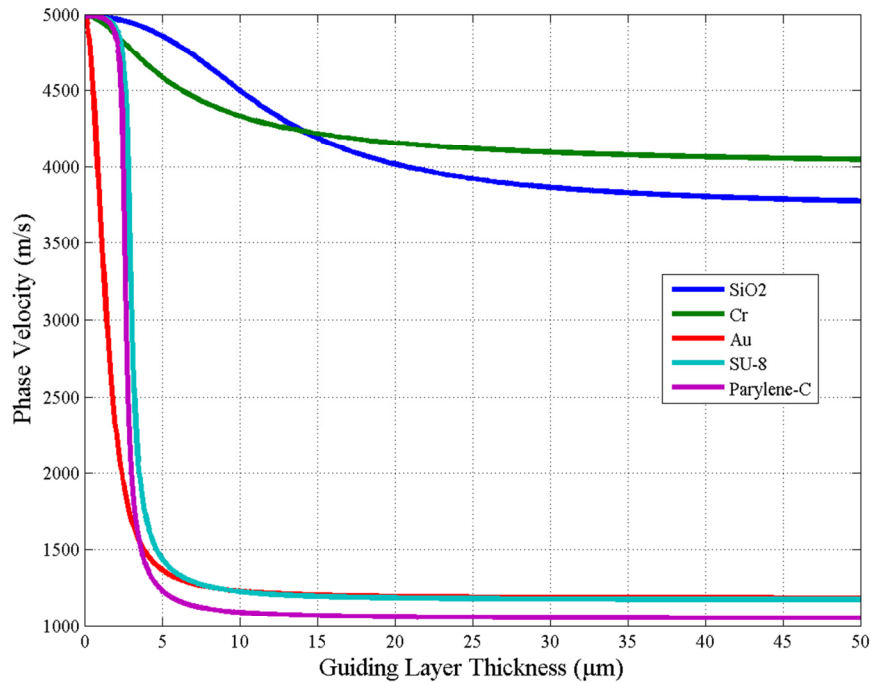


Figure 13. Dispersion curve for substrate: ST-Quartz, guiding layer: SiO₂, chromium, gold, SU-8 and Parylene-C, frequency: 100 MHz, $\omega\tau=10^6$, x-axis: guiding layer thickness.

The results presented in Figure 14 are similar to Figure 13, with some minor differences. For gold, SU-8 and Parylene-C layers, there is no significant change in trends. Their shear velocities are still significantly lower than substrate layer. The densities of polymers SU-8 and Parylene-C are also significantly lower than lithium tantalate, so they remained the same. However, for the gold, as the density of lithium tantalate is much closer to gold than quartz, the transition region has slightly increasing slope this time. SiO₂ and chromium dispersion curves are similar to ones with quartz substrate, again with some differences. First of all, both of their individual shear velocities are closer to lithium tantalate, then of quartz resulting in even smoother transition regions. They still have lower slopes, while the phase velocity approaching

shear velocity of guiding layer with increasing thickness. The most interesting outcome of the figure is the dispersion of chromium, which is almost a straight line in the range. This is because both the density and shear velocity of chromium is very close to of lithium tantalate.

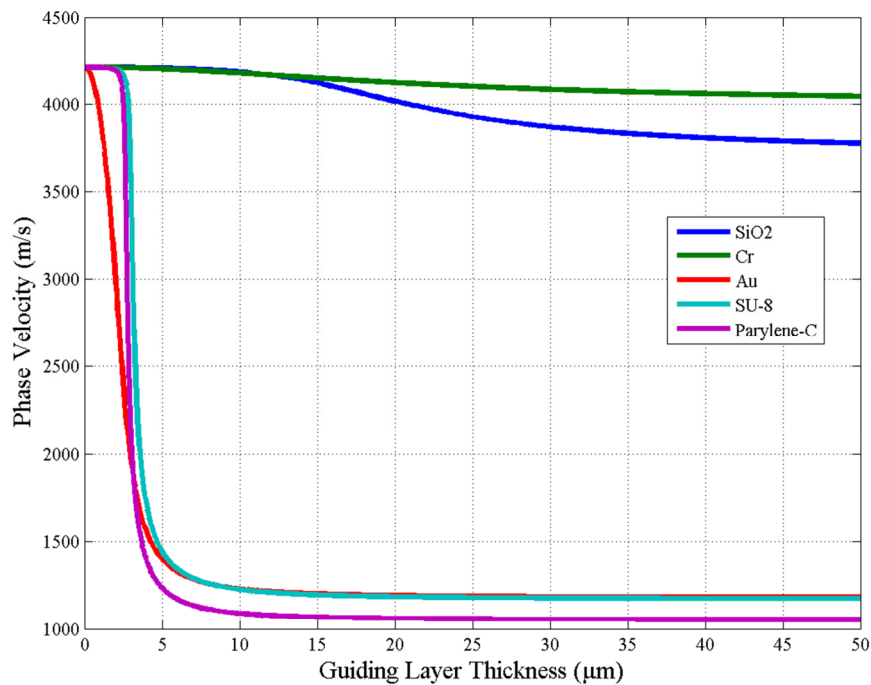


Figure 14. Dispersion curve for substrate: 36°LiTaO_3 , guiding layer: SiO₂, chromium, gold, SU-8 and Parylene-C, frequency: 100 MHz, $\omega\tau=10^6$, x-axis: guiding layer thickness.

Investigating these two limiting substrate materials, we can observe that; a transition region with a gradual decrease in phase velocity exists, where there is a relatively large shear velocity difference between substrate and guiding layer. As the shear velocity of guiding layer gets close to shear velocity of substrate material, smoother transition is observed. An interesting outcome is also observed for density. Large density

differences between substrate and guiding layer results in an almost constant slope transition region. Minimal density difference, does not result in a sharp transition, however results in constant slope transition throughout the range similarly.

3.5. Model Verification

The verification of the analytical model was done experimentally with a set of experiments done for dispersion curve. The relationship between guiding layer thickness and phase velocity of the guided waves were investigated on two-port delay path devices. Two different types of wafers: ST-Cut Quartz and 41°LiNbO_3 were used with two similar IDT designs with different pitches: 300 (number of IDT pairs: $N=20$) and $80\ \mu\text{m}$ ($N=50$).

However, none of the guiding layer materials used in the parametric study was found feasible in the desired thickness range or not accessible. For metals, the thickness required was not found as feasible because of the frequency of devices used. Thus, verification is done using photoresist polymers Shipley S1813 (Shipley, Marlborough, MA, USA), and AZP4260 (AZ Electronic Materials, Branchburg, NJ, USA), because of the thickness requirements. Thickness requirements were determined using non-dimensional thickness z and guiding layer properties. $80\ \mu\text{m}$ pitch sensors were spin coated with S1813 and $300\ \mu\text{m}$ sensors with AZP4620. The material properties for S1813 is given in reference [90] with Young's Modulus of 8 GPa and density of $1200\ \text{kg/m}^3$. The shear velocity for the photoresist was calculated as 1600 m/s with an assumed Poisson's ratio around 0.3. However, to author's knowledge, there is no source for AZP4620's mechanical properties. Both photoresists are based on the same NOVALAC

polymer, thus it was assumed that AZP4260 has the same characteristics as S1813. The photoresists were spin coated with respect to given thickness information and sheets. The spinning speed were chosen as 3000 rpm for S1813 (resulting in 1.6 μm thickness [91]) and 4000 rpm for AZP4260 (resulting in 7 μm thickness [92]). The photoresist layers were spun on top of each other, after softbaking with 60 s (S1813) and 85 s (AZP4260). The soft-bake time successively lengthened by 60 s for S1813) and 85 s for AZP4260 after each spinning. The layers stacked until the response at the monitored frequency vanished. 3 layers were spun for ST-quartz and 4 layers were spun for 41°LiNbO_3 . The results were presented in Figure 15Figure 18, for all 4 cases. However, the data points did not fit to dispersion curves perfectly. The method for data-fit suggested in [81] is employed to modify the dispersion curve. In the reference, authors stated that, using an effective density of 2.6 times the actual density of the guiding layer was essential to fit the dispersion curve to the data points. In Figure 5 of [81], it is seen that this approach were able to fit the dispersion of PMMA guiding layer with LiTaO_3 substrate to experimental data points. Following that fashion, the properties of the guiding layers were changed to fit the data points, and the velocity and density used to fit the data were listed below the figures, and also summarized in Table 3.

Table 3. Effective shear velocity and density values used for data fit. (Original values: $V_g=1600$ m/s and $\rho_g= 1200$ kg/m³)

Substrate	Pitch	$V_{g,eff}$ (m/s)	$\rho_{g,eff}$ (kg/m ³)
ST-Quartz	300 μm	1600	3200
	80 μm	3200	1200
41°LiNbO_3	300 μm	1600	5000
	80 μm	3200	2200

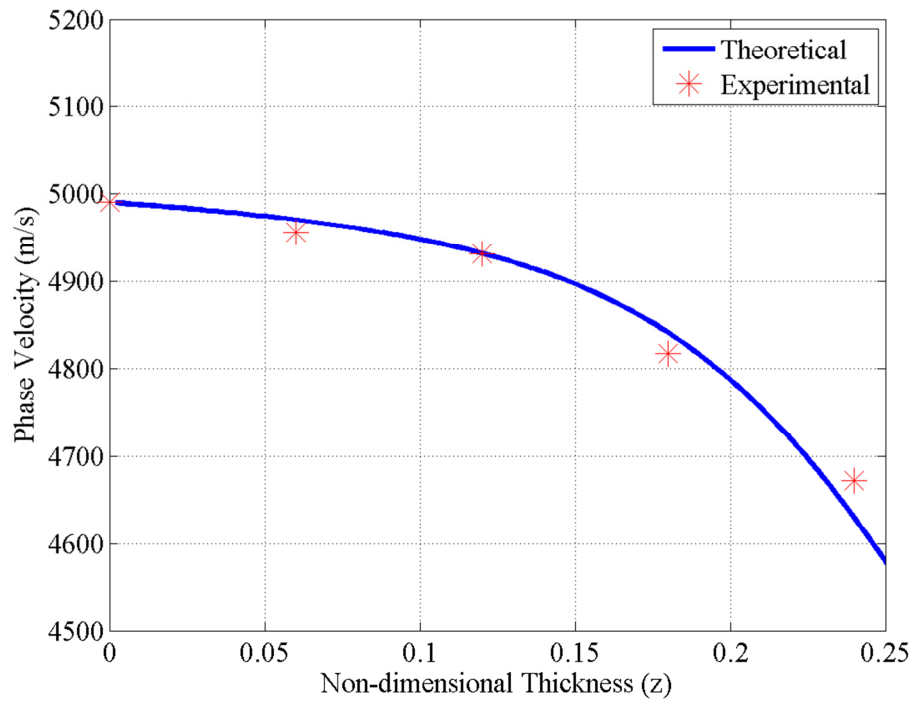


Figure 15. Data points and curve fit for substrate: quartz, $\lambda:80 \mu\text{m}$, guiding layer: S1813 ($V_{g,eff}=3200 \text{ m/s}$, $\rho_{g,eff}=1200 \text{ kg/m}^3$)

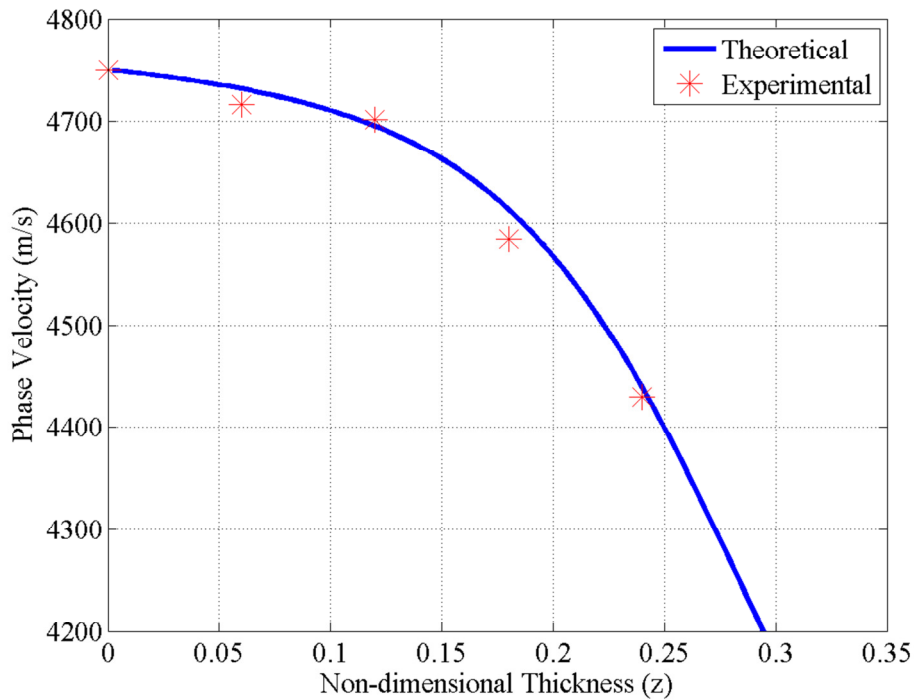


Figure 16. Data points and curve fit for substrate: LiNbO3, $\lambda:80 \mu\text{m}$, guiding layer: S1813 ($V_{g,eff}=3200 \text{ m/s}$, $\rho_{g,eff}=2200 \text{ kg/m}^3$)

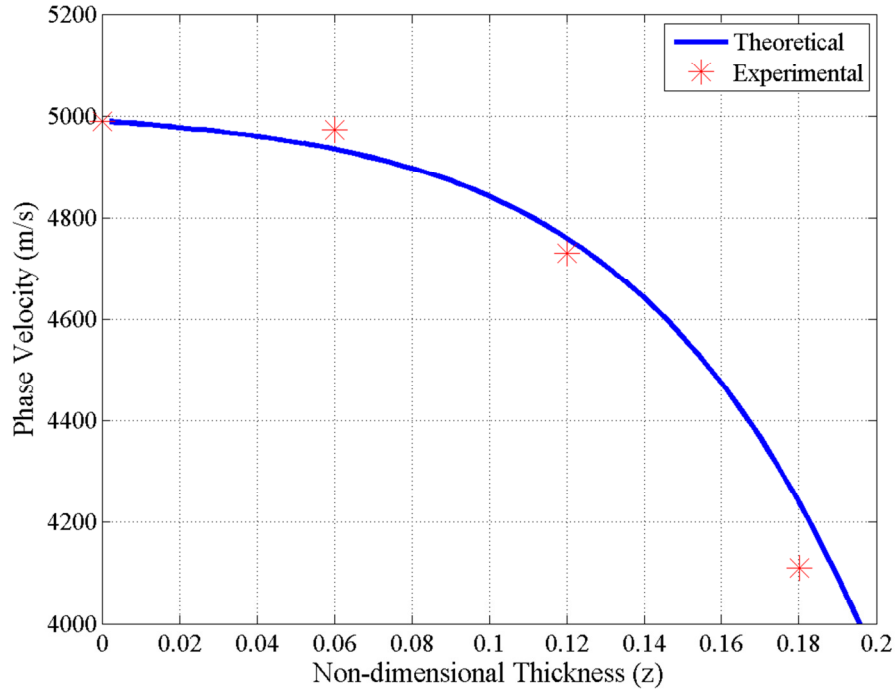


Figure 17. Data points and curve fit for substrate: quartz, λ : 300 μm , guiding layer: AZP4620 ($V_{g,eff}=1600$ m/s, $\rho_{g,eff}=3200$ kg/m³)

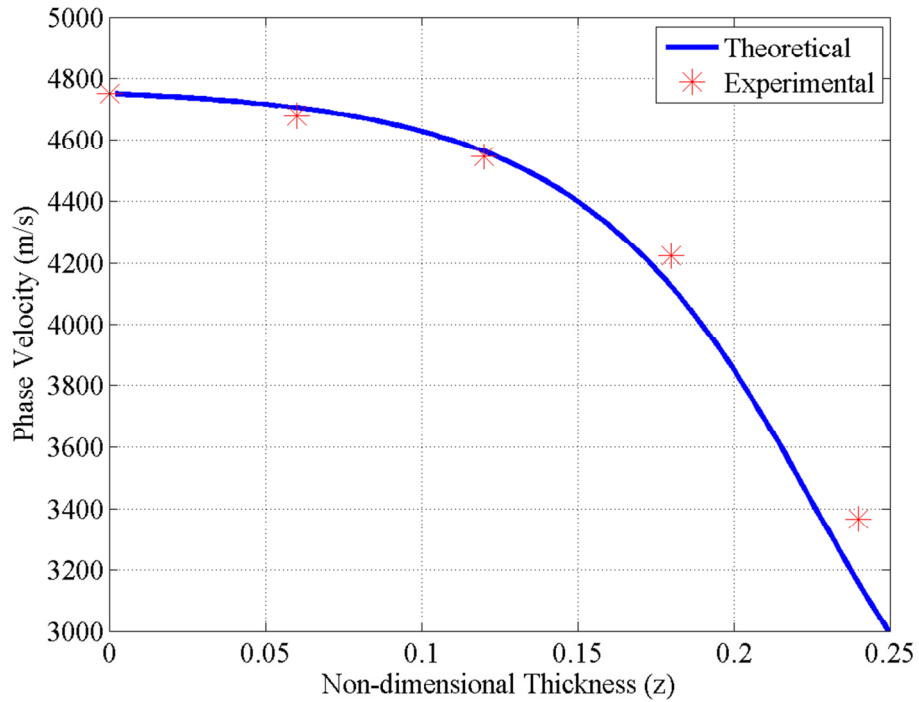


Figure 18. Data points and curve fit for substrate: LiNbO₃, λ : 300 μm , guiding layer: AZP4620 ($V_{g,eff}=1600$ m/s, $\rho_{g,eff}=5000$ kg/m³)

As depicted from Table 3, use of effective density, similar to [81], was required to fit the dispersion curve to the data points for 300 μm pitch sensors with AZP4620. However, for 80 μm pitch sensors, both doubling the shear velocity and increasing the density was required for 41°LiNbO_3 and only doubling the velocity was enough for quartz. There's no clear trend however, it can be observed that the effective velocities used were the same for the same pitch sensors. Furthermore, the ratio of effective densities between 300 μm and 80 μm is similar (≈ 2.5) for each substrate individually.

CHAPTER 4. PERTURBATION ANALYSIS

4.1. Perturbation Theory

Perturbation theory for acoustic waveguide problems was first presented by Auld [9]. Perturbation methods are analytical approximation techniques to provide guidelines for computations using numerical methods, and also for problems in which direct computation is not feasible [9]. Perturbation methods are based on the assumption that there are small changes in the solution, caused by small changes, or perturbations. Several different perturbation equations can be derived for a system with different parameters and degrees of approximation (order of expansion). Even though nowadays processing computational tasks is not a problem, the approximations still enable rapid analysis of a system, which can give detailed insight to problems.

Auld derived the perturbations from the complex reciprocity equation presented in the same reference [9]. The complex reciprocity equation given in equation (45) below was derived to relate two different possible solutions to a system, form the basis of derivation. In this equation, v is velocity, T is stress, Φ is potential difference, D is charge density, ρ is density, s_E is strain under constant electric field, d is piezoelectric strain constants, ϵ is dielectric coefficient, and F is force. The equation relates two possible solutions (1 and 2) to the set of partial differential ‘field’ equations and related constitutive relations of coupled acoustic and electromagnetic system. The details of the

derivation of the complex reciprocity equation is beyond scope of this dissertation, and can be found in reference [9]. The derivation involves forming two possible trial solutions to the system; multiplying equations with certain terms and adding/subtracting them to form one reciprocity equation. Similarly second reciprocity equation is obtained by interchanging subscripts of the solution with enabling the two solutions have different frequencies. If the terms by which the equations are multiplied are real, the resulting equations are called real reciprocity relation, and if they're complex (with their conjugates), resulting equations are called complex reciprocity relation:

$$\begin{aligned}
& \nabla \cdot \left\{ -v_2^* T_1 - v_1 T_2^* + \Phi_2^* \frac{\partial D_1}{\partial t} + \Phi_1 \frac{\partial D_2^*}{\partial t} \right\} = \\
& - \frac{\partial}{\partial t} \left(\begin{bmatrix} -v_2^* T_2^* - \nabla \Phi_2^* \\ 0 \\ 0 \end{bmatrix} \begin{bmatrix} \rho & 0 & 0 \\ : s :^E & : d \\ . d : & \epsilon :^T \end{bmatrix} \begin{bmatrix} v_1 \\ T_1 \\ -\nabla \Phi_1 \end{bmatrix} \right) + \\
& (v_2^* F_1 + v_1 F_2^*) + \Phi_2^* \frac{\partial D_1}{\partial t} + \Phi_1 \frac{\partial D_2^*}{\partial t}
\end{aligned} \tag{45}$$

Assuming no sources are present; the effect of piezoelectricity is negligible (as in previous section); no electrical perturbations; and both solutions 1 and 2 vary with $e^{j\omega t}$ the equation (45) reduces to:

$$\nabla \cdot \{ -v_2^* T_1 - v_1 T_2^* \} = 0 \tag{46}$$

A sample perturbation formula derivation is presented below, as described in reference [9]. Consider a single layer system with a mechanical surface perturbation only on top surface ($y=0$) as presented in Figure 19.

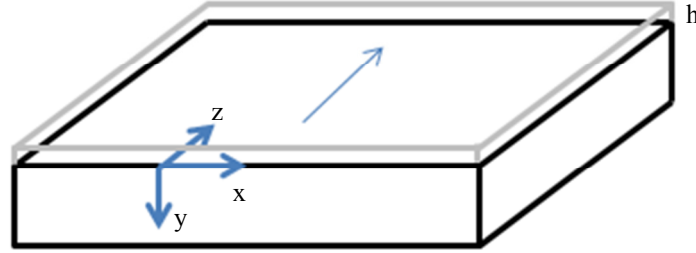


Figure 19. Single layer perturbation model

Assume the acoustic field is independent of x , which results in divergence in equation (46) only contain y and z derivatives. The integration of equation (46) along the y axis; from 0 to b , would result in energy per unit x , considering a field independent of x :

$$\int_0^b \frac{\partial}{\partial z} \left\{ -v_2^* T_1 - v_1 T_2^* \right\} \cdot \hat{z} dy = \left\{ -v_2^* T_1 - v_1 T_2^* \right\} \cdot \hat{y} \Big|_0^b \quad (47)$$

Assume the solutions 1 and 2 correspond to perturbed and unperturbed solutions respectively, where β_n is real (lossless) and β_n' is complex as:

$$v_1 = e^{-j\beta_n' z} v_n'(y), v_2 = e^{-j\beta_n z} v_n(y) \quad (48)$$

Substituting the perturbed and unperturbed solutions in to equation (47) and reorganizing the terms, with a first order approximation of β_n as $\beta_n' = \beta_n + \Delta\beta_n$;

$$\Delta\beta_n = \frac{-j \{ -v_n^* T_n' - v_n' T_n^* \} \hat{y}|_0^b}{\int_0^b \frac{\partial}{\partial z} \{ -v_n^* T_n' - v_n' T_n^* \} \cdot \hat{z} dy} \quad (49)$$

In able to derive the formula assume that, the perturbations are small, the two terms in the denominator can be replaced with unperturbed values and with stress free boundary condition dictates the second T term in the numerator is zero, the perturbation formula for this system with perturbation only at top surface can be obtained as :

$$\Delta\beta_n = \frac{j(\{ -v_n^* T_n' \} \cdot \hat{y})_{y=0}}{2 \int_0^b \frac{\partial}{\partial z} \{ -v_n^* T_n' \} \cdot \hat{z} dy} \quad (50)$$

The expression with the integral in the denominator usually treated as a measure that defines average unperturbed power flow per unit length; and is a constant three dimensional vector for each material. The values of this vector for several materials are given in reference [9]. The equation (50) can, for example, be used to treat mechanical surface perturbation of Rayleigh wave problem, as given in example 1 of Chapter 12 of reference [9]. Several perturbation relations was derived, solved, compared with exact solutions, and presented in the reference. The results presented show that perturbation theory is very useful in prediction of change in phase velocity, showing similar trends to exact solution. The agreement between exact and perturbation solutions usually increase with higher order approximations.

The perturbation relations for phase velocity changes will be formed step by step in the next section without energy integration and one-dimensional propagation

assumption. Starting from the simplest case, perturbations caused by the guiding layer g on the bare substrate, to perturbation by mass layer under liquid loading will be developed. Linear perturbation equations are formed with the assumptions made with first order approximations, except for the first case. The first case of perturbation by guiding layer on substrate is only presented to show the derivation of the equations. The exact solution to model formed is already calculated numerically in previous chapter.

4.2. Perturbation by Guiding Layer

The simplest case is the system with the substrate and guiding layer only, with no mass layer. The dispersion equation for this case was obtained previously as:

$$\tan(T_g d_g) = \xi_{sg} \tanh(T_s d_s) \quad (39)$$

The solution of equation (39) is the exact solution to the system. In order to obtain the perturbation relations, consider a perturbed state, in which the phase velocity is v_0 , which is different from v_s , Assuming the guiding layer g is viscoelastic ($\mu_g \rightarrow G_g$), the perturbation relation for changes in phase velocity (Δv) can be obtained by first order expansions of wave vectors: $T_s^0 \rightarrow T_s^0 + \Delta T_s$, $T_g^0 \rightarrow T_g^0 + \Delta T_g$ and $\xi_{sg}^0 \rightarrow \xi_{sg}^0 + \Delta \xi_{sg}$ with expansions of terms:

$$\tanh(T_s d_s) = \left[\frac{(\tanh(T_s^0 d_s) + \tanh(\Delta T_s d_s))}{1 - (\tanh(T_s^0 d_s) \tanh(\Delta T_s d_s))} \right] \quad (51)$$

$$\tan(T_g d_g) = \left[\frac{(\tan(T_g^0 d_g) + \tan(\Delta T_g d_g))}{1 - \tan(T_g^0 d_g) \tan(\Delta T_g d_g)} \right] \quad (52)$$

To develop an expression in change in phase velocity Δv , with $v=v_0+\Delta v$; combining equations (39), (51) and (52):

$$\left[\frac{(\tan(T_g^0 d_g) + \tan(\Delta T_g d_g))}{1 - \tan(T_g^0 d_g) \tan(\Delta T_g d_g)} \right] = (\xi_{sg}^0 + \Delta \xi_{sg}) \left[\frac{(\tanh(T_s^0 d_s) + \tanh(\Delta T_s d_s))}{1 - (\tanh(T_s^0 d_s) \tanh(\Delta T_s d_s))} \right] \quad (53)$$

As discussed in reference [79], the solution is possible when $\xi_{sg}^0 = 0$, which implies $T_s^0 = 0$ and $\Delta T_g = 0$, because of the assumption that no perturbation present on guiding layer for very small changes. Hence, equation (53) simplifies to:

$$\tan(T_g^0 d_g) \approx \Delta \xi_{sg} \tanh(\Delta T_s d_s) \quad (54)$$

Substituting and rearranging terms, the change in phase velocity Δv can be calculated from the relation:

$$\left(\frac{\Delta v}{v_s}\right) \tanh^2\left(\frac{d_s \omega}{v_s} \sqrt{-\frac{2\Delta v}{v_s}}\right) \approx -\frac{1}{2} \left(\frac{G_g T_g^0 v_s}{\mu_s \omega}\right)^2 \tan^2(T_g^0 d_g) \quad (55)$$

This expression can further be simplified under some assumptions. Firstly, in the case of infinitely thick substrate, in which $d_s \omega \rightarrow \infty$, and negative real part of Δv , "tanh ()" term on the left side of the equation approaches to unity. Similarly, if we consider elastic solid and Newtonian fluid limits of G_g ($\omega \tau \rightarrow \infty$ and 0 respectively), further simplifications can be made.

4.3. Perturbation by Mass Layer

Perturbation relations for the three layer system can be derived in a similar fashion. The perturbation equations are aimed to investigate change in phase velocity as a function of perturbing mass layer thickness. Before expanding the terms related with the perturbing mass layer, reorganizing equation (21), in a form to have mass layer terms on the left side:

$$\xi_{mg} \tan(T_m d_m) = \frac{\xi_{sg} \tanh(T_s d_s) - \tan(T_g d_g)}{1 + \xi_{sg} \tan(T_g d_g) \tanh(T_s d_s)} \quad (56)$$

Assuming viscoelastic guiding and mass layers, we can expand ξ_{mg} and $\tan(T_m d_m)$ similarly around v_0 , and the perturbation relation for three layer case as given in [79]:

$$\frac{\Delta v}{v_0} \approx g(\omega, v_0, v_s, G_g, v_g, d_s, d_g) \left(1 - \frac{v_m^2}{v_0^2}\right) \left(\frac{\tan(T_m^0 d_m)}{T_m^0 d_m}\right) d_m \rho_m \quad (57)$$

where the coefficient factor g is:

$$g = \frac{\frac{-\omega^2}{G_g T_g^0} [1 + \tan^2(T_g^0 d_g)]}{\left\{ \frac{T_g^0 d_g}{\frac{v_0^2}{v_g^2} - 1} [1 + \tan^2(T_g^0 d_g)] + \frac{\xi_{sg}^0 T_s^0 d_s}{1 - \frac{v_0^2}{v_s^2}} \left[1 - \tanh^2(T_s^0 d_s) + \tan(T_g^0 d_g) \left(\frac{1}{\frac{v_0^2}{v_g^2} - 1} + \frac{1}{1 - \frac{v_0^2}{v_s^2}} \right) \right] \right\}} \quad (58)$$

Note that, in equations (57) and (58); phase velocity of the substrate is real and of guiding and mass layers are complex. As seen from equation (58), the coefficient factor g has numerous terms, even for the three layer system. It is quite obvious that it will not be easy to come up with a similar analytical expression, if an additional layer is added. However, the perturbation relation (57) can be used to evaluate g approximately with the method presented in reference [82]. Assume that the guiding layer and the mass perturbing layer are of same material. Furthermore, let the perturbing mass layer be acoustically thin ($\omega d_m \rightarrow 0$), which results in $\tan(T_m^0 d_m) / T_m^0 d_m \rightarrow 1$. If we assume an infinitesimal phase velocity change $\Delta v \rightarrow dv$ happens with an infinitesimal increase in mass layer thickness, and $d_m \rightarrow dx$, equation (57) can be rewritten as

$$g(\omega, v_0, \mu_s, v_s, G_g, v_g, d_s, d_g) = \left(\frac{dv}{dx} \right)_{x_3=d_m} \left[v_0 \rho_g \left(1 - \frac{v_g^2}{v_0^2} \right) \right]^{-1} \quad (59)$$

If we consider a very small perturbation from the initial unperturbed state, we can take the limit of the expression in equation (59) to obtain a value for g at any point with reorganizing terms:

$$\lim_{d_m \rightarrow 0} g(\omega, v_0, v_s, G_g, v_g, d_s, d_g) = \lim_{d_m \rightarrow 0} \frac{1}{v_0} \left(\frac{dv}{dx} \right)_{x_3=d_m} \left[\rho_g \left(1 - \frac{v_g^2}{v_0^2} \right) \right]^{-1} \quad (60)$$

$$g(\omega, v_0, v_s, G_g, v_g, d_s, d_g) = \left(\frac{d \ln v}{dx} \right)_{x_3=d_m} \left[\rho_g \left(1 - \frac{v_g^2}{v_0^2} \right) \right]^{-1}$$

where $d(\ln v)/dx$ is the slope of the natural logarithm of the dispersion curve. Substituting equation (60) back in equation (57), we can obtain assuming acoustically thin perturbing layer:

$$\frac{\Delta v}{v_0} = \left(\frac{d \ln v}{dx} \right)_{x_3=d_m} \frac{\left(1 - \frac{v_m^2}{v_0^2} \right) \rho_m d_m}{\left(1 - \frac{v_g^2}{v_0^2} \right) \rho_g} \quad (61)$$

The equation can further be modified to replace x with a dimensionless parameter z , which is defined as; $z = d_g f / v_g^\infty$ where, the superscript ∞ represents the solid limit of velocity. Substituting this dimensionless parameter into the equation (61), we can obtain:

$$\frac{\Delta v}{v_0} = \left(\frac{d \ln v}{dz} \right)_{z=z_0} \frac{\left(1 - \frac{v_m^2}{v_0^2} \right)}{\left(1 - \frac{v_g^2}{v_0^2} \right)} \frac{f}{v_g^\infty \rho_g} \rho_m d_m \quad (62)$$

The perturbation relation, equation (62) shows that, the complex coefficient equation g can be obtained from the dispersion curve; resulting in a simple expression. Having obtained the dispersion curve from equation (39) numerically, the slope of the natural logarithm of the dispersion curve for each operating point can be calculated numerically using a center-difference method. The sensitivity to mass loading at any z , can then be formed as suggested in [79] as:

$$S_m^{vacuum} = \lim_{d_m \rightarrow 0} \frac{1}{\rho_m d_m} \left(\frac{dv}{dx} \right)_{x_3=d_m} \operatorname{Re} \left(\frac{\Delta v}{v_0} \right)^{vac} \\ = \operatorname{Re} \left[\left(\frac{d \ln v}{dz} \right)_{z=z_0}^{vac} \frac{\left(1 - \frac{v_m^2}{v_0^2} \right)}{\left(1 - \frac{v_g^2}{v_0^2} \right)} \frac{f}{\rho_g v_g^\infty} \right] \quad (63)$$

The superscript “*vac*” is used for this case, in order to avoid confusion with fluid loaded case. The perturbation equations developed are used to investigate mass loaded sensor and biosensor performance, similar to parametric study presented in previous section. The sensitivity defined in equation (63), which depends on the dispersion curve, guiding and perturbing mass layer properties is used. Note that the sensitivity definition was made by dividing the velocity change by the density and thickness of the mass

guiding layer. Thus, the sensitivity is calculated per surface density ($1/\text{kg/m}^2$), which makes the results independent of thickness or density of the mass perturbing layer. Only its mass or surface density is considered. It should again be noted that, the sensitivities that will be shown in the next figures are only valid for small perturbations. The sensitivity value corresponding to a thickness is only valid around that thickness, with acoustically thin mass perturbing layers. The figures are all drawn with non-dimensional thickness z , which was defined as $z = f \cdot d_g / v_g^\infty$. The sensitivity values on the y axes of the figures do represent physical significant quantities. The defined sensitivity equation is based on the ratio $\Delta v/v$, which is also equal to $\Delta f/f$. More physically significant values can be obtained for sensitivity if the sensitivity values are divided by some reference velocity or frequency. However, for easy comparison the values are left without further manipulation of the results of equation (63).

- Mass loading sensitivity with ST-quartz substrate with chromium guiding layer: In Figure 20, the sensitivity of ST-quartz substrate with chromium guiding layer is shown for four different perturbing mass layers, as a function of non-dimensional thickness of chromium. The sensitivity of this configuration to Parylene-C, gold, SiO₂ and chromium is illustrated. The dispersion curve shown in Figure 13 and material properties (shear velocity) of the guiding layers, given in Table 2 are used. The highest sensitivity among the mass perturbations is observed for Parylene-C and gold. This high sensitivity is caused by the sharp phase velocity transitions observed from the dispersion curve. As depicted previously, less the shear velocity difference between substrate and guiding layer, less sharp is the transition; resulting in less sensitivity.

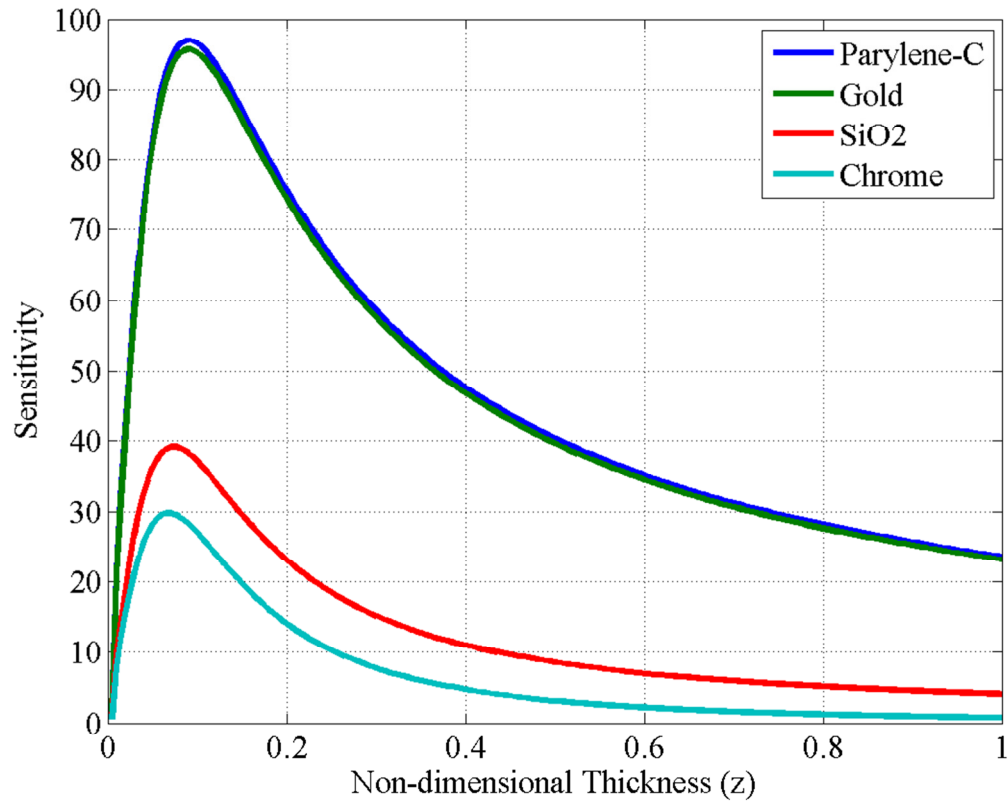


Figure 20. Sensitivity with substrate: quartz; guiding layer: chrome; $f=100$ MHz; $\omega\tau=10^6$ with perturbing mass layers: Parylene-C, gold, SiO₂ and chromium.

- Mass loading sensitivity with LiTaO₃ substrate with chromium guiding layer: Similarly Figure 21 illustrates the sensitivity with chromium guiding layer is shown for four different perturbing mass layers, but with LiTaO₃ substrate. The dispersion curve of chromium from Figure 14 is used to calculate the sensitivities. Compared with ST-quartz, there are no sharp peaks. The sensitivity is also lower than ST-quartz; however the range of peak sensitivity is wider than ST-Quartz. Similarly, the highest sensitivity among the mass perturbations is observed for Parylene-C and gold. Lower sensitivity values; again, is related with the dispersion curve of LiTaO₃ and chromium case. The lower shear velocity difference between substrate and guiding layer results in lower sensitivity.

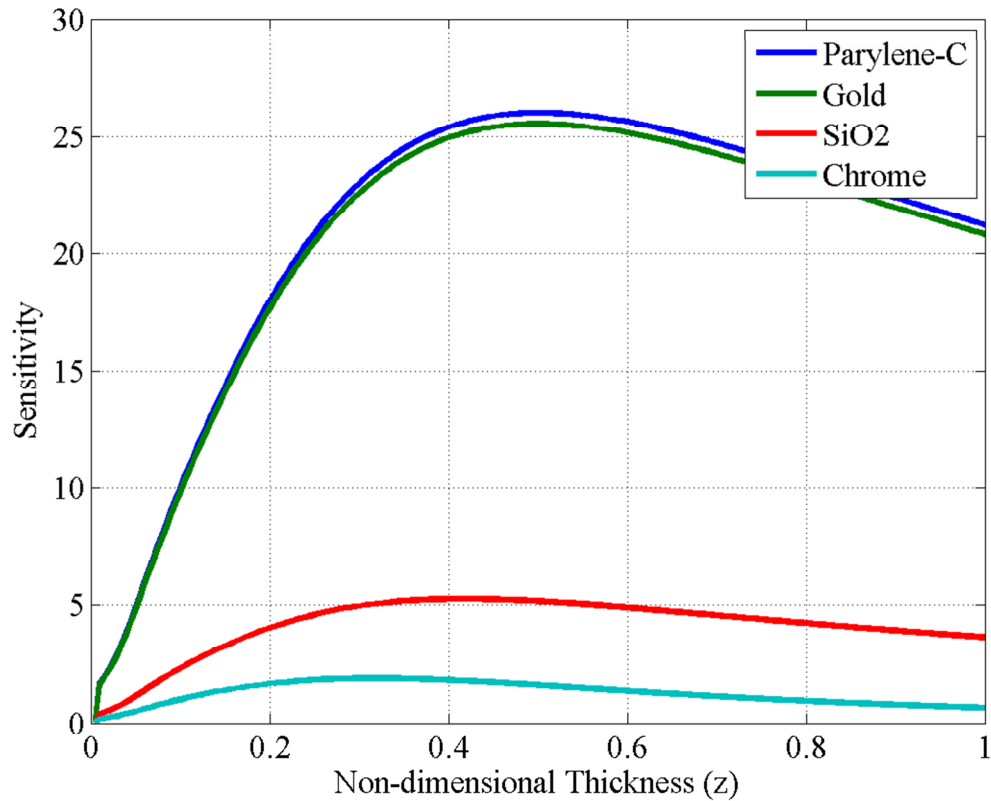


Figure 21. Sensitivity with substrate: LiTaO₃; guiding layer: chrome; $f=100$ MHz; $\omega\tau=10^6$ with perturbing mass layers: Parylene-C, gold, SiO₂, and chromium.

- Mass loading sensitivity with ST-quartz substrate with gold guiding layer: The next figure show the effect of changing guiding layer on the sensitivity for same perturbing mass layers used in Figure 20. The results in Figure 22 show higher sensitivities for all four guiding layers. Especially for SiO₂ and chromium, the sensitivity values are very high, with their shear velocities higher than of gold. There are also local peaks for very small z values observed for these two perturbing layers, caused by the curvature change of dispersion curve, given in Figure 13. However, the high sensitivity related with these two layers might not be physically sound. Love wave theory and the model presented are based on the assumption that the shear velocity of topping layer

should be less than the bottom layer. The sensitivity for gold and Parylene-C is also almost three times higher than the chromium guiding layer case. Similar to chromium case, the peaks are pronounced.

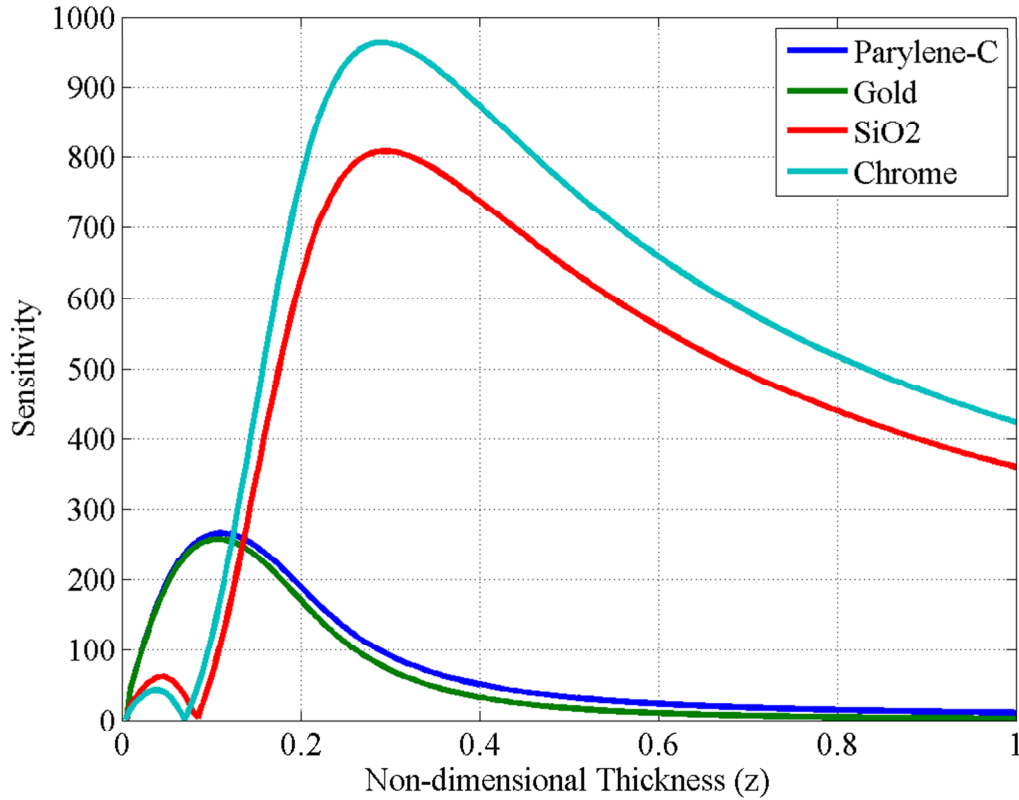


Figure 22. Sensitivity with substrate: quartz; guiding layer: gold; $f=100$ MHz; $\omega\tau=10^6$ with perturbing mass layers: Parylene-C, gold, SiO₂ and chromium.

- Mass loading sensitivity with LiTaO₃ substrate with gold guiding layer: In Figure 23, the same configuration with LiTaO₃ substrate and guiding layer is shown. The sensitivity results are very similar to ones given in Figure 22 with higher sensitivities for all four guiding layers. Especially for SiO₂ and chromium, the sensitivity values are very high, with no significant physical soundness. The local peaks for very small z values which are observed in quartz substrate have almost diminished for these two perturbing

layers. For LiTaO_3 , the sensitivity for gold and Parylene-C is also almost ten times higher than the chromium guiding layer case (with compared to three times in quartz). Similar to chromium case, the peaks are pronounced.

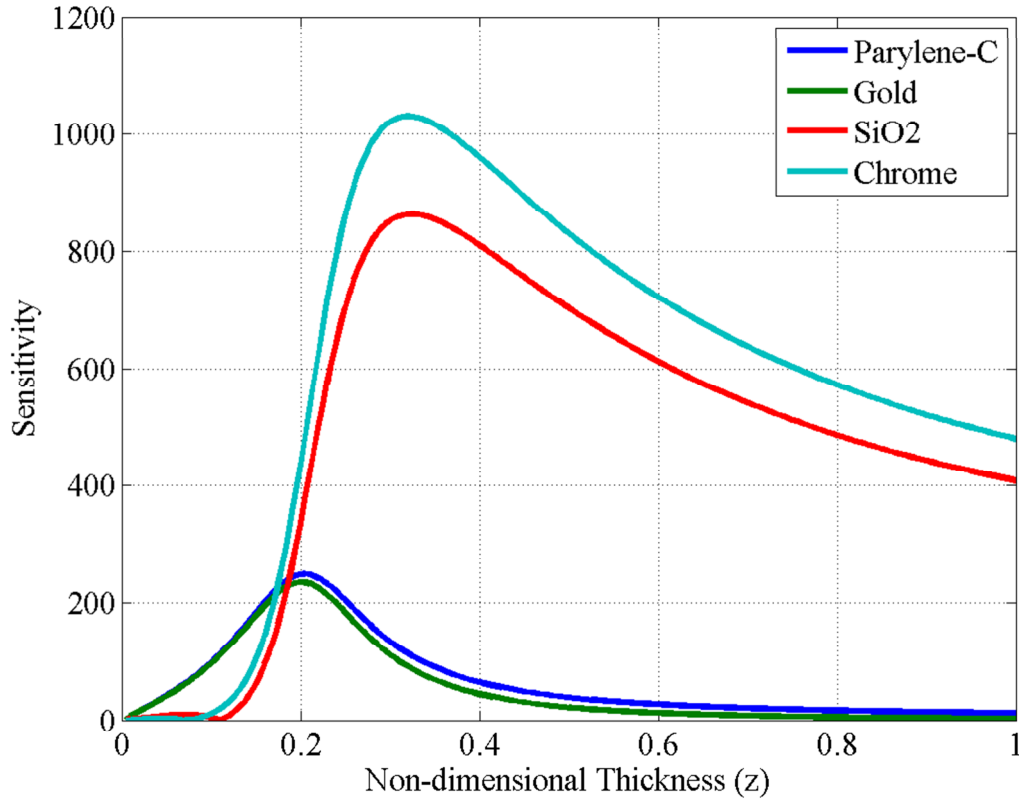


Figure 23. Sensitivity with substrate: LiTaO_3 ; guiding layer: gold; $f=100$ MHz; $\omega\tau = 10^6$ with perturbing mass layers: Parylene-C, gold, SiO_2 and chromium.

- Mass loading sensitivity with ST-quartz substrate with Parylene-C guiding layer: Figure 24 illustrates the same configuration, this time with Parylene-C. The trends are similar to gold guiding layer, however, the sensitivities are further enhanced; almost 25 folds for SiO_2 and chromium, and 40 folds for gold and Parylene-C; compared with gold guiding layer. The shape of the curve is similar to gold perturbing layer for chrome and SiO_2 , however the peaks for gold and Parylene-C are more pronounced. The sharper

peaks are a result of change of the curvature (change of sign of second derivative) of the Parylene-C dispersion curve in Figure 13. The dispersion curve of the gold on top of quartz has a transition region with almost constant slope resulting in wider sensitivity region. The change of curvature in Parylene-C or (SU-8) results in the sharper peak. Sharper peaks are usually not desirable for general sensing application, because realization of experimental optimization, for small changes, is not easy. Even the surface uniformity or roughness can affect the optimal performance. The local peaks at low z values are also less pronounced in Parylene-C guiding layer, compared with gold.

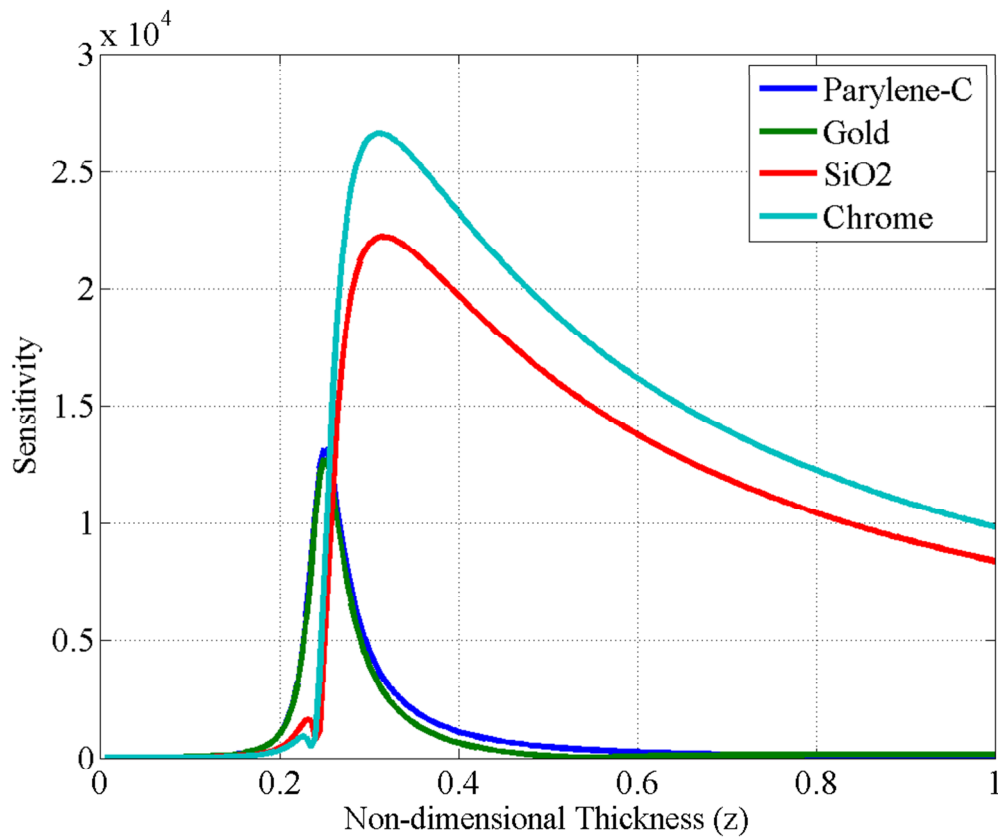


Figure 24. Sensitivity with substrate: quartz; guiding layer: Parylene-C; $f=100$ MHz; $\omega\tau=10^6$ with perturbing mass layers: Parylene-C, gold, SiO₂ and chromium.

- Mass loading sensitivity with LiTaO₃ substrate with Parylene-C guiding layer:

Figure 25 shows the sensitivity to same layers with Parylene-C guiding layer on LiTaO₃ substrate. The trends are very similar to quartz with Parylene-C, both shape- and value-wise. The sensitivities are further enhanced almost 25 folds for SiO₂ and chromium similar to quartz but for gold and Parylene-C the increase is higher: 50 folds. It can be concluded that for Parylene-C guiding layer, the substrate selection does not make significant difference in sensitivity, with sharp peaks for sensing gold and Parylene-C.

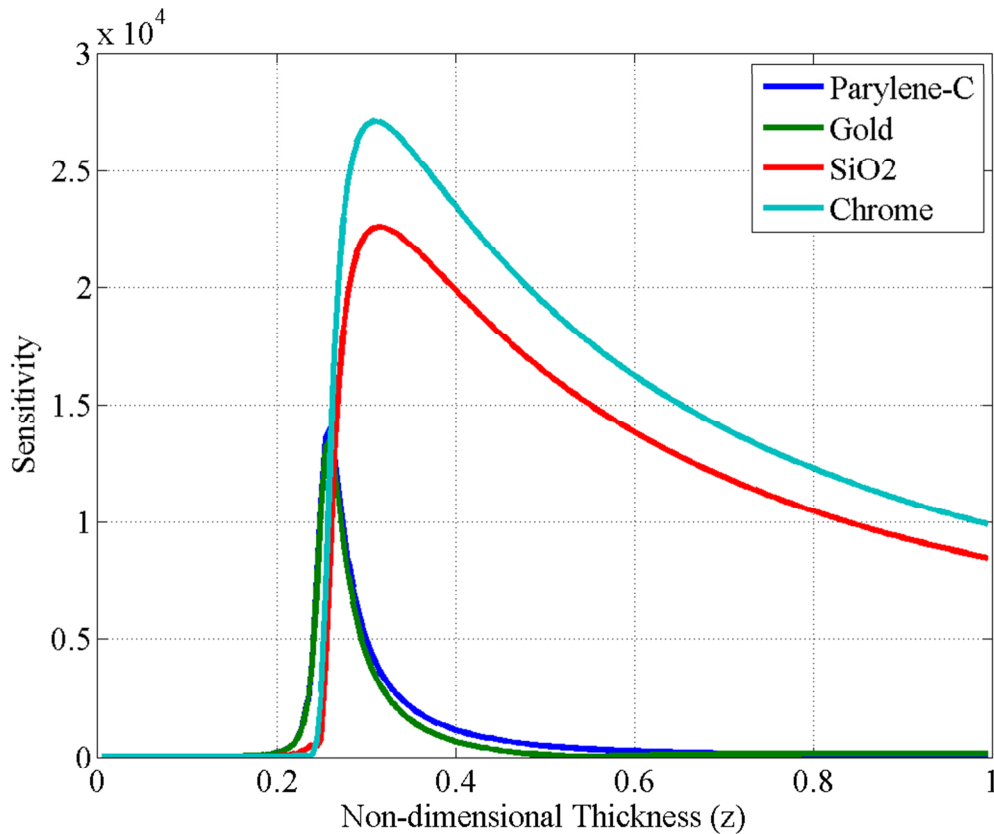


Figure 25. Sensitivity with substrate: LiTaO₃ guiding layer: Parylene-C; $f=100$ MHz; $\omega\tau=10^6$ with perturbing mass layers: Parylene-C, gold, SiO₂ and chromium.

- Mass loading sensitivity with quartz substrate with viscoelastic Parylene-C guiding layer: Figure 26 shows the sensitivity with Parylene-C guiding layer (with viscoelastic behavior) and antibody layer on quartz substrate. Similar to the parametric study done before, the limiting relaxation times of 10 and 10^6 used for Parylene C. For protein film, the values listed in reference [78] was used. Note that for each relaxation time of Parylene-C; the two dispersion curves given in Figure 11 is used. A small increase in sensitivity is observed, when the guiding layer is more fluid-like (smaller relaxation time), however the values are close and have almost the same shape. The protein film, which is assumed to have almost viscous behavior (using the values for real and imaginary modulus in the reference), show sensitivity in between those two. The high sensitivity values obtained for biosensing are obtained under several assumptions, which may make this sensitivity hard to achieve. First of all, antibody films have the highest level of non-homogeneity. The isotropic film assumption makes this high sensitivity values hard to achieve for actual protein films. The sensitivity to same perturbations on LiTaO_3 substrate is not presented, because they show very similar results with very little increase in sensitivity.

The sensitivity study showed that the highest possible sensitivity can be obtained using polymer guiding layers. The highest sensitivity values are observed in Figure 26 with Parylene-C guiding layer on top of ST-cut quartz substrates. Furthermore, it was observed that the sensitivity to protein layers in this configuration is very similar to sensitivity to viscoelastic Parylene layers. However, as mentioned, the optimization for the narrow range might be problematic, especially when there is no precise control of polymer thickness. On the other hand, if sensitivity in a wide range is desired, solid films

with higher shear velocities are favorable, with less sensitivity. Fabrication capability and film properties such as intrinsic stress should also be considered, if the desired film thicknesses are high. For low frequency applications, the high thickness requirement for solid films might even be impossible.

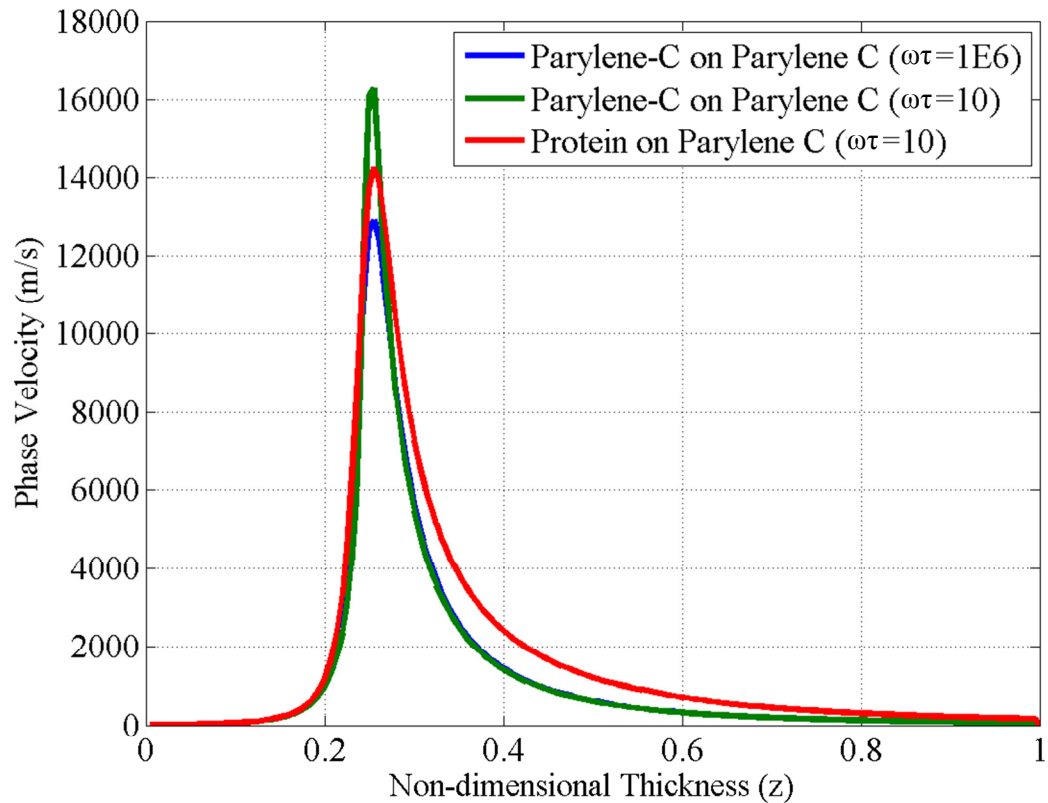


Figure 26. Sensitivity with substrate: quartz guiding layer: Parylene-C; $f=100$ MHz; $\omega\tau=10$ and 10^6 with perturbing mass layers: Parylene-C, and protein layer.

The final sensitivity perturbation investigations were performed on the experimental parameter modifications presented in section 3.5. The effect was investigated using four cases: actual density and shear velocity; double density and actual velocity; actual density and double velocity; and double density and double velocity.

The configuration selected was Parylene-C guiding layer on top of ST-quartz substrate and perturbation sensitivity to Parylene-C for the elastic case. The dispersion curves for these four cases are presented in Figure 27 and related sensitivities are presented in Figure 28. As expected from previous investigations, increase in density and shear velocity both results in decrease in sensitivity. The effect of doubling the velocity is more significant as observed for the cases of perturbations to silicon dioxide and chromium, which both have higher shear velocities. The modifications reduce the sensitivity; however the sensitivity is still higher than previous cases.

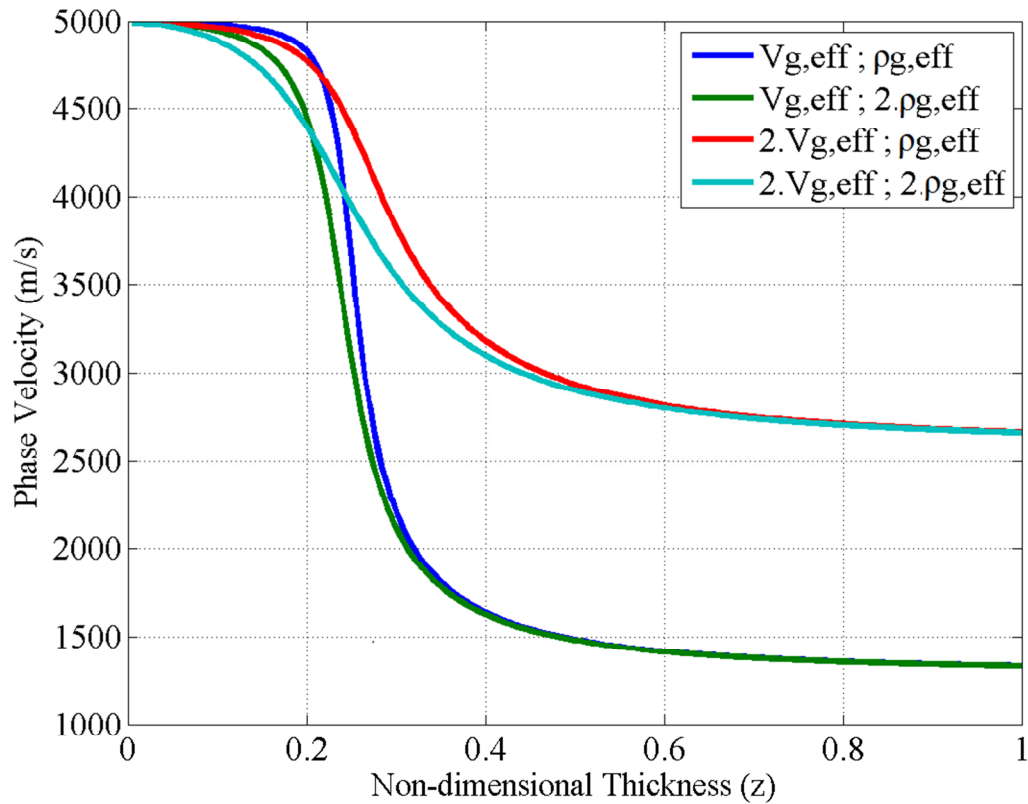


Figure 27. Disperison curves with modified density and shear velocity, after experimental verification.

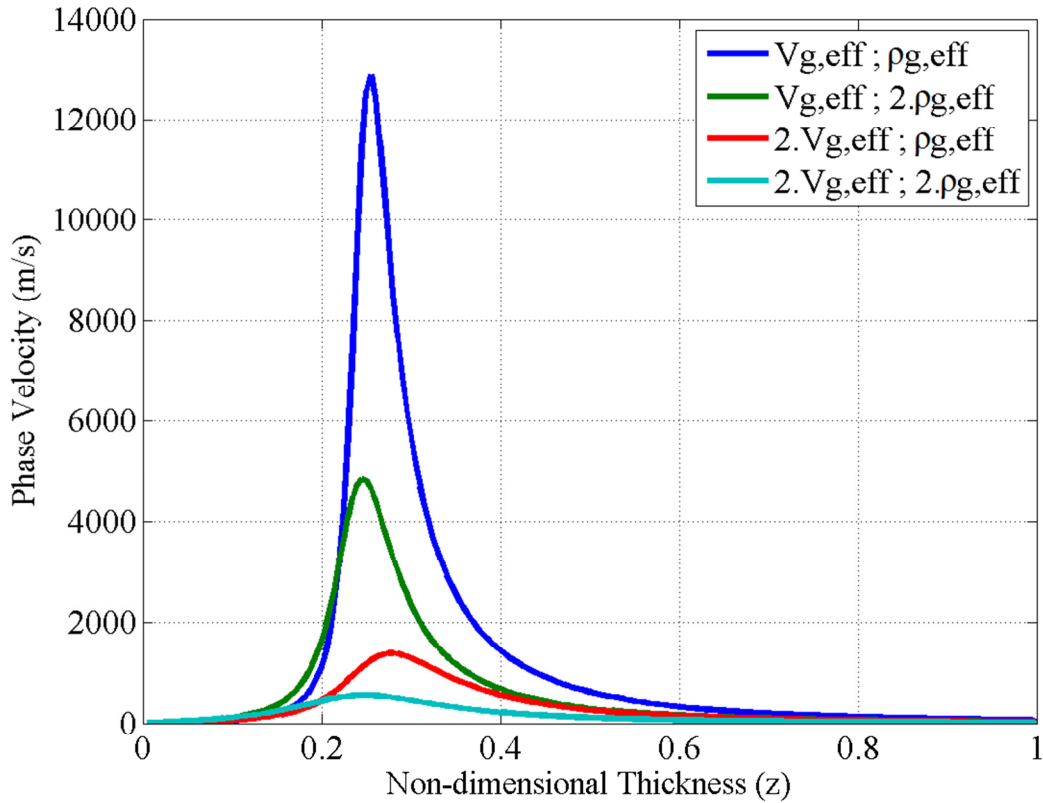


Figure 28. Sensitivity curves with modified density and shear velocity, after experimental verification.

4.4. Perturbation by Fluid Loaded Mass Layer

As discussed previously, biosensing applications usually involve sensing target analytes from aqueous solutions or samples. In an ideal SH SAW sensor, wave propagation should not be affected by liquid loading, however properties of the liquid like viscosity and conductivity topping the sensor, affects its performance. The effects of the liquid on top of the guiding and mass layer with perturbing mass layer under liquid loading can be investigated similarly. The perturbation relation is formed using the dispersion relation (42), again with order expansions. Additionally, $\tan(T_f d_f)$ term can be

expanded similar to equation (51) and ξ_{ij} terms can be expanded as $\xi_{ij} \rightarrow \xi_{ij}^0 + \Delta\xi_{ij}$. The algebraic solution procedure and expressions is lengthy and not presented. The resulting perturbation relation for the 4 layer case is given in reference [79] in the form of equation (57) and (58) as

$$\frac{\Delta v}{v_0} \approx g_L(\omega, v_0, \mu_s, v_s, G_g, v_g, G_f, v_f, d_s, d_g, d_f) \left(1 - \frac{v_m^2}{v_0^2}\right) \left(\frac{\tan(T_m^0 d_m)}{T_m^0 d_m}\right) \cdot \left(1 + \xi_{fm}^2 \tan^2(T_f^0 d_f)\right) d_m \rho_m \quad (64)$$

where g_L is the function that can be related to dispersion curve of the liquid loaded case, to similar to g in equation (60) related to dispersion of three layer case. In order to obtain an expression for g_L , assuming small changes: $\Delta v \rightarrow dv$, and $d_m \rightarrow d$; and guiding layer is same material as mass layer:

$$g_L = v_0 \frac{dv}{dx} \left[\left(1 - \frac{v_g^2}{v_0^2}\right) \left(\frac{\tan(T_m^0 d_m)}{T_m^0 d_m}\right) \left(1 + \xi_{fg}^2 \tan^2(T_f^0 d_f)\right) d_g \rho_g \right]^{-1} \quad (65)$$

Following the procedure from equation (57) to (60), the perturbation relation for the four layer system, g_L becomes:

$$g_L = v_0 \frac{dv}{dx} \left[\left(1 - \frac{v_g^2}{v_0^2}\right) \left(1 + \xi_{fg}^2 \tan^2(T_f^0 d_f)\right) d_g \rho_g \right]^{-1} \quad (66)$$

Converting x to non-dimensional parameter z , taking the limit approaching 0 similarly and resubstituting g_L into equation; the perturbation relation for liquid loaded case is:

$$\frac{\Delta v}{v_0} = \left(\frac{d \ln v}{dz} \right)_{z=z_0}^{fluid} \left[\frac{1 + \xi_{fm}^2 \tan^2 (T_f^0 d_f)}{1 + \xi_{fg}^2 \tan^2 (T_f^0 d_f)} \right] \left(\frac{1 - \frac{v_m^2}{v_0^2}}{\frac{v_g^2}{v_0^2}} \right) \frac{f}{v_g^\infty \rho_g} \rho_m d_m \quad (67)$$

Note that the $d \ln v / dz$ term in this equation, corresponds to the slope of the fluid loaded dispersion curve f , obtained from equation (42). In order to obtain the slopes for cases, the dispersion curve should be evaluated numerically. Similar to previous case, the sensitivity at fluid loaded system, which includes the slope of fluid loaded dispersion curve, can be defined and calculated as:

$$S_m^{fluid} = \lim_{d_m \rightarrow 0} \frac{1}{\rho_m d_m} \left(\frac{dv}{dx} \right)_{x_3=d_m} \operatorname{Re} \left(\frac{\Delta v}{v_0} \right)^{fluid} \\ = \operatorname{Re} \left[\left(\frac{d \ln v}{dz} \right)_{z=z_0}^{fluid} \left[\frac{1 + \xi_{fm}^2 \tan^2 (T_f^0 d_f)}{1 + \xi_{fg}^2 \tan^2 (T_f^0 d_f)} \right] \left(\frac{1 - \frac{v_m^2}{v_0^2}}{\frac{v_g^2}{v_0^2}} \right) \frac{f}{\rho_g v_g^\infty} \right] \quad (68)$$

The solutions of the fluid loaded case were almost identical to dry sensing for the materials chosen with water-like fluids for sensing. Thus the results of the dry sensing can be assumed as valid for fluid loaded sensing as well.

CHAPTER 5. CASE STUDY: BCL-2 SAW IMMUNOSENSOR

Note to Reader

The manuscript and the results presented in this chapter have been previously published [5, 8]; available for open access and are utilized with permission of the publisher.

5.1. Introduction

Ovarian cancer is the fifth leading cause of cancer death among women in United States and it has a 1.4% (1 in 71) lifetime risk [93]. Diagnosis of ovarian cancer in the early stages currently accounts for only 30% of all cases, and the cancer is lethal in most late stages. The lack of overt symptoms and the absence of a reliable screening test results in over 70% diagnoses occurring the disease has spread beyond the ovary, so the prognosis is poor [93]. Ovarian cancer patients have a short median survival time after diagnosis and their 5-year survival rate is less than 40%. Currently, pelvic examination, ultrasound and blood levels of serum biomarker CA125 are the standard screening methods for ovarian cancer [94-96]. However, each of these methods has limitations for ovarian cancer detection. Pelvic examination is known to be obstructed by the intraperitoneal location of the ovaries and is typically capable of late-stage disease

detection only. Similarly, ultrasonic examination does not possess the capability of distinguishing between benign and malignant cases and is subject to variation in interpretations among sonographers. CA125 is the current standard biomarker for ovarian cancer diagnosis and monitoring [96]. It is present in the blood serum of ovarian cancer patients. However, it has been shown that CA125 levels can also be elevated due to other disorders, including inflammation, benign gynecological disease, or hepatic disease, leading to false positive results [97, 98]. There are other biomarkers that have been associated with ovarian cancer such as eosinophil-derived neurotoxin [99], mesothelin [100], VEGF [101], and HE4 [102]. There also exists a few biochips relying on fluorescence or chemiluminescence for ovarian cancer monitoring based on DNA sequences (testing for ovarian cancer-related mutations) [103, 104] and protein biomarkers [105, 106]. However, these biosensors use complex reagents such as DNA extraction kits and expensive laboratory equipment including fluorescence microscopes or plate readers, thus, are not suitable for point-of-care testing [107]. Recently, an enzyme-linked immunosorbent assay (ELISA) test based on a cell-phone-coupled optical sensor has been presented for point-of-care quantification of urinary HE4 levels [107]. However, the chemicals and substances used during ELISA tests are still fairly expensive, and special attention should be given for storage. The absence of reliable screening methods to detect early ovarian cancer contributes to poor prognosis. Therefore, the development of a new, reliable, simple, safe, and economic testing platform to detect ovarian cancer is imperative.

Bcl-2 (B-cell lymphoma 2) is a protein that is directly related with apoptosis of healthy and cancer cells [108]. Apoptosis is the most common form of programmed cell

death (cellular autophagocytosis, anoikis and necrosis are other forms). It has several other crucial functions, such as formation of the embryo, tissue maintenance, cellular homeostasis, terminating immune responses, and restricting the spreading of infections [109]. The Bcl-2 family, named after the Bcl-2 protein itself, includes both anti-apoptic and pro-apoptic constituents that control the release of catalysts of cell death. It was previously shown that urinary Bcl-2 levels are elevated during different stages of ovarian cancer [110, 111]. Clinical validation of urinary Bcl-2 as a reliable biomarker for ovarian cancer was conducted with ELISA tests using urine samples collected from 388 patients, including healthy controls and patients with benign gynecological disorders, early- and late-stage ovarian cancer [110]. The average urinary level of Bcl-2 was found to be 0.59ng/ml in healthy controls, 1.12ng/ml in benign disorders, 2.60ng/ml in early-stage ovarian cancer and 3.58ng/ml in late-stage ovarian cancer. The highest Bcl-2 concentration observed in the study was around 10ng/ml. The number of samples, average concentration, and standard deviation of Bcl-2 for these four patient groups are listed in Table 4. Signs of poor diagnosis of early-stage ovarian cancer can also be observed from the table, considering the small number of early-stage ovarian cancer patients (13) compared to other groups (137+). Thus, analyzing the values in Table 4, the minimum detectable target concentration of Bcl-2 was chosen to be 0.5ng/ml for design and for experimental characterization studies reported herein.

The efficacy of Bcl-2 as a biomarker for ovarian cancer was further validated by comparison to CA125 serum levels using ELISA tests on samples from with results obtained from 12 healthy controls and 23 cancer patients. [110]. Elevated urinary Bcl-2 (>1.8ng/ml) identified 17/17 or 100% of patients with serous adenocarcinoma (versus

13/17 or 76% with CA125), 4/4 or 100% of patients with mucinous ovarian cancer (versus 3/4 or 75% with CA125), and 1/2 or 50% of patients with primary peritoneal cancer as ovarian cancer positive (versus 1/2 or 50% with CA125).

Table 4. Elevated urinary Bcl-2 in cohorts for healthy controls, benign diseases, and early- and late-stage ovarian cancer (N:388) [110].

	Number of Samples	Mean (ng/ml)	Std. Dev. (ng/ml)
Normal	77	0.59	0.61
Benign	161	1.12	0.79
Early-Stage Ovarian Cancer	13	2.60	2.23
Late-Stage Ovarian Cancer	137	3.58	1.55

Furthermore, none of the healthy controls had urinary Bcl-2 levels higher than 1.8ng/ml and were identified as cancer negative (versus 2/12 or 16% incorrect identification with CA125). It was noted that Bcl-2 did considerably better in identifying false positives as compared to CA125 screening, and it was concluded that urinary Bcl-2 over-expression can be effectively employed for ovarian cancer monitoring [110]. The comparison of Bcl-2 and CA125 not only provides further validation of Bcl-2 as a urinary biomarker, but also it leads the way for more reliable dual screening for ovarian cancer diagnosis.

The biosensor studied employs shear horizontal (SH) surface acoustic waves (SAWs) to identify mass loading changes caused by Bcl-2 binding specifically to antibodies on the sensor surface. It is composed of a pair of interdigital transducers (IDTs) microfabricated on ST-cut Quartz wafers in the direction 90° off x-axis and delay path specifically functionalized to capture Bcl-2 proteins while minimizing non-specific

adsorption (Figure 29). An experimentally-verified optimized surface functionalization scheme was employed for effective capture of Bcl-2 protein while maximizing sensitivity and selectivity. The developed surface functionalization technique also minimizes the non-specific binding to the sensor surface. The sensor's electrical connections were made by low-conductivity silver-reinforced epoxy. The experimental characterizations of the sensor's response to varying Bcl-2 concentrations were performed in a custom-designed oscillatory circuit. The oscillatory circuit was composed of two RF amplifiers connected in series, a frequency counter, an oscilloscope (to monitor the signal), and the sensor, which was used as the feedback element determining the oscillation frequency. The characterization was performed by using multiple sensors with up to 10 tests conducted on a sensor by cleaning the delay path with 1.5M NaCl solution in de-ionized (DI) water. The tests were done by placing 80 μ l droplets of Bcl-2 solutions (in Dulbecco's phosphate-buffered saline—DPBS) with various concentrations on the delay path. Quantification of the Bcl-2 concentration was achieved by monitoring the frequency shift for each solution. The frequency shift was caused by the change in surface density of the delay path (mass loading). As surface density increased by protein adhesion, SAW velocity decreased, resulting in a reduction in the oscillation frequency that was measured by the frequency counter. The frequency shift for each tested concentration was measured, and the sensor was successful in detecting Bcl-2 concentrations as low as the target concentration, 0.5ng/ml. It was observed that the frequency shift had a linear trend corresponding to increasing Bcl-2 concentration. Additionally, minimal frequency shift was observed for the control DPBS solution with no Bcl-2 present.

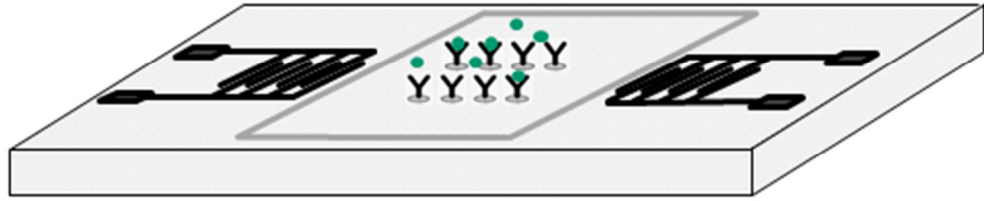


Figure 29. Illustration of sensor.

In the following section, important design parameters, fabrication of the sensor, and surface functionalization are discussed in detail. In section 5.3, the electrical characterization of the sensor and results are presented. The final section covers the discussions and conclusion along with the future work.

5.2. Sensor Design and Fabrication

5.2.1. Sensor Design

The sensor uses shear horizontal surface acoustic waves, which are frequently used for liquid-loaded biosensing applications. In SH-SAWs, the particle displacement is in the plane of the surface (unlike normal-to-surface displacement of Rayleigh waves). SH-SAWs are not affected or damped by liquid loading, as compared to Rayleigh waves, in which the particle displacement is directly coupled with the liquid on top and highly damped by mass loading of the liquid itself. Thus, Rayleigh waves are virtually insensitive to mass loading changes in liquid sensing applications. On the other hand, almost all SH wave propagation on various substrates results in leaky waves (not pure waves like Rayleigh waves), which also leak into longitudinal and shear vertical wave

components when excited. For this reason, special cuts of typical wafer types of wafers are typically used for SH waves, in which the energy is highly concentrated on the SH mode. Typical wafer types used in SH-SAWs are ST cut Quartz, 41° and 36° Y-cut Lithium Niobate (LiNbO_3), and 36° Y-cut Lithium Tantalate (LiTaO_3). The sensing mechanism of SH-SAW sensors relies on the change of SAW speed either by change in mass loading (most biological and chemical sensors) or by changing physical parameters. In general, the majority of SAW sensors include surface treatments and extra layers to effectively and specifically sense the target analyte. Several SH-SAW sensors have been reported using 36° Y-cut LiTaO_3 [112], ST-cut Quartz [37, 113], 36° Y-Cut Quartz [114], 41° Y-cut LiNbO_3 [115, 116], 64° Y-cut LiNbO_3 [30, 117], potassium niobate (KNbO_3) [118], and Langasite [76]. In the design stage, different alternative SH-SAW generating wafers (such as ST-cut Quartz, 36° Y-Cut LiNbO_3 , and LiTaO_3) were tested with identical delay path designs and surface functionalization steps. It was observed that ST-cut Quartz is the most stable and the easiest to operate among those tested. ST-cut Quartz is also favorable for narrower bandwidth operation, and it does not need additional layers or gratings to concentrate the energy in the surface. SH waves are present in the direction of 90° off the x-axis (parallel to primary flat) in ST-cut Quartz, so the features were designed to obtain wave propagation in this particular direction.

The substrates used in this study were 3-inch, single-side-polished, 500 μm -thick ST-cut Quartz wafers. The SH-SAWs were generated and sensed by a pair of interdigital transducers separated with a delay path on these wafers. The pitch (corresponding to the wavelength of the SAW) was chosen as 300 μm , ensuring fabrication yield and tolerable wave attenuation through the delay path. Each finger of the IDT was 75 μm wide

(corresponding to the one quarter of wavelength) for the most efficient SAW generation, as reported by others [10]. The design parameters of the sensor are illustrated in Table 5.

Table 5. Sensor design parameters.

Wavelength (λ)	300 μm
Finger width ($\lambda/4$)	75 μm
Finger length	6250 μm
Number of IDT finger pairs	20
Total sensor size	28mm x 22mm
Delay path length	12mm (40λ)
Resonance frequency	16.8MHz

5.2.2. Fabrication

The IDTs were microfabricated using conventional MEMS fabrication techniques with a single-mask photolithography process. The fabrication steps are illustrated in Figure 30. The fabrication process started with cleaning the wafer in an acetone bath placed in an ultrasound cleaner for 10 minutes, followed by rinsing with methanol and DI water and dried by a stream of nitrogen (Figure 3 [a]). The metal film (Cr) was then sputtered by DC sputtering (CRC Sputter, Torr International, New Windsor, NY) for 5 minutes at 200mA constant current to obtain a film thickness of 1000Å (Figure 3 [b]). After sputtering, the wafers were cleaned once again with acetone, methanol, and DI water and dried with nitrogen. A positive photoresist S1813 (Shipley, Marlborough, MA) was then spun on the wafer. Photoresist was spun initially for 10 seconds at 700 rpm to be spread around the wafer, and then for 40 seconds at 3000 rpm to reach the desired thickness (Figure 3 [c]). A photoresist thickness of 1.6 μm was obtained using this recipe.

The wafers were then soft-baked at 90°C for 60 seconds before exposure. After soft bake, the wafers were exposed to UV light for 5 seconds with an average intensity of 25W/m² to transfer the features from the mask to the wafers (Figure 3 [d]). The exposed wafers were then developed in developer MF-319 (Shipley, Marlborough, MA, USA) for 70 seconds to remove the exposed portions of the photoresist. The wafers were then hard-baked for 5 minutes at 100°C. The features were formed by etching for 40 seconds (Figure 3 [e]). Then, the remaining photoresist was removed in an acetone bath (Figure 3 [f]). After completing the fabrication process to realize the sensors, the wafers were coated with photoresist to protect the features during the dicing process. The dicing of the ST Quartz wafer was performed using resin-bonded diamond blades at a spindle speed of 20K rpm and a feed rate of 1mm/s in the dicing saw. One of the fabricated ST-cut Quartz sensors used in this study is illustrated in Figure 31.

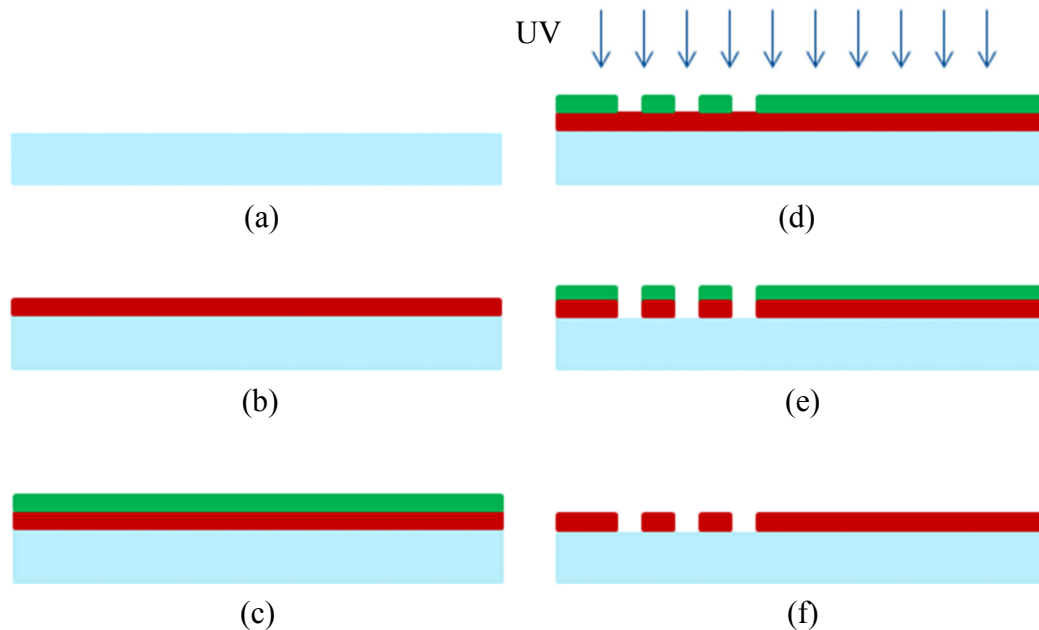


Figure 30. Overview of sensor fabrication. (a) ultrasound cleaning; (b) chromium deposition; (c) photoresist spinning; (d) exposure; (e) wet etching of chrome; (f) photoresist stripping.

The electrical connections to the sensors were obtained with a low-conductivity silver-reinforced conductive epoxy (Duralco 120, Cotoronics Corp., Brooklyn, New York). This connection method was preferred over the wire bonding method because stronger connections are desired during tests and it is not possible to solder chromium. Unlike the wire bonding method, it was observed that the conducting silver epoxy successfully withstood the solvents used in the surface functionalization of the delay path.

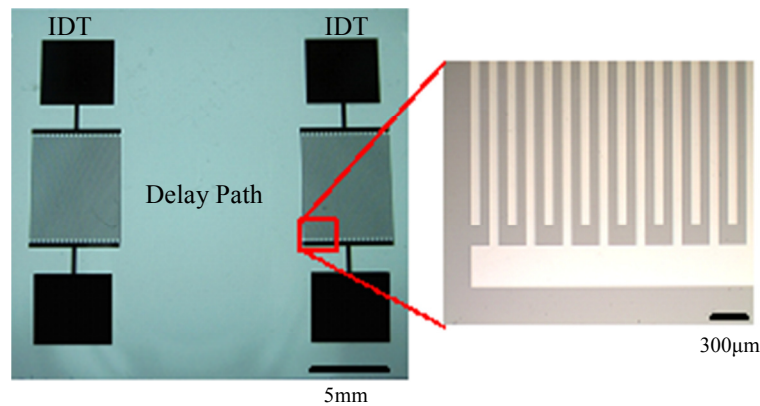


Figure 31. Fabricated ST-cut Quartz sensor

5.2.3. Surface Functionalization

The sensor will quantify Bcl-2 levels in aqueous solutions, so it is necessary to apply surface treatments to the delay path section of the sensor to specifically and selectively sense the target protein. Molecular self-assembly techniques involving bioconjugation were employed to develop an effective Bcl-2 capture method. Bioconjugation can be defined as molecular linking of two or more components to construct a compound—namely, molecular self-assembly of several reagents for a

desired purpose [109, 119]. A scheme was developed to isolate the Bcl-2 protein from a solution via specific binding to a monoclonal capture antibody that is immobilized on the sensor surface. More specifically, self-assembled monolayers (SAMs) and blocking agents were used to optimize Bcl-2 capture on the sensor surface. The surface functionalization developed in this study is novel as it is the first of its kind to isolate and capture Bcl-2 protein using functionalization by surface assemblies. The method was optimized for most effective Bcl-2 capture, with trials of several different SAMs and recipes, which were presented in detail in [109]. The optimization was handled by modified sandwich ELISA tests. The surface functionalization recipe employed in this study is summarized in the following steps (Figure 32):

- First, oxygen plasma cleaning of the surface was performed to remove organic residues and form hydroxyl groups on the surface. The sensors were oxygen plasma-cleaned for 5 minutes. The beaker in which the silanization was performed also was plasma-cleaned for 5 minutes. The hydroxyl groups serve as a foundation for organofunctional silanization.
- Silanization was done using the organosilane, octyldimethyl silane (ODMS, molecular formula $\text{CH}_3(\text{CH}_2)_7\text{Si}(\text{CH}_3)_2\text{Cl}$, Sigma Aldrich, St. Louis, MO) using a solution of 474 μl of stock ODMS in 20ml of acetone resulting in an ODMS concentration of 0.1 M. ODMS provides the linkage between organic and inorganic domains through hydrophobic interactions. The sensors were kept in the solution for 30 minutes, while IDTs were protected by Kapton tape. If the IDTs were not protected, it was observed that the chromium was attacked by HCl formed during the silanization

process, and the sensor did not work properly. After the silanization step, the sensors were rinsed with acetone and ethanol and dried with nitrogen.

- Protein A/G (Pierce Recombinant Protein A/G, Thermo Fisher Scientific, Rockford, IL) with a concentration of $1\mu\text{g/ml}$ in Dulbecco's Buffer Phosphate Silane (DPBS, Life Technologies, Grand Island, NY) was employed for immobilizing antibodies. The sensors were again placed completely in the solution for 1 hour. Protein A/G was adsorbed directly on the ODMS to ensure proper orientation of the antibodies on the sensor surface by binding their constant fragment (F_c) domains. The sensors were rinsed with DPBS after this step.

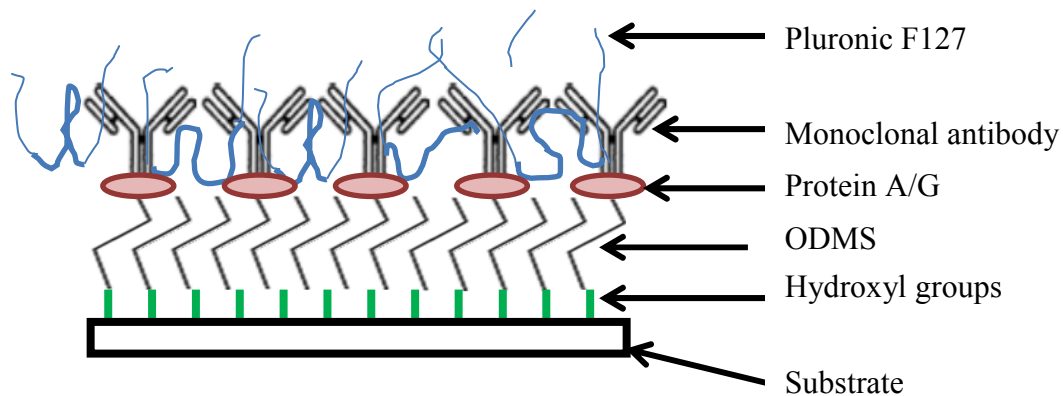


Figure 32. Illustration of surface functionalization.

- Immunoglobulin G (IgG) antibodies (polyclonal rabbit anti-human Bcl-2, Sigma Aldrich, St. Louis, MO) were used for Bcl-2 capture, which are Y-shaped with two antigen binding (F_{ab}) regions and one F_c . The F_c regions were immobilized with the help of Protein A/G onto the surface, resulting in properly-oriented free F_{ab} regions for the most effective Bcl-2 capture and therefore maximum sensor surface affinity. A working concentration of $5\mu\text{g/ml}$ of anti-Bcl-2 in DPBS was placed on the sensor surface as a

droplet covering only the delay path for 1 hour. The sensor surface was then rinsed with DPBS before the final step.

- Pluronic F127 (Sigma Aldrich, St. Louis, MO) was adsorbed to obtain a non-fouling surface for highly selective Bcl-2 capture, which is essential for a diagnostically applicable sensor. The Pluronic, a tri-block copolymer whose non-fouling nature is mediated by its two polyethylene glycol (PEG) chains, prevents other molecules from non-specifically attaching to the sensor surface. The sensor was submerged in 10 μ g/ml Pluronic F127 in DI water for one hour and then rinsed with DI water.

5.3. Measurement Setup and Results

5.3.1. Oscillatory Circuit Design and Experimental Setup

The SH-SAW biosensor was employed in a custom-designed oscillatory circuit for quantifying the Bcl-2 concentrations. An oscillatory circuit configuration was selected due to its higher sensitivity as compared to other detection methods such as vector voltmeter or network analyzer. In the custom oscillator circuit, the sensor was used as the feedback element of the RF amplifier. In this configuration, the relative change in SAW velocity due to Bcl-2 adhesion to the delay path leads to an oscillation frequency shift. This change in oscillation frequency was detected with a digital frequency counter, which was reported to accurately identify of acoustic wave velocities [6]. The setup used for Bcl-2 characterization involves the biosensor, two variable gain RF amplifiers (Olympus 5073PR and Olympus5072PR, Olympus NDT Inc., Waltham, MA), a digital frequency

counter (Agilent 53220A, Agilent Technologies Inc, Santa Clara, CA), an oscillator (Tektronix TDS2001C, Tektronix Inc., Beaverton, OR) and the specifically-designed analog filter, as illustrated Figure 33. Two RF amplifiers were used to enable optimization of the loop gain [120].

The fabrication was done on both ST-cut quartz (90°-off x-axis direction and on 41° Y-cut lithium niobate. The frequency responses for both sensors can be found in Appendix-B. It can be observed from the figures that for ST-cut quartz the response is noisy, with only a few crossings with 0°. The 0° crossings are usually the operation points of the sensors, given the fact that enough amplifier gain is supplied to the system. For the 41° Y-cut lithium niobate sensor, the response is less noisy with several 0° crossings, which results in excitation of several modes, even with using a filter. For this reason ST-cut Quartz is chosen for further sensor development.

As the SH-SAW biosensor was used as a resonator, the frequency response was investigated in order to identify proper circuit satisfying oscillation conditions. Experimentally-measured frequency response is depicted in Figure 34. An insertion loss of 61.5 dB was measured when there was liquid on the functionalized delay line. The frequency response shows several peaks around the designed oscillation frequency (16.8 MHz).

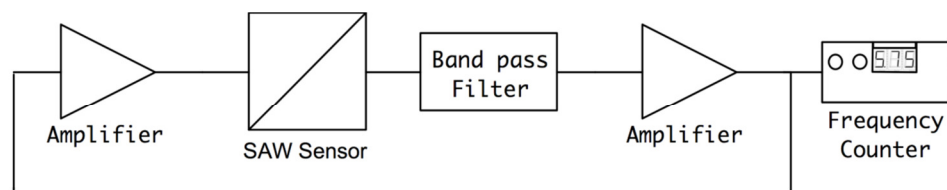


Figure 33. Block schematic for oscillator circuit

The designed feedback/loop based oscillator had a measured short-term frequency stability less than 3 ppm. The experiments show that this sensitivity enabled the detection of Bcl-2 concentration as low as 0.5ng/ml, which was sufficient for this study. The gain of the amplifiers were adjusted, and the passive filter was designed in such a way that the loop gain was 0 dB or higher and the phase shift in the loop was equal to 0° . The oscillation started after these two conditions were met and the exact resonance frequency was the frequency that makes the phase 0° , not the point of peak gain. We chose to use a physical circuit measurement technique rather than simulation techniques for filter design due to the complicated impedance spectrum of SAW devices and the requirement of accurately identifying the total phase in the oscillator loop [121]. The open loop gain and phase were measured by an experimental setup illustrated in Figure 8 (a). A network analyzer (Agilent 5061A, Agilent Technologies Inc., Santa Clara, CA) was used to measure open loop gain and phase satisfying the aforementioned oscillation conditions.

The first oscillation condition required adjustment of the amplifier gain to obtain a total loop gain of at least 0 dB, compensating for all of the losses in the loop. The noise figure of the amplifiers was also important since it affected the frequency stability of the oscillator. The insertion loss of the sensor was -61.5 dB (Figure 34); hence, a feasible range of 61 to 65 dB was determined for the sensor. The passive filter also had an insertion loss of 2 dB; hence, a minimum total gain of 67 dB was supplied by RF amplifiers to meet the first oscillation condition. Additionally, it was observed that the sensor response after surface functionalization was even more noisy (with several local maxima and minima) compared with Figure B1. This was caused by the non-homogenous nature of the protein films, which resulted in additional wave scattering.

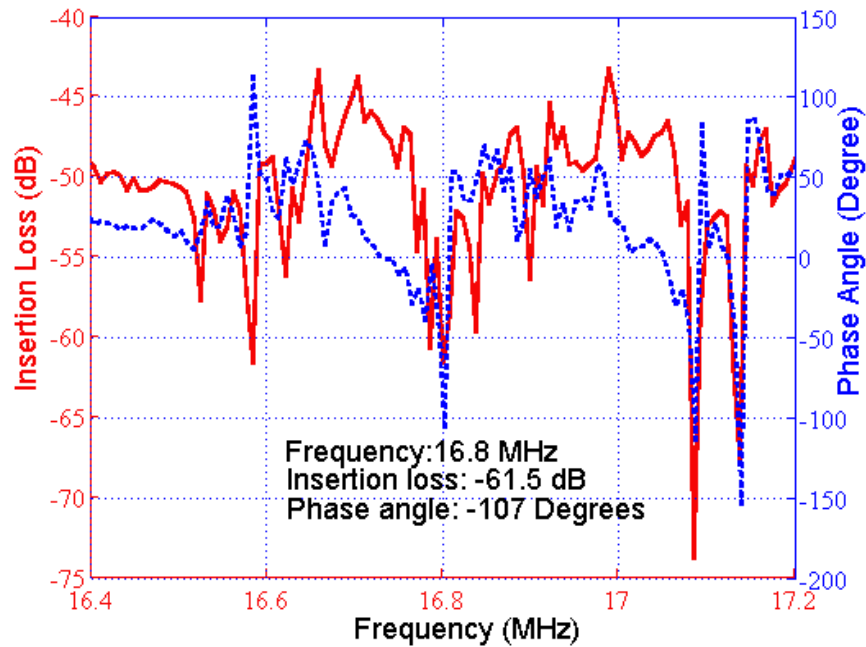


Figure 34. Frequency response of sensor. Insertion loss (red, solid), phase (blue, dashed).

The second oscillation condition was to make the total loop phase 0° and was satisfied using a passive filter. The designed band-pass filter also helped to eliminate the undesirable peaks in the frequency response of the SAW sensor. A pi-type LC band pass filter was designed with 16.8 MHz center frequency and 30% fractional bandwidth. The phase at the center frequency was determined using the set up illustrated in Figure 35 (a). The phase of the filter was designed to obtain 0° total phase in the loop. The designed filter circuit and its frequency characteristics can be seen in Figure 35 (b) and (c). The circuit parameters were determined with the developed MATLAB code then were fine-tuned by the trial and error method [122].

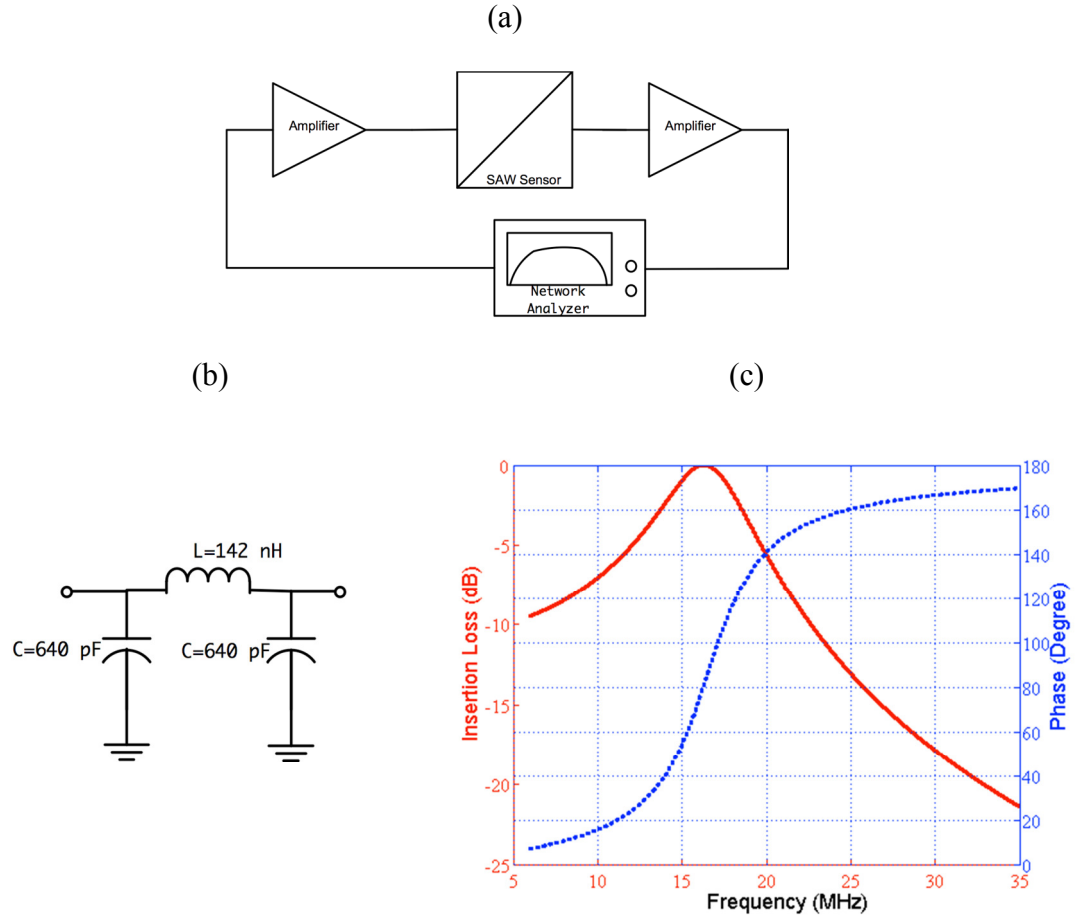


Figure 35. Loop gain and loop phase measurements for filter design. (a) Block diagram of loop-gain and loop phase measurement setup; (b) designed pi type filter; (c) frequency characteristics of filter: insertion loss (red, solid), phase (blue, dashed).

The magnitude and phase response of the loop was also measured after insertion of the filter block. The measured open loop phase lag and the loop gain in the required oscillation frequency were found to be 0° and 3.1 dB, respectively. The block diagram of the measurement setup and the results are illustrated in Figure 36(a) and (b), respectively. As a result, the oscillation conditions were satisfied with this custom designed circuit and oscillation started when the loop was closed in the setup illustrated previously in Figure 33.

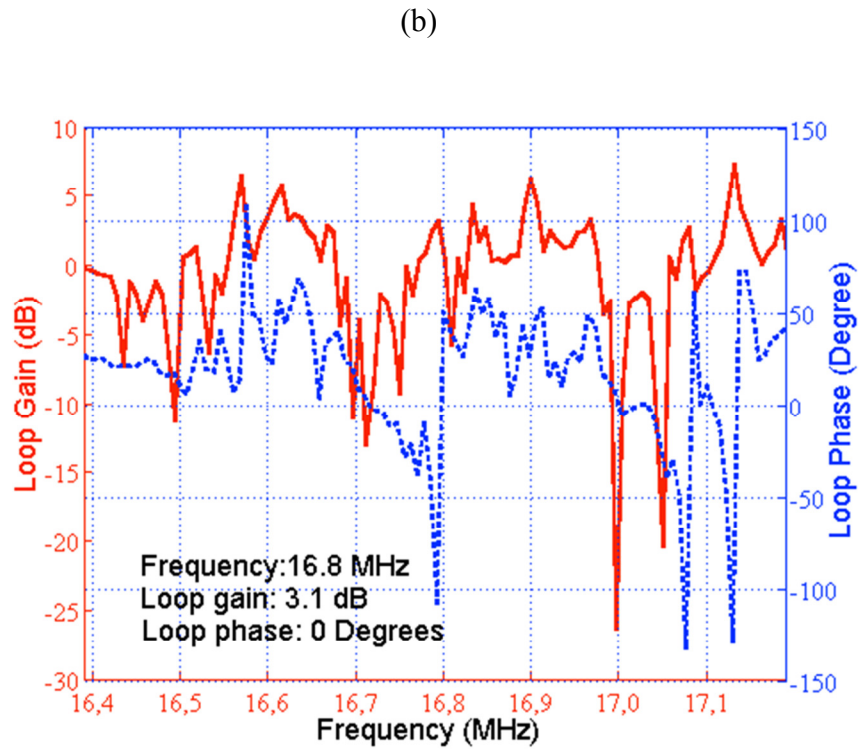
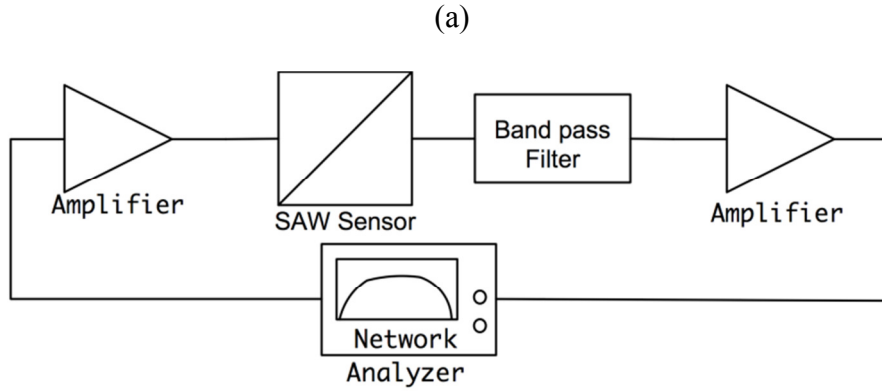


Figure 36. Loop gain and loop phase measurements with filter. (a) block diagram of loop gain and loop phase measurement setup; (b) measured loop gain and loop phase plots: loop gain (red, solid), loop phase (blue, dashed).

5.3.2. Results

The tests were performed using the setup illustrated previously in Figure 5 with Bcl-2 solutions in DPBS ranging from 0.5 to 12ng/ml. Several ST Quartz sensors were

tested with droplets of Bcl-2 solutions for 10 minutes to ensure reproducibility and repeatability. Each fabricated and surface functionalized sensor was used in several tests by soaking them in 1.5M NaCl solution in DI water, rinsing with DI water, and drying them under a nitrogen stream between uses. Each sensor was able to be tested up to 10 times by following this technique to remove Bcl-2 proteins attached to the antibodies. Placed manually on the delay path were 80 μ l droplets of Bcl-2 solutions to ensure that the shape and coverage of the droplets on the delay path were same in each test.

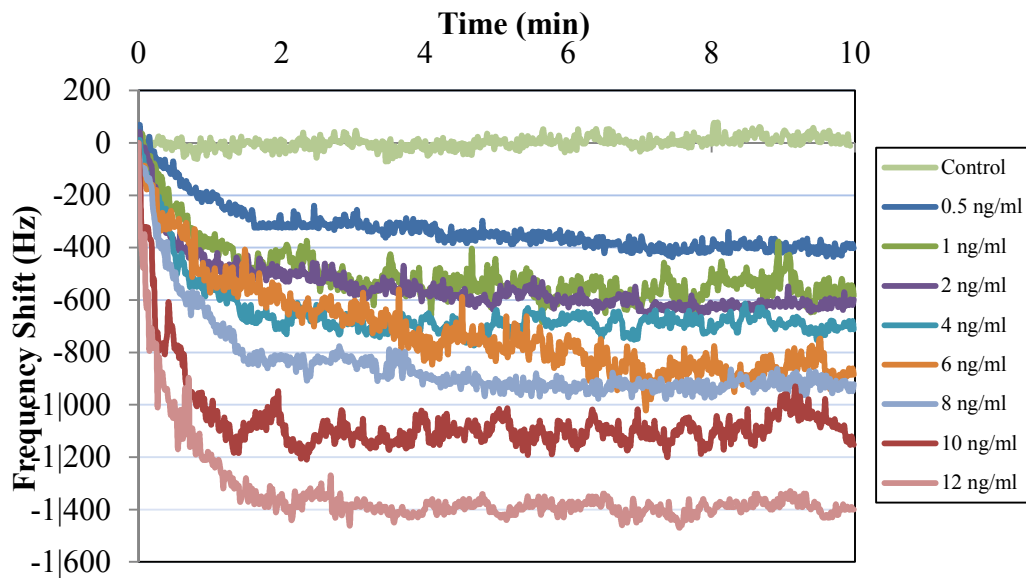


Figure 37. Measured frequency shift (Hz) for various concentrations of Bcl-2 in DPBS.

Bcl-2 solutions with concentrations of 0.5, 1, 2, 4, 6, 8, 10, and 12 ng/ml were tested along with a control (DPBS only). The results of these tests are presented in Figure 37. As can be observed from the figure, there was a clear linear trend of increasing oscillation frequency shift with increasing Bcl-2 concentration. The control test showed almost no shift in oscillation frequency. It can also be observed from the shape of the

curves that the protein adhesion was nearly completed by the end of the second minute. The lowest concentration tested resulted in a frequency shift of >300Hz, which is a detectable value with an oscillation frequency of 16.8MHz. In Figure 38, the shift in oscillation frequency is presented as a function of Bcl-2 concentration. The frequency shift values were calculated by taking the average of data after 2.5 minutes. As seen from the figure, the shift in frequency increases linearly with increasing concentration.

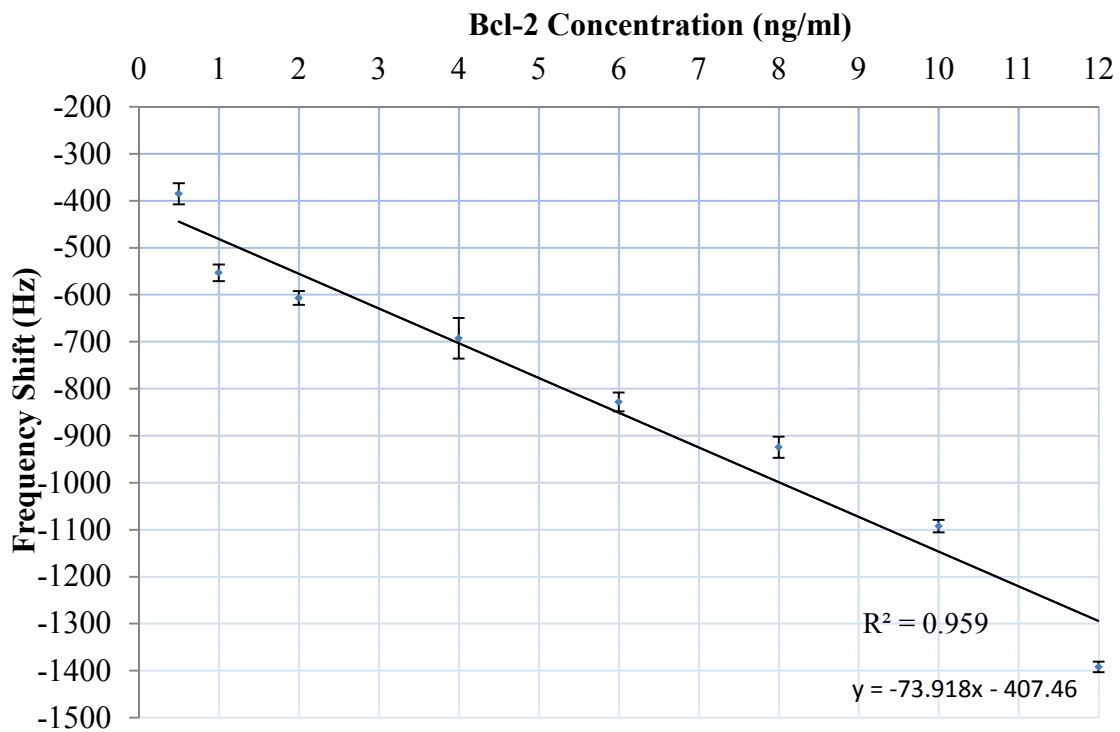


Figure 38. Average frequency shift measured, corresponding to different Bcl-2 concentrations and best line fit ($R^2=0.959$).

Furthermore, another control was also tested with Bovine Serum Albumin (5 mg/ml) in PBS to ensure specificity of the sensing system to Bcl-2. Importantly, when the device designed to detect only Bcl-2 was challenged with a solution of an alternate

protein control (BSA), only a minimal frequency change occurred compared to protein free controls. Finally, the sensor was challenged with a mixture of Bcl-2 (4 ng/ml) and BSA (5 mg/ml), chosen to simulate high urine levels of each protein. Even in the presence of 1000-fold more BSA than Bcl-2, a shift in the frequency similar to Bcl-2 alone was observed, conclusively demonstrating the specificity of this functionalized surface in a biosensor application. The frequency shifts as a function of time obtained from these tests are presented in Figure 39 similarly to Figure 37, with some select data series taken from it for better visualization. The mean and uncertainty of the steady state (>2.5 min) frequency shift of Figure 39 is summarized in Table 6. Steady state frequency shifts of an acoustic biosensor for Bcl-2. Not surprisingly, however, the more highly concentrated protein solutions introduced greater noise, possibly caused by physical interactions between the concentrated but unbound proteins and the multilayered surface which could be reduced by rinsing. Taken together, these results show the best performing surface of those tested has been identified and its specificity and sensitivity demonstrated; however, further optimization and device integration will be necessary before clinical use is feasible.

5.4. Perturbation Considerations

The experimental results of the case study are also analyzed via perturbation method and equations derived in the previous chapter. The equation for liquid loaded perturbation was given in equation (67).

Table 6. Steady state frequency shifts of an acoustic biosensor for Bcl-2.

	Mean (Hz)	Std. Dev. (Hz)
PBS	6	2
Bcl-2 0.5 ng/ml	369	37
Bcl-2 4 ng/ml	693	29
Bcl-2 8 ng/ml	907	40
Bcl-2 12 ng/ml	1392	27
BSA 5ug/ml	108	80
BSA 5ug/ml & Bcl-2 4ng/ml	538	142

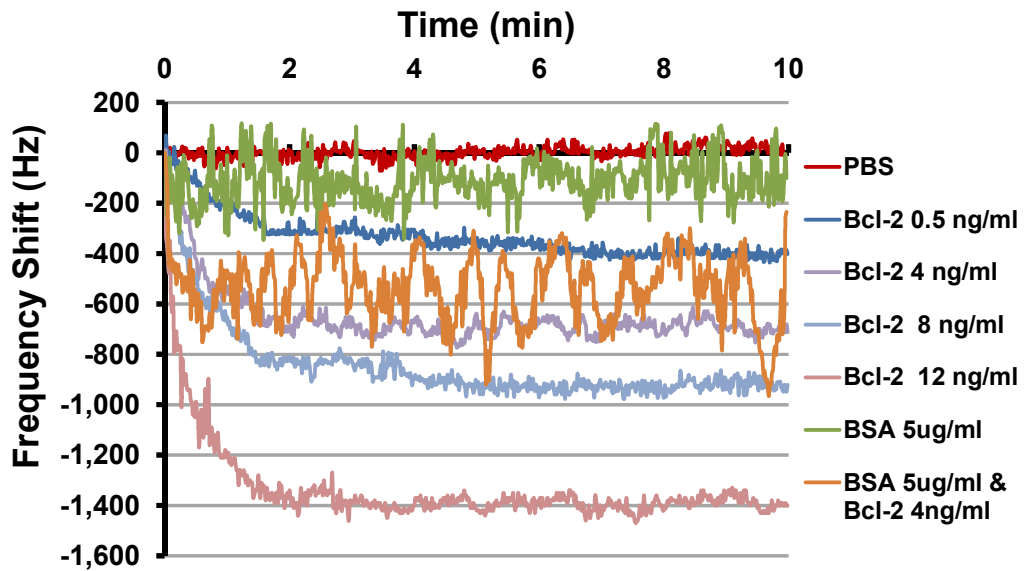


Figure 39. The frequency shifts corresponding to various concentrations of Bcl-2 in PBS, PBS only or BSA controls, and a mixture of Bcl-2 and BSA were measured with an acoustic biosensor.

For the Bcl-2 immunosensor, no other guiding layers were utilized. However, SAMs of protein layers formed on the surface can be regarded as guiding layers with identical properties to protein layer, which is the perturbing mass layer in this case. Assuming identical properties for guiding perturbing layers (perturbing protein layer on top of another protein layer), the terms in perturbation equation reduces to:

$$\left[\frac{1 + \xi_{fm}^2 \tan^2(T_f^0 d_f)}{1 + \xi_{fg}^2 \tan^2(T_f^0 d_f)} \right] = 1, \quad \frac{\left(1 - \frac{v_m^2}{v_0^2}\right)}{\left(1 - \frac{v_g^2}{v_0^2}\right)} = 1 \quad \text{and} \quad \frac{\rho_m}{\rho_g} = 1 \quad (69)$$

Applying these, the perturbation equation reduces to,

$$\frac{\Delta v}{v_0} = \left(\frac{d \ln v}{dz} \right)_{z=z_0}^{fluid} d_m \quad (70)$$

The first term in the right side of the equality, is approximated from the perturbation analysis as the slope of natural logarithm of the dispersion curve. Before approaching the perturbation problem starting from the dispersion curve, the thickness range and region of the dispersion curve should be considered. Typical thicknesses for the protein layers are in the order of 1 to 10 nm [119]. A thickness of 10 nm, corresponds to a z of 0.0056, which is at the very far left of the dispersion curve with virtually no change in phase velocity region. The assumption of perturbation analysis also states that starting point for perturbation is not equal to unperturbed state, which does not hold very true for this case.

The approach is investigated with back-substitution from the experimental results; with the slope of the best fit curve from Figure 38; -74 Hz/(ng/mL of Bcl-2). v_g^∞ can be calculated using the real part of the complex shear modulus (≈ 1 MPa) and density (≈ 1000 kg/m³) supplied in reference [78] for aqueous protein films as 31 m/s.

Another approximation should be made to determine the perturbing mass thickness d_m , since aqueous protein films is not isotropic and uniform. Defining an

effective thickness $d_{m,eff}$ as the ratio of the volume of the film \forall_{film} , by the area on which the sample droplets are placed $A_{surface}$ as:

$$d_{m,eff} = \frac{\forall_{film}}{A_{surface}} \quad (71)$$

The volume of the film also equals the total protein mass captured on the surface Δm_p , divided by the film density:

$$d_{m,eff} = \frac{\Delta m_p}{A_{surface} \rho_m} \quad (72)$$

The total protein mass in a sample equals to protein concentration (C) times the volume of the sample droplet. Substituting this into the equation:

$$d_{m,eff} = \frac{C \forall_{droplet}}{A_{surface} \rho_m} \quad (73)$$

Finally, substituting terms into the perturbation equation, with the slope term renamed as SL and with $f=f_0$:

$$\frac{\Delta f}{f_0} = SL \frac{f_0}{v_g^\infty} \frac{C \forall_{droplet}}{A_{surface} \rho_m} \quad (74)$$

Reorganizing terms, we can obtain the ratio of theoretical frequency change (Δf) and concentration ratio (C) as:

$$\frac{\Delta f}{C} = SL \frac{f_0^2}{v_g^\infty} \frac{\nabla_{droplet}}{A_{surface} \rho_m} \quad (75)$$

The slope SL, which is the experimental counterpart of the first term in the original perturbation equation can be calculated, using the experimentally calculated $\Delta f/C$ of 74 Hz/(ng/mL of Bcl-2). The slope SL is found as $-2.5 \cdot 10^{-4}$; using the values $\nabla_{droplet} = 80 \mu\text{L}$, $A_{surface} = 80 \cdot 10^{-6} \text{ m}^2$ (10mm x 8mm), $v_g^\infty = 31 \text{ m/s}$ and $\rho_m = 1000 \text{ kg/m}^3$ by equation (75). The slope of $-2.5 \cdot 10^{-4}$ is very small, but still large enough to be considered as non-zero.

As seen from the analysis, even though perturbation analysis is efficient in giving insight to the problems, the high order of approximations made during derivation, makes corrections based on experimental work essential. Considering the slope obtained experimentally, the dispersion curve should be experimentally verified first, if further perturbation prediction to be made.

5.5. Discussion and Conclusions

In this study, an ultrasonic MEMS biosensor for detection of urinary anti-apoptotic protein Bcl-2 was successfully designed, fabricated, and experimentally characterized. SH-SAWs were employed with microfabricated IDTs on ST-cut Quartz to

quantify the Bcl-2 concentration. SH-SAWs were generated and sensed by a pair of micro-fabricated IDTs separated by a surface functionalized delay path. An optimized recipe using SAMs of ODMS, Protein A/G, monoclonal antibodies, and Pluronic F127 was employed for the most effective Bcl-2 capture. The method was optimized specificity and selectivity, with trials of several different similar SAMs.

The sensor was experimentally characterized in a resonator circuit by placing buffer solutions of Bcl-2 of known concentration (in DPBS) on the delay path. Bcl-2 concentrations were characterized by the resulting resonance frequency shift caused by the mass loading increase of biomarker binding, which reduces the speed of the SH-SAWs. The target sensitivity for diagnosis and quantifying the stage of ovarian cancer was achieved with successful detection of Bcl-2 in the concentration range of 0.5 to 12ng/ml. It was also observed that there is a linear relationship between the shift in resonance frequency and Bcl-2 concentration. Each sensor was used up to 10 times after applying 1.5M NaCl solutions in DI water to remove the proteins attached to the antibodies. The sensor developed was successful in detecting and quantifying Bcl-2 in the target concentration range. Also control tests with BSA shows the selectivity of the sensor.

The sensor can potentially be employed in a point-of-care test device for monitoring and diagnosis at the patient's bedside. The electrical components of the sensing system—RF amplifiers, frequency counter, and analog filter can potentially be miniaturized, assembled, and packaged in a standalone device with the sensor itself. A new, low-cost, accurate, safe, simple, and reliable testing platform to diagnose ovarian cancer by urinary Bcl-2 levels would benefit all women not only in the U.S., but

worldwide, including medically underserved geographical areas and women at high risk for developing ovarian cancer. This is especially important for detection of early-stage ovarian cancer, which is associated with high survival (>95%) and reduced lifelong medical costs, but currently accounts for less than 10% of diagnosed ovarian cancer cases. In addition to our sensor's ability to accurately detect initial ovarian cancer cases, ovarian cancer monitoring during the course of the disease may indicate recurrent disease and, possibly, therapeutic efficacy. In 2009, 21,550 women were diagnosed with ovarian cancer in the U.S. [93]; this biosensor could potentially detect thousands of previously-undiagnosed cases. In summary, this technology could potentially accurately detect all ovarian cancers, many of which currently go undetected.

CHAPTER 6. CONCLUSION

6.1. Summary and Contributions

In this dissertation, guided surface acoustic wave sensors are theoretically and experimentally investigated in detail. Wave propagation and mass loading sensing with shear horizontal polarized surface acoustic waves are investigated and characterized using analytical modeling and perturbation analysis. The model verification was performed experimentally using surface acoustic wave devices. A surface acoustic wave immunosensor case study was done experimentally and results were investigated using the perturbation analysis. The immunosensor was designed, fabricated and tested for selective capture of protein Bcl-2, which is elevated in many cancer types including ovarian cancer.

Guided surface acoustic waves or Love waves are obtained when a guiding layer is introduced on top of a shear horizontal surface acoustic wave propagating substrates. The layers deposited, spun or grown on top enable wave-guiding, by confining energy to surface, increasing sensor sensitivity and performance. Wave propagation problem was investigated in detail for gravimetric (or mass loading) guided wave sensors. The analytical model was developed for both dry and liquid loaded sensing using wave equation in for multilayer system enabling viscoelasticity. The closed form algebraic solutions were obtained by simultaneous solution of wave equations of each layer, with

continuity of stress and displacement boundary conditions. A numerical approach was developed and used to solve the complex and implicit algebraic equation to obtain dispersion relation. Detailed parametric investigation of dispersion curves was done using typical substrate materials and guiding layers. Substrate types of ST-cut quartz, 41° YX lithium Niobate and 36° YX lithium tantalate with guiding layers of silicon dioxide, metals (chromium and gold), and polymers (Parylene-C and SU-8) were analyzed. The effects of frequency and degree of viscoelasticity were also investigated. The results showed that dispersion curve for different frequencies show similar characteristics but in different guiding layer thickness ranges. The degree of viscoelasticity was demonstrated to have little effect on dispersion. It was also observed that, a transition region with a gradual decrease in phase velocity is obtained, when the shear velocity difference between substrate and guiding layer is relatively high. A smoother transition is observed, when shear velocities are close. Furthermore, the difference in density was also shown to have effect. Large density differences between substrate and guiding layer resulted in sharp with nearly constant slope transition in dispersion curve. Minimal density difference was observed to have a very smooth transition. The model was verified with experiments involving polymers (spun photoresists). It was shown that the model was able to represent the problem with modifications of guiding layer density and shear velocity.

Perturbation methods are employed to obtain approximate solutions to complex problems. Perturbation equations were developed with first order approximations with relating the slope of the dispersion curves presented with sensitivity. The equations were used to investigate the sensitivity for material selection (substrate, guiding layer, and

mass perturbing layer) and degree of viscoelasticity. The investigations showed that the sensitivity is increased with using guiding layers with lower shear velocities and lower densities. Among the guiding layers investigated, Parylene C showed the highest sensitivity with having both lowest density and shear velocity. Gold and chrome was also investigated and similarly gold came out with better sensitivity compared with chrome. The perturbation investigations were also extended for viscoelasticity and for protein layers, which are involved in all of immunosensing applications. It was observed that, more viscoelastic behavior results in more sensitivity. The highest sensitivity values are observed with Parylene-C guiding layer on top of ST-cut quartz substrates. Furthermore, it was observed that the sensitivity to protein layers in this configuration is very similar to sensitivity to viscoelastic Parylene layers. However, it should be noted that the assumption of isotropic behavior for aqueous protein layer may not be very valid.

Finally, an immunosensing case study was presented for selective capture of protein B-cell lymphoma 2 (Bcl-2), which was proven to be related with ovarian cancer. The immunosensor was designed, fabricated, and experimental characterization was done. The sensor was microfabricated in cleanroom environment using traditional MEMS fabrication techniques. A surface-functionalization scheme with monoclonal antibodies, ODMS, Protein A/G and Pluronic F127 was developed and applied to delay path. Detection of Bcl-2 with sub ng/ml sensitivity was successfully presented from buffer solutions. Bcl-2 concentrations were quantified by the resulting resonance frequency shift. The frequency shift was detected by a resonator circuit. The target sensitivity was achieved with demonstrated Bcl-2 detection capability as low as 0.5 ng/ml from a buffer solution. A linear frequency shift increase was observed with increasing Bcl-2

concentration. The selectivity was shown with experiments done with introducing another protein, in addition to Bcl-2, to the buffer. It was seen that similar detection capability of Bcl-2 is obtained even with existence of control protein in very high concentration. The results were investigated with perturbation analysis and equations.

6.2. Future Work

Recommended future work, based on the investigations and results acquired are as follows:

- The analytical model should be modified for more accurate dispersion predictions. Although, modification of guiding layer density seems to be effective, methods or modifications to derivation should be introduced to include this effect.
- The validity of the approximation of perturbation equations with dispersion curve slope should be both theoretically and experimentally verified. The level of agreement for different materials and frequencies should be evaluated.
- Inherent selectivity problem of the surface acoustic wave sensors should be addressed in the long term. The low cost and feasible operation of surface acoustic wave sensor is promising and could possibly contribute significantly to global healthcare.

REFERENCES

1. Lee, S.H., *Theoretical and Experimental Characterization of Time-Dependent Signatures of Acoustic Wave Based Biosensors*, in *School of Electrical and Computer Engineering* 2006, Georgia Institute of Technology: Atlanta, Georgia. p. 156.
2. Ballantine, D.S., *Acoustic wave sensors : theory, design, and physico-chemical applications*. Applications of modern acoustics 1997, San Diego: Academic Press. xii, 436 p.
3. Ikeda, T., *Fundamentals of piezoelectricity*. Corrected pbk. ed. Oxford science publications 1996, Oxford ; New York: Oxford University Press. xi, 263 p.
4. Gardner, J.W., V.K. Varadan, and O.O. Awadelkarim, *Microsensors, MEMS and Smart Devices* 2001, West Sussex, England: Wiley. 528.
5. Onen, O., et al., *A Urinary Bcl-2 Surface Acoustic Wave Biosensor for Early Ovarian Cancer Detection*. *Sensors*, 2012. 12(6): p. 7423-7437.
6. Rocha-Gaso, M.I., et al., *Surface Generated Acoustic Wave Biosensors for the Detection of Pathogens: A Review*. *Sensors*, 2009. 9(7): p. 5740-5769.
7. Du, J., et al., *A study of Love-wave acoustic sensors*. *Sensors and Actuators A: Physical*, 1996. 56(3): p. 211-219.
8. Onen, O., et al., *Surface Modification on Acoustic Wave Biosensors for Enhanced Specificity*. *Sensors*, 2012. 12(9): p. 12317-12328.
9. Auld, B.A., *Acoustic Fields and Waves in Solids* 2nd ed 1990, Malabar, Florida: Krieger Pub. Co.
10. Hashimoto, K.Y., *Surface Acoustic Wave Devices in Telecommunications* 2010, Berlin: Springer-Verlag. 329.
11. White, R.M. and F.W. Voltmer, *Direct Piezoelectric Coupling To Surface Elastic Waves*. *Applied Physics Letters*, 1965. 7(12): p. 314-316.

12. Campbell, C., *Surface acoustic wave devices for mobile and wireless communications*. Applications of modern acoustics 1998, San Diego: Academic Press. xxvi, 631 p.
13. Rayleigh, L., *Theory of Sound*. Vol. II. 1896, Dover, UK.
14. Bruckner, G., et al. *SAW strain sensitivity of selected rayleigh wave crystal cuts*. in *Ultrasonics Symposium (IUS), 2009 IEEE International*. 2009.
15. Bao, X.Q., et al. *SAW Temperature Sensor and Remote Reading System*. in *IEEE 1987 Ultrasonics Symposium*. 1987.
16. Sang-Hun, L., et al. *Vapor phase detection of plastic explosives using a SAW resonator immunosensor array*. in *Sensors, 2005 IEEE*. 2005.
17. Bleustein, J.L., *a new surface wave in piezoelectric materials*. Applied Physics Letters, 1968. 13(12): p. 412-413.
18. Gulyaev, Y.V., *New Type of Surface Sound Wave in Conducting Crystals*. Applied Physics Letters, 1972. 20(6): p. 215-216.
19. Slobodnik, A.J., E.D. Conway, and R.T. Delmonico, *Microwave Acoustics Handbook* 1970: Air Force Cambridge Research Laboratories (U.S.).
20. Milsom, R.F., N.H.C. Reilly, and M. Redwood, *Analysis of Generation and Detection of Surface and Bulk Acoustic Waves by Interdigital Transducers*. Sonics and Ultrasonics, IEEE Transactions on, 1977. 24(3): p. 147-166.
21. Browning, T.I. and M.F. Lewis. *A New Class of Quartz Crystal Oscillator Controlled by Surface-Skimming Bulk Waves*. in *31st Annual Symposium on Frequency Control*. 1977. 1977.
22. Bagwell, T.L. and R.C. Bray. *Novel Surface Transverse Wave Resonators with Low Loss and High Q*. in *IEEE 1987 Ultrasonics Symposium*. 1987.
23. Strashilov, V.L. and V.M. Yantchev, *Surface transverse waves: properties, devices, and analysis*. Ultrasonics, Ferroelectrics and Frequency Control, IEEE Transactions on, 2005. 52(5): p. 812-821.
24. Newton, M., P. Roach, and G. McHale, *ST Quartz Acoustic Wave Sensors with Sectional Guiding Layers*. Sensors, 2008. 8(7): p. 4384-4391.
25. Gizeli, E., et al., *A novel Love-plate acoustic sensor utilizing polymer overlayers*. Ultrasonics, Ferroelectrics and Frequency Control, IEEE Transactions on, 1992. 39(5): p. 657-659.

26. Länge, K., S. Grimm, and M. Rapp, *Chemical modification of parylene C coatings for SAW biosensors*. Sensors and Actuators B: Chemical, 2007. 125(2): p. 441-446.
27. Powell, D.A., et al. *A layered SAW device based on ZnO/LiTaO₃ for liquid media sensing applications*. in *Ultrasonics Symposium, 2002. Proceedings. 2002 IEEE*. 2002.
28. Zadeh, K.K., et al., *A novel Love-mode device based on a ZnO/ST-cut quartz crystal structure for sensing applications*. Sensors and Actuators A: Physical, 2002. 100(2-3): p. 135-143.
29. Herrmann, F., M. Weihnacht, and S. Buttgenbach, *Properties of sensors based on shear-horizontal surface acoustic waves in LiTaO₃/SiO₂ and quartz/SiO₂ structures*. Ultrasonics, Ferroelectrics and Frequency Control, IEEE Transactions on, 2001. 48(1): p. 268-273.
30. Chivukula, V.S., M.S. Shur, and D. Ciplys, *Recent advances in application of acoustic, acousto-optic and photoacoustic methods in biology and medicine*. Physica Status Solidi a-Applications and Materials Science, 2007. 204(10): p. 3209-3236.
31. Zimmermann, C., et al. *Love-waves to improve chemical sensors sensitivity: theoretical and experimental comparison of acoustic modes*. in *Frequency Control Symposium and PDA Exhibition, 2002. IEEE International*. 2002.
32. Glen, M., *Generalized concept of shear horizontal acoustic plate mode and Love wave sensors*. Measurement Science and Technology, 2003. 14(11): p. 1847.
33. Wohltjen, H. and R. Dessy, *Surface acoustic wave probe for chemical analysis. I. Introduction and instrument description*. Analytical Chemistry, 1979. 51(9): p. 1458-1464.
34. Wohltjen, H. and R. Dessy, *Surface acoustic wave probes for chemical analysis. II. Gas chromatography detector*. Analytical Chemistry, 1979. 51(9): p. 1465-1470.
35. Wohltjen, H. and R. Dessy, *Surface acoustic wave probes for chemical analysis. III. Thermomechanical polymer analyzer*. Analytical Chemistry, 1979. 51(9): p. 1470-1475.
36. Lange, K., B.E. Rapp, and M. Rapp, *Surface acoustic wave biosensors: a review*. Analytical and Bioanalytical Chemistry, 2008. 391(5): p. 1509-1519.
37. Roederer, J.E. and G.J. Bastiaans, *Microgravimetric Immunoassay with Piezoelectric-Crystals*. Analytical Chemistry, 1983. 55(14): p. 2333-2336.

38. Calabrese, G.S., H. Wohltjen, and M.K. Roy, *Surface acoustic wave devices as chemical sensors in liquids. Evidence disputing the importance of Rayleigh wave propagation*. Analytical Chemistry, 1987. 59(6): p. 833-837.
39. Flory, C.A. and R.L. Baer. *Surface Transverse Wave Mode Analysis and Coupling to Interdigital Transducers*. in *IEEE 1987 Ultrasonics Symposium*. 1987.
40. Moriizumi, T., Y. Unno, and S. Shiokawa. *New Sensor in Liquid Using Leaky SAW*. in *IEEE 1987 Ultrasonics Symposium*. 1987.
41. Grate, J.W. and G.C. Frye, *Acoustic Wave Sensors*. Sensors Update, 1996. 2(1): p. 37-83.
42. Deisingh, A.K. and M. Thompson, *Biosensors for the detection of bacteria*. Canadian Journal of Microbiology, 2004. 50(2): p. 69-77.
43. Iqbal, S.S., et al., *A review of molecular recognition technologies for detection of biological threat agents*. Biosensors and Bioelectronics, 2000. 15(11-12): p. 549-578.
44. Dubrovsky, T., et al., *Langmuir films of Fc binding receptors engineered from protein A and protein G as a sublayer for immunoglobulin orientation*. Thin Solid Films, 1996. 284-285(0): p. 698-702.
45. Welsch, W., et al., *Development of a Surface Acoustic Wave Immunosensor*. Analytical Chemistry, 1996. 68(13): p. 2000-2004.
46. Freudenberg, J., M. von Schickfus, and S. Hunklinger, *A SAW immunosensor for operation in liquid using a SiO₂ protective layer*. Sensors and Actuators B: Chemical, 2001. 76(1-3): p. 147-151.
47. Freudenberg, J., et al., *A contactless surface acoustic wave biosensor*. Biosensors and Bioelectronics, 1999. 14(4): p. 423-425.
48. Kwon, Y. and Y. Roh, *Development of SH-SAW sensors for underwater measurement*. Ultrasonics, 2004. 42(1-9): p. 409-411.
49. Baer, R.L., et al. *STW chemical sensors*. in *Ultrasonics Symposium, 1992. Proceedings., IEEE 1992*. 1992.
50. Rapp, M., et al. *Mass-sensitive immunosensor based on surface acoustic wave devices for in-situ measurements in water*. in *Proc. 7th Int. Conf. Solid-State Sens. Actuators*. 1993. Yokohama, Japan.

51. Wessa, T., M. Rapp, and H.J. Ache, *New immobilization method for SAW-biosensors: covalent attachment of antibodies via CNBr*. *Biosensors and Bioelectronics*, 1999. 14(1): p. 93-98.
52. Gizeli, E., et al., *A Love plate biosensor utilising a polymer layer*. *Sensors and Actuators B: Chemical*, 1992. 6(1-3): p. 131-137.
53. Rasmusson, A. and E. Gizeli, *Comparison of Poly(methylmethacrylate) and Novolak waveguide coatings for an acoustic biosensor*. *Journal of Applied Physics*, 2001. 90(12): p. 5911-5914.
54. Saha, K., F. Bender, and E. Gizeli, *Comparative Study of IgG Binding to Proteins G and A: Nonequilibrium Kinetic and Binding Constant Determination with the Acoustic Waveguide Device*. *Analytical Chemistry*, 2003. 75(4): p. 835-842.
55. Gizeli, E., et al., *Sensitivity of the acoustic waveguide biosensor to protein binding as a function of the waveguide properties*. *Biosensors and Bioelectronics*, 2003. 18(11): p. 1399-1406.
56. Leidl, A., et al., *Surface acoustic wave devices and applications in liquid sensing*. *Smart Materials and Structures*, 1997. 6(6): p. 680.
57. Moussa, H., C. Andrew, and W. Wojtek, *Acoustic wave sensors: design, sensing mechanisms and applications*. *Smart Materials and Structures*, 1997. 6(6): p. 647.
58. Harding, G.L., et al., *Love wave acoustic immunosensor operating in liquid*. *Sensors and Actuators A: Physical*, 1997. 61(1-3): p. 279-286.
59. Josse, F., F. Bender, and R.W. Cernosek, *Guided Shear Horizontal Surface Acoustic Wave Sensors for Chemical and Biochemical Detection in Liquids*. *Analytical Chemistry*, 2001. 73(24): p. 5937-5944.
60. Schlensoog, M.D., et al., *A Love-wave biosensor using nucleic acids as ligands*. *Sensors and Actuators B: Chemical*, 2004. 101(3): p. 308-315.
61. Gronewold, T.M.A., et al., *Monitoring complex formation in the blood-coagulation cascade using aptamer-coated SAW sensors*. *Biosensors and Bioelectronics*, 2005. 20(10): p. 2044-2052.
62. Perpeet, M., et al., *SAW Sensor System for Marker-Free Molecular Interaction Analysis*. *Analytical Letters*, 2006. 39(8): p. 1747-1757.
63. Wessa, T., et al., *Polyimide, a new shielding layer for sensor applications*. *Sensors and Actuators B: Chemical*, 1998. 53(1-2): p. 63-68.

64. Barié, N., H. Sigrist, and M. Rapp, *Development of immunosensors based on commercially available surface acoustic wave (SAW) devices*. *Analisis*, 1999. 27(7): p. 622-629.
65. Länge, K., et al., *A Surface Acoustic Wave Biosensor Concept with Low Flow Cell Volumes for Label-Free Detection*. *Analytical Chemistry*, 2003. 75(20): p. 5561-5566.
66. Tigli, O., et al., *Fabrication and Characterization of a Surface-Acoustic-Wave Biosensor in CMOS Technology for Cancer Biomarker Detection*. *Biomedical Circuits and Systems, IEEE Transactions on*, 2010. 4(1): p. 62-73.
67. Gruhl, F.J., M. Rapp, and K. Länge, *Label-free detection of breast cancer marker HER-2/neu with an acoustic biosensor*. *Procedia Engineering*, 2010. 5(0): p. 914-917.
68. Gronewold, T.M.A., et al., *Discrimination of Single Mutations in Cancer-Related Gene Fragments with a Surface Acoustic Wave Sensor*. *Analytical Chemistry*, 2006. 78(14): p. 4865-4871.
69. Bröker, P., et al., *A nanostructured SAW chip-based biosensor detecting cancer cells*. *Sensors and Actuators B: Chemical*, 2012. 165(1): p. 1-6.
70. Saitakis, M., A. Tsortos, and E. Gizeli, *Probing the interaction of a membrane receptor with a surface-attached ligand using whole cells on acoustic biosensors*. *Biosensors and Bioelectronics*, 2010. 25(7): p. 1688-1693.
71. Racz, Z., et al. *Cell-based surface acoustic wave resonant microsensors for biomolecular agent detection*. in *Solid-State Sensors, Actuators and Microsystems Conference (TRANSDUCERS), 2011 16th International*. 2011.
72. Tamarin, O., et al., *Real time device for biosensing: design of a bacteriophage model using love acoustic waves*. *Biosensors and Bioelectronics*, 2003. 18(5-6): p. 755-763.
73. Howe, E. and G. Harding, *A comparison of protocols for the optimisation of detection of bacteria using a surface acoustic wave (SAW) biosensor*. *Biosensors and Bioelectronics*, 2000. 15(11-12): p. 641-649.
74. Moll, N., et al., *A Love wave immunosensor for whole E. coli bacteria detection using an innovative two-step immobilisation approach*. *Biosensors and Bioelectronics*, 2007. 22(9-10): p. 2145-2150.
75. Branch, D.W. and S.M. Brozik, *Low-level detection of a Bacillus anthracis simulant using Love-wave biosensors on 36°YX LiTaO3*. *Biosensors and Bioelectronics*, 2004. 19(8): p. 849-859.

76. Berkenpas, E., P. Millard, and M. Pereira da Cunha, *Detection of Escherichia coli O157:H7 with langasite pure shear horizontal surface acoustic wave sensors*. Biosensors and Bioelectronics, 2006. 21(12): p. 2255-2262.
77. Bisoffi, M., et al., *Detection of viral bioagents using a shear horizontal surface acoustic wave biosensor*. Biosensors and Bioelectronics, 2008. 23(9): p. 1397-1403.
78. Weiss, M., et al., *Viscoelastic Behavior of Antibody Films on a Shear Horizontal Acoustic Surface Wave Sensor*. Analytical Chemistry, 1998. 70(14): p. 2881-2887.
79. McHale, G., M.I. Newton, and F. Martin, *Theoretical mass, liquid, and polymer sensitivity of acoustic wave sensors with viscoelastic guiding layers*. Journal of Applied Physics, 2003. 93(1): p. 675-690.
80. McHale, G., *Generalized concept of shear horizontal acoustic plate mode and Love wave sensors*. Measurement Science & Technology, 2003. 14(11): p. 1847-1853.
81. McHale, G., F. Martin, and M.I. Newton, *Mass sensitivity of acoustic wave devices from group and phase velocity measurements*. Journal of Applied Physics, 2002. 92(6): p. 3368-3373.
82. McHale, G., M.I. Newton, and F. Martin, *Theoretical mass sensitivity of Love wave and layer guided acoustic plate mode sensors*. Journal of Applied Physics, 2002. 91(12): p. 9701-9710.
83. Newton, M.I., et al., *Generalized Love waves*. Europhysics Letters, 2002. 58(6): p. 818-822.
84. Balda, M. *LMFnlq - Solution of nonlinear least squares, Matlab subroutine*. 2007, (updated 2012) January 10, 2013]; Available from: <http://www.mathworks.com/matlabcentral/fileexchange/17534-lmfnlq-solution-of-nonlinear-least-squares>.
85. Piezoelectrics, B. <http://bostonpiezooptics.com>. 2013 February 1, 2013].
86. MIT. *LPCVD Silicon Dioxide Process Notes* http://www.mit.edu/~6.777/matprops/lpcvd_sio2.htm. February 1, 2013].
87. Tech, G. *SU-8 Process Files* http://mems.mirc.gatech.edu/msmaweb site/members/processes/processes_files/SU8/SU-8.htm. February 1, 2013].

88. University, C. *Parylene-C Information Sheets* <http://www.nbtc.cornell.edu/facilities/downloads/Parylene%20Information%20Sheets.pdf>. February 1, 2013].
89. Harder, T.A., et al. *Residual stress in thin-film parylene-c*. in *Micro Electro Mechanical Systems, 2002. The Fifteenth IEEE International Conference on*. 2002.
90. Calabri, L., et al., *Nanoindentation shape effect: experiments, simulations and modelling*. *Journal of Physics: Condensed Matter*, 2007. 19(39): p. 395002.
91. Shipley, M., MA, USA. *S1813 Photoresist Datasheet* February 1, 2013]; Available from: <http://www.nanophys.kth.se/nanophys/facilities/nfl/resists/S1813/s1800seriesDataSheet.pdf>.
92. AZ Electronic Materials, B., NJ, USA. *AZP4620 Photoresist Datasheet*. February 1, 2013]; Available from: http://photoresist.com/wp-content/uploads/2010/11/az_p4620_photoresist.pdf.
93. <http://www.cancer.org/docroot/home/index.asp>. American Cancer Society; Accessed November 2009 September 12].
94. Einhorn, N., et al., *Prospective Evaluation of Serum Ca-125 Levels for Early Detection of Ovarian-Cancer*. *Obstetrics and Gynecology*, 1992. 80(1): p. 14-18.
95. van Nagell, J.R., et al., *The efficacy of transvaginal sonographic screening in asymptomatic women at risk for ovarian cancer*. *Gynecologic Oncology*, 2000. 77(3): p. 350-356.
96. Moore, R.G., et al., *The use of multiple novel tumor biomarkers for the detection of ovarian carcinoma in patients with a pelvic mass*. *Gynecologic oncology*, 2008. 108(2): p. 402-408.
97. Jacobs, I. and R.C. Bast, *The Ca-125 Tumor-Associated Antigen - a Review of the Literature*. *Human Reproduction*, 1989. 4(1): p. 1-12.
98. Jacobs, I., et al., *Prevalence Screening for Ovarian-Cancer in Postmenopausal Women by Ca 125 Measurement and Ultrasonography*. *British Medical Journal*, 1993. 306(6884): p. 1030-1034.
99. Ye, B., et al., *Proteomic-based discovery and characterization of glycosylated eosinophil-derived neurotoxin and COOH-terminal osteopontin fragments for ovarian cancer in urine*. *Clin Cancer Res*, 2006. 12(2): p. 432-41.

100. Badgwell, D., et al., *Urinary mesothelin provides greater sensitivity for early stage ovarian cancer than serum mesothelin, urinary hCG free beta subunit and urinary hCG beta core fragment*. *Gynecologic oncology*, 2007. 106(3): p. 490-497.
101. Li, L., et al., *Correlation of serum VEGF levels with clinical stage, therapy efficacy, tumor metastasis and patient survival in ovarian cancer*. *Anticancer Res*, 2004. 24(3b): p. 1973-9.
102. Hellstrom, I., et al., *Detection of the HE4 protein in urine as a biomarker for ovarian neoplasms*. *Cancer Lett*, 2010. 296(1): p. 43-8.
103. Yim, S.C., et al., *Array-based mutation detection of BRCA1 using direct probe/target hybridization*. *Anal Biochem*, 2005. 337(2): p. 332-7.
104. Mavrogiannopoulou, E., et al., *Real-time detection of BRCA1 gene mutations using a monolithic silicon optocoupler array*. *Biosensors & Bioelectronics*, 2009. 24(5): p. 1341-1347.
105. Gagnon, A. and B. Ye, *Discovery and application of protein biomarkers for ovarian cancer*. *Curr Opin Obstet Gynecol*, 2008. 20(1): p. 9-13.
106. Bast, R.C., Jr., B. Hennessey, and G.B. Mills, *The biology of ovarian cancer: new opportunities for translation*. *Nat Rev Cancer*, 2009. 9(6): p. 415-28.
107. Wang, S.Q., et al., *Integration of cell phone imaging with microchip ELISA to detect ovarian cancer HE4 biomarker in urine at the point-of-care*. *Lab on a Chip*, 2011. 11(20): p. 3411-3418.
108. Cory, S. and J.M. Adams, *The BCL2 family: Regulators of the cellular life-or-death switch*. *Nature Reviews Cancer*, 2002. 2(9): p. 647-656.
109. Asad, A.A., *Surface Functionalization and Analysis Thereof for an Ovarian Cancer Diagnostic Biosensor*, in *Department of Mechanical Engineering 2011*, University of South Florida: Tampa, FL. p. 109.
110. Anderson, N.S., et al., *Urinary levels of Bcl-2 are elevated in ovarian cancer patients*. *Gynecologic Oncology*, 2009. 112(1): p. 60-67.
111. Baekelandt, M., et al., *Clinical significance of apoptosis-related factors p53, Mdm2, and Bcl-2 in advanced ovarian cancer*. *Journal of Clinical Oncology*, 1999. 17(7): p. 2061-2068.
112. Guhr, G., et al. *A surface acoustic wave sensor for detection of cell adhesion*. in *Ultrasonics Symposium, 2008. IUS 2008. IEEE*. 2008.

113. Deobagkar, D.D., et al., *Acoustic wave immunosensing of Escherichia coli in water*. Sensors and Actuators B-Chemical, 2005. 104(1): p. 85-89.
114. Yatsuda, H., et al. *Biosensor using shear-horizontal surface acoustic wave*. in *Microwave Conference Proceedings (CJMW), 2011 China-Japan Joint*. 2011.
115. Hechner, J. and W. Soluch, *Pseudo surface acoustic wave dual delay line on 41 degrees YX LiNbO₃ for liquid sensors*. Sensors and Actuators B-Chemical, 2005. 111: p. 436-440.
116. Xiafu, L., et al. *The Small Volume Liquid Density Sensor Using Surface Acoustic Wave*. in *Mechatronics and Automation, Proceedings of the 2006 IEEE International Conference on*. 2006.
117. Yamanouchi, K., K. Abe, and K. Shibayama, *Propagation and Amplification of Rayleigh-Waves and Piezoelectric Leaky Surface-Waves in Structure of InSb Thin-Films on LiNbO₃*. Ieee Transactions on Sonics and Ultrasonics, 1975. 22(5): p. 369-375.
118. Pollard, T.B., et al., *Pure SH-SAW propagation, transduction and measurements on KNbO₃*. Ultrasonics, Ferroelectrics and Frequency Control, IEEE Transactions on, 2006. 53(1): p. 199-208.
119. Hermanson, G.T., *Bioconjugate Techniques*. 2nd ed2008, London: Academic Press.
120. Eichinger, L. *Accurate Design of Low-Noise High Frequency SAW Oscillators*. in *European Microwave week*. 2003. England.
121. Schmitt, R.F., J.W. Allen, and R. Wright, *Rapid design of SAW oscillator electronics for sensor applications*. Sensors and Actuators B-Chemical, 2001. 76(1-3): p. 80-85.
122. Rhea, R.W., *Oscillator Design and Computer Simulation*. 2nd ed2008: Noble Publishing Corporation.

APPENDICES

Appendix A. Matlab Codes

% Property Definitions

clear all

clc

%Solution

f=100E6; %frequency

wt=1E6; %relaxation time

%Substrate

vs=4990; %shear velocity

rhos=2650; %density

t=500E-6; %thickness

nus=vs^2*rhos; %shear modulus

%guiding layer

vlinf=30; %shear velocity

rho1=1000; %density

%top fluid layer

rhof=1000; %density

viscosity=1.2E-3; %dynamic viscosity

nuf=0.16; %shear modulus

Appendix A (Continued)

```
Gf=1i*2*pi*f/(1+1i*2*pi*f*nuf/viscosity); %Complex Shear modulus
```

```
vf=(Gf/rhof)^0.5;
```

```
b=2E-6; %thickness
```

```
%Initial value
```

```
i=1;
```

```
for z=0.002:0.002:0.010
```

```
%Equations
```

```
vl=vlinf*(wt*1i/(1+wt*1i))^0.5;
```

```
Gl=1i*r% Property Definitions
```

```
clear all
```

```
clc
```

```
%Solution
```

```
f=100E6; %frequency
```

```
wt=1E6; %relaxation time
```

```
%Substrate
```

```
vs=4990; %shear velocity
```

```
rhos=2650; %density
```

```
t=500E-6; %thickness
```

```
nus=vs^2*rhos; %shear modulus
```

Appendix A (Continued)

```
%guiding layer

vlinf=30; %shear velocity

rhol=1000; %density

%top fluid layer

rhof=1000; %density

viscosity=1.2E-3; %dynamic viscosity

nuf=0.16; %shear modulus

Gf=1i*2*pi*f/(1+1i*2*pi*f*nuf/viscosity); %Complex Shear modulus

vf=(Gf/rhof)^0.5;

b=2E-6; %thicknesshol*vlinf^2*wt/(1+1i*wt);

d=z*vlinf/f;

x(i)=2*pi*f*(1/vl^2-1/vs^2)^0.5*d;

x_t_re(i)=real(x(i));

x_t_im(i)=imag(x(i));

i=i+1;

end

%function [x,ssq,cnt] = rootfindx(nus,Gl, beta,t,d,w0,Options)

Function for complex root search

%%%%%%%%%%%%%%%%%%%%%%%%%%%%%%%%%%%%%%%%%%%%%%%%%%%%%%%%%%%%%%%%%%%%%%%%

%%%%%%%%%%%%%%%%%%%%%%%%%%%%%%%%%%%%%%%%%%%%%%%%%%%%%%%%%%%%%%%%%%%%%%%%
```

Appendix A (Continued)

```
[x,ssq,cnt] = cxroot(@funw,w0,Options);  
  
%~~~~~  
  
% The nested function funw uses parameters k and c1 from the parent function  
% , where are as input arguments.  
  
% Usef supplied nested function funw defines formulae for calculating value  
% of the complex function of complex argument (w) and other parameters  
% (k,c1)  
  
    function fw = funw(x)  
  
        fw = tan(x)+nus/Gl*(beta/x)*sqrt(x^2/beta^2-1)*tan(beta*t/d*sqrt(x^2/beta^2-1));  
  
    end % fw  
  
end  
  
%SENSITIVITY  
  
%v=complex(v1(:,1),v1(:,2));  
  
LOG=log(v);  
  
%Derivative  
  
kz=1; %z limit  
  
step=0.005; %step  
  
wt=10; %Viscoelasticity  
  
f=100E6; %Frequency  
  
%Guiding layer  
  
rhog=rhol;
```

Appendix A (Continued)

```
vginf=vlinf;
%Mass layer
vminf=vlinf;
for k=1:1:1
vg=vginf*(wt*1i/(1+wt*1i))^0.5;
vm=vminf(k)*(wt*1i/(1+wt*1i))^0.5;
for i=1:1:kz/step
if i==1;
    der(1)=(LOG(2)-LOG(1))/step;
else if i==kz/step;
    der(i)=(LOG(kz/step-1)-LOG(kz/step))/step;
else
der(i)=(LOG(i+1)-LOG(i-1))/0.001;
end
end
S_rho_m_vac(i)=1.3*abs(real( (1-vm^2/v(i)^2)/(1-vg^2/v(i)^2)*der(i)*f/vginf/rhog));
%Vacuum sensitivity
end
S(:,k)=S_rho_m_vac;
end
z=step:step:1;
plot(z,S,'linewidth',3);
```

Appendix B. Frequency Responses of the Bare Sensors

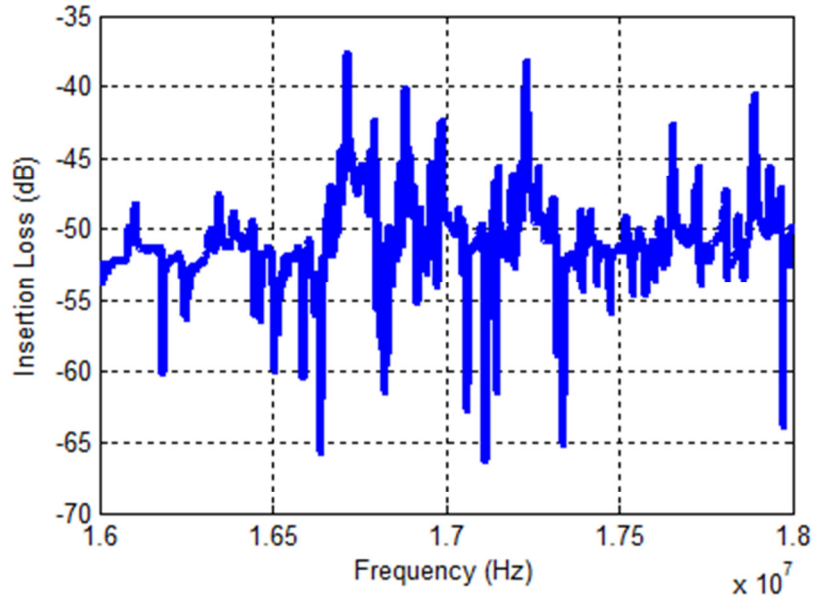


Figure B1. Insertion loss of ST-cut quartz sensor without surface functionalization.

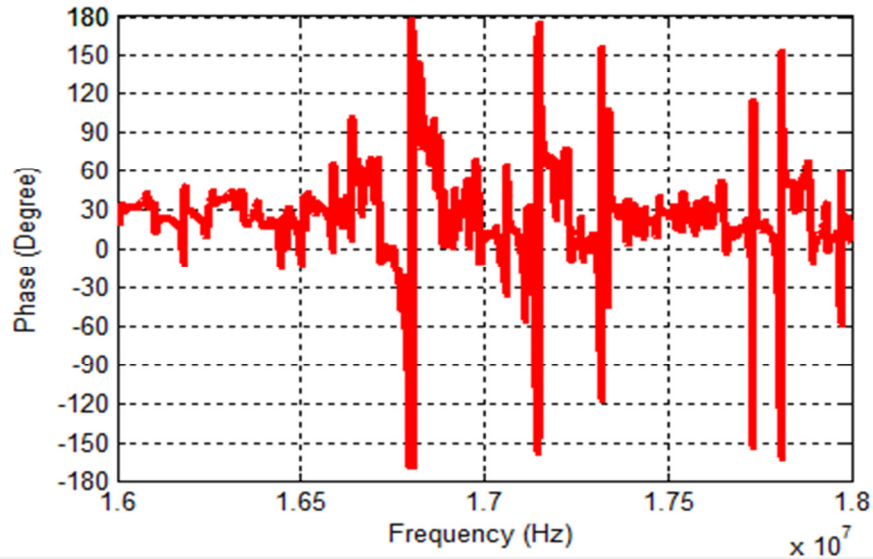


Figure B2. Phase of ST-cut quartz sensor without surface functionalization.

Appendix B (continued)

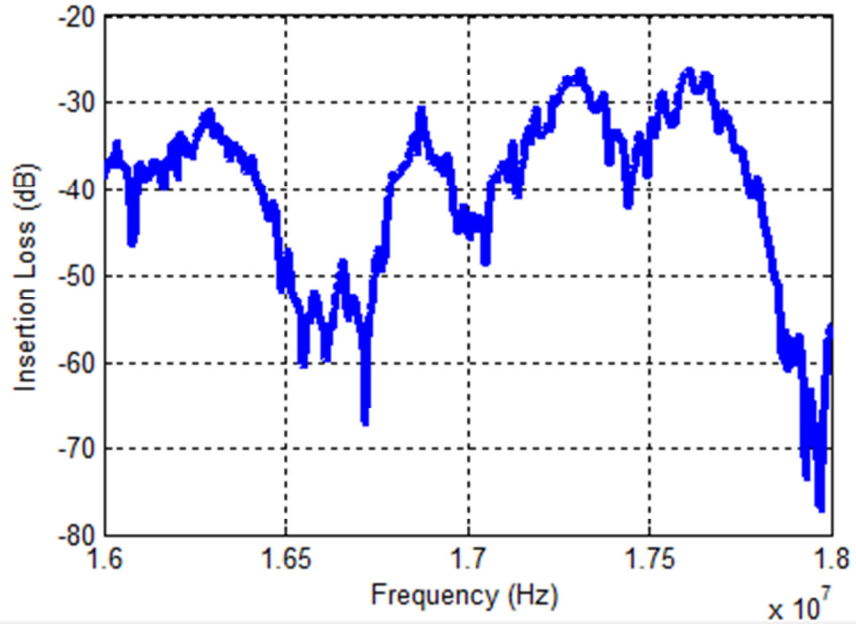


Figure B3. Insertion loss of lithium niobate sensor without surface functionalization.

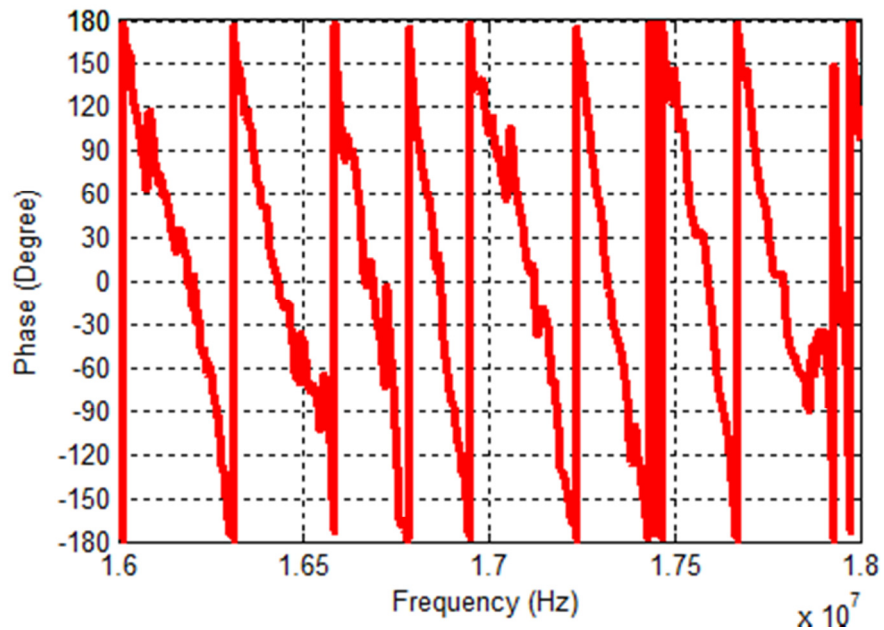
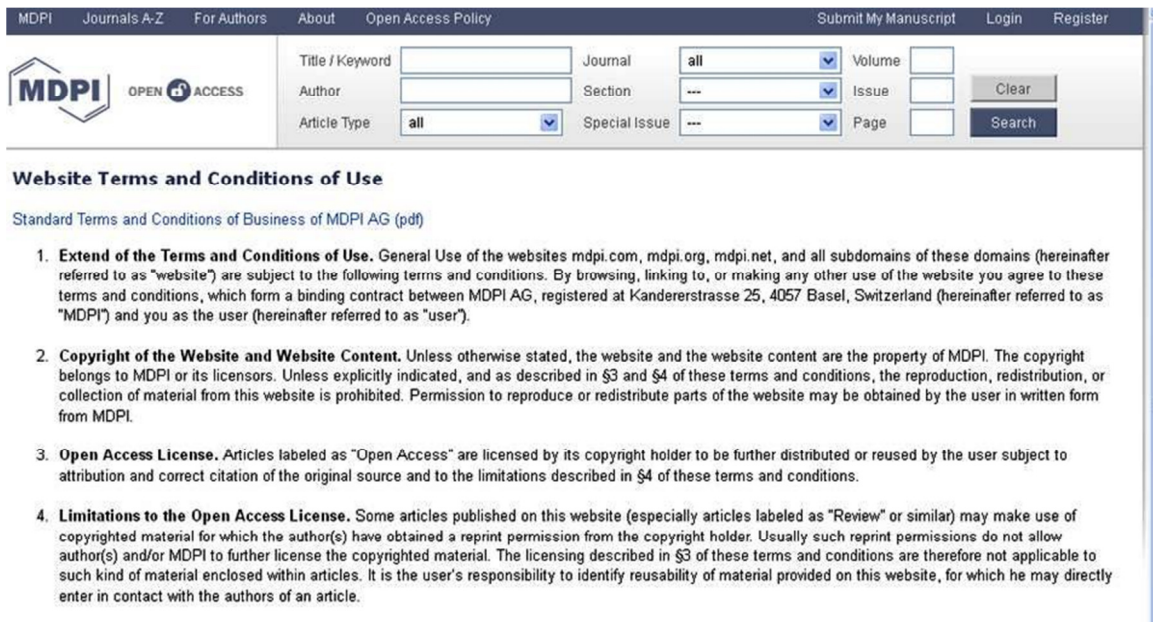


Figure B4. Phase of lithium niobate sensor without surface functionalization.

Appendix C. Copyright Clearance

All referenced figures and manuscript and figures of Chapter 5 were published in open access journal “Sensors MDPI”. The authorization of reproduction of author’s own manuscript is granted by terms of use as stated in “3. Open Access License.” From the webpage: <http://www.mdpi.com/about/termsfuse>. The use of other figures referenced from “Sensors MDPI” (i.e. reference 6) was granted through the publisher and proof e-mail can be found in the last page.



The screenshot shows the MDPI website search interface at the top, with navigation links for MDPI, Journals A-Z, For Authors, About, Open Access Policy, Submit My Manuscript, Login, and Register. The search form includes fields for Title / Keyword, Author, Article Type, Journal, Section, Special Issue, Volume, Issue, and Page, along with a Search button and a Clear button. Below the search form is the "Website Terms and Conditions of Use" section, which includes a link to the "Standard Terms and Conditions of Business of MDPI AG (pdf)" and four numbered points:

- 1. Extend of the Terms and Conditions of Use.** General Use of the websites mdpi.com, mdpi.org, mdpi.net, and all subdomains of these domains (hereinafter referred to as "website") are subject to the following terms and conditions. By browsing, linking to, or making any other use of the website you agree to these terms and conditions, which form a binding contract between MDPI AG, registered at Kandererstrasse 25, 4057 Basel, Switzerland (hereinafter referred to as "MDPI") and you as the user (hereinafter referred to as "user").
- 2. Copyright of the Website and Website Content.** Unless otherwise stated, the website and the website content are the property of MDPI. The copyright belongs to MDPI or its licensors. Unless explicitly indicated, and as described in §3 and §4 of these terms and conditions, the reproduction, redistribution, or collection of material from this website is prohibited. Permission to reproduce or redistribute parts of the website may be obtained by the user in written form from MDPI.
- 3. Open Access License.** Articles labeled as "Open Access" are licensed by its copyright holder to be further distributed or reused by the user subject to attribution and correct citation of the original source and to the limitations described in §4 of these terms and conditions.
- 4. Limitations to the Open Access License.** Some articles published on this website (especially articles labeled as "Review" or similar) may make use of copyrighted material for which the author(s) have obtained a reprint permission from the copyright holder. Usually such reprint permissions do not allow author(s) and/or MDPI to further license the copyrighted material. The licensing described in §3 of these terms and conditions are therefore not applicable to such kind of material enclosed within articles. It is the user's responsibility to identify reusability of material provided on this website, for which he may directly enter in contact with the authors of an article.

Appendix C (continued)

32913

University of South Florida Mail - Re: MDPI Contact Form: Use of published material in dissertation



Onursal Onen <onursalonen@mail.usf.edu>

Re: MDPI Contact Form: Use of published material in dissertation

Support - MDPI <support@mdpi.com>
To: Onursal Onen <onursalonen@mail.usf.edu>

Thu, Mar 28, 2013 at 5:38 AM

Dear Onursal,

Thank you very much for your E-Mail!

The permission is here with guaranteed.
Please find the citation details below the article you'd like to use!

Please do not hesitate to contact me again if there is anything else I can help you with!

Kind regards,
MDPI Support
Marta Körkel

On 26.03.2013 20:39, Onursal Onen wrote:

Dear Sir/Madam,

I have two questions about use of publisher material.

1) I have published two papers as the first author in your open access journal "Sensors" with titles "A Urinary Bcl-2 Surface Acoustic Wave Biosensor for Early Ovarian Cancer Detection" and "Surface Modification on Acoustic Wave Biosensors for Enhanced Specificity". I would like to use the whole manuscript (including tables and figures) of the first manuscript and parts of the second one in my dissertation. Should I obtain a permission to use them? If so, would you please guide me for obtaining it?

2) In my dissertation, I used several figures from the papers published in "MDPI Sensors" journal of other authors. I tried to obtain copyright clearance from copyright.com, but I was notified to contact the publisher. How can I obtain permission to use the other author's figures?

Kind regards,

Onursal Onen